Frequency-Tunable Second-Harmonic Submillimeter-Wave Gyrotron Oscillators

by

Antonio C. Torrezan de Sousa

M.S. (EECS), Universidade Estadual de Campinas (2005)
B.S. (EECS), Universidade Estadual de Campinas (2004)

Submitted to the
Department of Electrical Engineering and Computer Science
in partial fulfillment of the requirements for the degree of

Doctor of Philosophy

at the

MASSACHUSETTS INSTITUTE OF TECHNOLOGY

September 2010

Author .....
Department of Electrical Engineering and Computer Science
August 9, 2010

Certified by .....
Richard J. Temkin
Senior Research Scientist, Department of Physics
Thesis Supervisor

Accepted by .....
Professor Terry P. Orlando
Chairman, Committee on Graduate Students
Department of Electrical Engineering and Computer Science

Frequency-Tunable Second-Harmonic Submillimeter-Wave Gyrotron Oscillators

by

Antonio C. Torrezan de Sousa

Submitted to the Department of Electrical Engineering and Computer Science
on August 9, 2010, in partial fulfillment of the
requirements for the degree of
Doctor of Philosophy

Abstract

This thesis reports the design and experimental demonstration of frequency-tunable submillimeter-wave gyrotrons operating in continuous wave (CW) at the second harmonic of the electron cyclotron frequency. An unprecedented continuous frequency tuning range of more than 1 GHz has been achieved in both a 330- and a 460-GHz gyrotron via magnetic field tuning or voltage tuning.

The 330-GHz gyrotron has generated 19 W of power in a cylindrical $TE_{-4,3,q}$ mode from a 13-kV 190-mA electron beam. The minimum start current was measured to be 21 mA, where good agreement was verified between the measured start current values and the calculation from linear theory for the first six axial modes, $q = 1$ through 6. A continuous tuning range of 1.2 GHz with a minimum output power of 1 W has been achieved experimentally via magnetic or beam voltage tuning. The output stability of the gyrotron running under a computerized control system was assessed to be $\pm 0.4\%$ in power and ± 3 ppm in frequency during a 110-hour uninterrupted CW test. Evaluation of the gyrotron microwave output beam using a pyroelectric camera indicated a Gaussian-like mode content of 91%. Measurements were also carried out in microsecond pulse operation at a higher beam current (610 mA), yielding a minimum output power of 20 W over a tuning range of 1.2 GHz obtained by means of cyclotron frequency tuning and thermal tuning. The 330-GHz gyrotron will be used as a source for 500 MHz nuclear magnetic resonance (NMR) experiments with sensitivity enhanced by dynamic nuclear polarization (DNP).

In addition to the 330-GHz gyrotron, the design and CW operation of a tunable second-harmonic 460-GHz gyrotron are described. The 460-GHz gyrotron operates in the whispering gallery mode $TE_{11,2}$ and has generated 16 W of output power with a 13-kV 100-mA electron beam. The start oscillation current measured over a range of magnetic field values is in good agreement with theoretical start currents obtained from linear theory for successive high order axial modes $TE_{11,2,q}$. The minimum start current is 27 mA. Power and frequency tuning measurements as a function of the electron cyclotron frequency have also been carried out. A smooth frequency tuning range of 1 GHz with a minimum output power of 2 W has been obtained for the

operating second-harmonic mode either by magnetic field tuning or beam voltage tuning. Long-term CW operation was evaluated during an uninterrupted period of 48 hours, where the gyrotron output power and frequency were kept stable to within $\pm 0.7\%$ and ± 6 ppm, respectively, by a computerized control system. Proper operation of an internal quasi-optical mode converter implemented to transform the operating whispering gallery mode to a Gaussian-like beam was also verified. Based on images of the gyrotron output beam taken with a pyroelectric camera, the Gaussian-like mode content of the output beam was computed to be 92% with an ellipticity of 12%. The 460-GHz gyrotron is intended to be used as a submillimeter-wave source in a 700-MHz DNP/NMR spectrometer.

Thesis Supervisor: Richard J. Temkin
Title: Senior Research Scientist, Department of Physics

Acknowledgments

I would like to thank my research supervisor Dr. Richard Temkin for opening the doors of this renowned institution and for giving me this unique opportunity to work in a world-class project. His trust, patience, support, expertise, and guidance throughout the process were essential for the development and refinement of this work. I would like to acknowledge the members of my thesis committee, Dr. Richard Temkin, Prof. Qing Hu, and Prof. Ronald Parker, for reading my thesis. Prof. Ronald Parker also served as my academic advisor and as a committee member in my research qualifying exam along with Prof. David Staelin. I would also like to thank Prof. Robert Griffin, director of the Francis Bitter Magnet Laboratory at MIT, for his support and I am grateful to the National Institutes of Health and the Department of Electrical Engineering and Computer Science at MIT for providing financial assistance.

Many people came along during these years at MIT, each one helping in a different way. I am grateful to many current and former members, both official and unofficial, of the Waves and Beams Division at the Plasma Science and Fusion Center over my time here: Dr. Chiping Chen, Dr. Jake Haimson, Paul Thomas, Dr. Amit Kesar, Dr. Yoshiteru Hidaka, Dr. Alan Cook, Chad Marchewka, Dr. Jing Zhou, Dr. Ronak Bhatt, Dr. Ksenia Samokhvalova, Dr. Eunmi Choi, Dr. Colin Joye, Dr. Roark Marsh, Brian Munroe, Emilio Nanni, and Elizabeth Kowalski. Dr. Jagadishwar Sirigiri provided valuable assistance and motivation in many steps of this project, from simulations to the experiments. Ivan Mastovsky was very helpful in bringing things from the paper world to the real world and in debugging problems when the situation did not look promising. Dr. Michael Shapiro always kept his door open to discuss things as extraordinary as electromagnetic mode converters and as mundane as soccer. The collaboration with Dr. Seong-Tae Han at the beginning of this work was very helpful and appreciated. I am also thankful to Dr. Paul Woskov, and William Mulligan for their technical assistance.

Outside of the group, I would like to acknowledge the people at the Francis Bitter Magnet Laboratory: Alexander Barnes for discussions about dynamic nuclear po-

larization as well as Ajay Thakkar, Jeffrey Briant, and Ronald DeRocher for their technical assistance. I am also thankful to Dr. Jeffrey Neilson, then at Calabazas Creek Research, for providing and supporting his code Surf3D. Outside of the laboratory, the greater world of Boston and the United States has been explored with the good company of Dr. Rajiv Menjoge, Dr. Hae Jin Kim, David Tax, Nick Comfoltey, and Antoine Cerfon, among others.

I could not have begun this journey at MIT without the prior support received in my country. I acknowledge my former advisors Prof. Hugo Figueroa at the Universidade Estadual de Campinas, and Dr. Gilberto Medeiros Ribeiro, then at the Laboratório Nacional de Luz Síncrotron in Campinas-SP, Brazil, for their guidance and encouragement. Also, nothing that has been said would have been possible without the support of my family, in particular that of my parents, Fernando and Iracema. All of the sacrifices they made over these years deserve more than thanks, and they will never be forgotten.

À minha família e Àquele que me ajudou a superar as tormentas desta jornada

Contents

List of Figures

List of Tables

Abbreviations and Acronyms

AC	Alternating current
BWO	Backward-wave oscillator
CFA	Crossed-field amplifier
CPI	Communication and Power Industries
CVD	Chemical vapor deposition
CW	Continuous wave
DAQ	Data acquisition
DC	Direct current
DESY	Deutsches Elektronen Synchrotron
DNP	Dynamic nuclear polarization
ECH-CD	Electron cyclotron heating and current drive
ECM	Electron cyclotron maser
EDM	Electrical discharge machining
EIK	Extended-interaction klystron
EPR	Electron paramagnetic resonance
FEL	Free-electron laser
FFT	Fast Fourier transform
FWMH	Full width at half maximum
gpm	U.S. liquid gallons per minute
IAP	Institute of Applied Physics (Nizhny Novgorod, Russia)
IF	Intermediate frequency
LINAC	Linear accelerator
LO	Local oscillator

LOG	Large-orbit gyrotron
MAGY	Maryland Gyrotron self-consistent code
MBK	Multiple-beam klystron
MIG	Magnetron injection gun
MIT	Massachusetts Institute of Technology (Cambridge, MA, USA)
NLC	Next Linear Collider
NMR	Nuclear magnetic resonance
NRL	U.S. Naval Research Laboratory
PBG	Photonic band gap
PFN	Pulse forming network
PID	Proportional, integral, and derivative
PRF	Pulse repetition frequency
QCL	Quantum cascade laser
RF	Radio frequency
SBK	Sheet-beam klystron
SI	International System of Units
SNR	Signal-to-noise ratio
TE	Transverse electric
TM	Transverse magnetic
TWT	Traveling-wave tube
VED	Vacuum electron device
VNA	Vector network analyzer
XFEL	X-ray free-electron laser

Chapter 1

Introduction

Vacuum electronics was not included on the list of endangered species in 1947 when John Bardeen (1908-1991) and Walter Brattain (1902-1987) invented the bipolar transistor under the direction of William Shockley (1910-1989) at Bell Laboratories. While our society has enormously benefited from the development of solid-state electronics and integrated circuits, vacuum electronics followed its own course of evolution and reinvention by responding to the demand of applications whose requirements of more efficient high-power high-frequency devices were beyond the capability of its solid-state counterpart. The superior performance of vacuum electron devices (VEDs) at high frequencies can be attested in Fig. 1-1, which portrays the state-of-the-art of microwave and submillimeter-wave sources. The microwave spectrum corresponds to frequencies between 0.3 and 300 GHz while the submillimeter or terahertz band ranges from 300 GHz up to 3 THz. Nowadays VEDs are present in our homes in the form of a magnetron inside our microwave ovens and in other applications such as plasma heating, materials processing, communication and radar systems, particle acceleration, diagnostics, and spectroscopy.

The primary focus of this thesis is the development of a continuous-wave (CW) frequency-tunable 330 GHz gyrotron oscillator operating at the second harmonic of the electron cyclotron frequency. This VED will be utilized for a spectroscopic application, namely nuclear magnetic resonance (NMR) enhanced by dynamic nuclear polarization (DNP). Before entering the details about the device and its application,

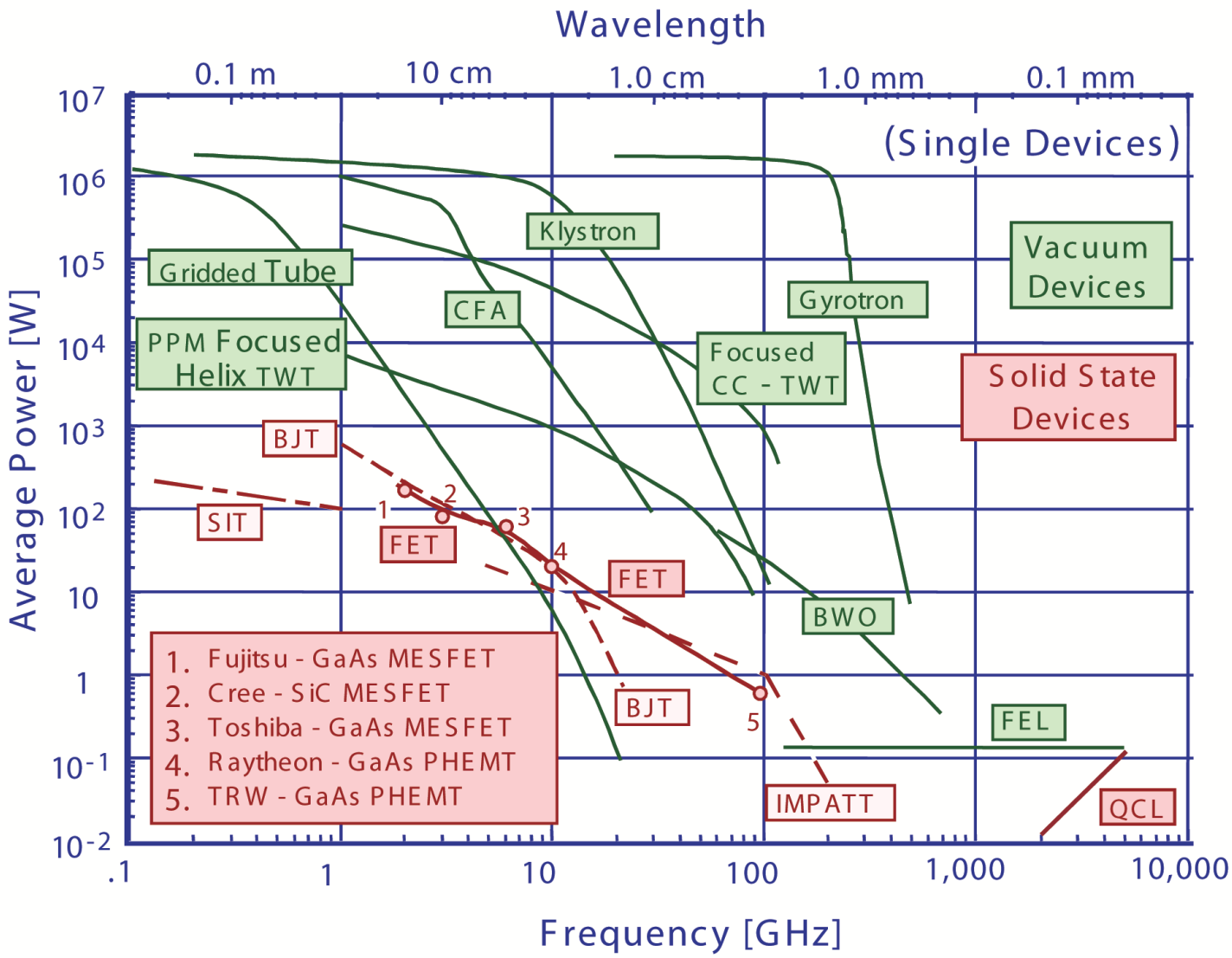

Figure 1-1: Average power capability of single solid-state and vacuum electron devices in the microwave and submillimeter bands (Modified from original figure courteously provided by Bruce Danly, NRL).

an overview of the physics and evolution of VEDs will be given.

1.1 Physics of Vacuum Electron Devices

Vacuum electron devices generate or amplify electromagnetic waves by converting the energy of electrons to electromagnetic wave energy. In the majority of VEDs, the most common configuration to generate an electron beam is by thermionic emission from a cathode followed by acceleration due to an applied direct-current (DC) or pulsed voltage. As electrons travel through the device, magnetic fields are utilized to guide and confine the beam, counterbalancing the repulsive electrostatic forces. At the beginning of the interaction region, electrons emit spontaneous electromagnetic radiation with random phases at first. There are basically three processes in which charged particles can produce electromagnetic radiation: Cherenkov radiation, transition radiation, and *bremsstrahlung*.

- Cherenkov radiation occurs when electrons travel in a medium or structure with a velocity greater than the phase velocity of the electromagnetic wave in that medium or structure. Examples of VEDs based on Cherenkov radiation include backward-wave oscillators (BWO), traveling-wave tubes (TWTs), orotrons, magnetrons, and crossed-field amplifiers (CFAs).

- Transition radiation is generated when electrons travel through a spatially inhomogeneous medium such as media with different refractive indexes or perturbations including conducting grids, plates, or gaps between conducting surfaces. Gaps and cavities are utilized in klystrons to produce transition radiation.

- *Bremsstrahlung* occurs when electrons oscillate in external electric fields such as in reflex triodes or in external magnetic fields such as in gyrotrons and free-electron lasers (FELs).

In the case of an oscillator, the initial spontaneous radiation from electrons may excite an electromagnetic eigenmode associated with an interaction structure such as

a waveguide or a resonator. In the case of amplifiers, these eigenmodes are already excited by the input high-frequency signal. As electrons interact and remain in close synchronism with the electromagnetic field in the interaction structure, some electrons are accelerated while others are decelerated. This process may stimulate the formation of electron bunches if the electron transit time through the interaction structure is longer than the wave period. Once electrons are grouped together, an alternating-current (AC) component is imparted to the DC beam, enabling electrons to radiate in phase and produce coherent radiation. A net energy transfer to the wave will occur as long as the electron bunches stay in the decelerated phase of the field during the most part of the interaction process. In oscillators, if the power transferred from the beam exceeds circuit losses, the mode initially excited from spontaneous radiation can grow due to internal or external feedback until it reaches steady state. In amplifiers, the beam-wave interaction usually occurs in a single pass due to the absence of feedback, which is desirable in order to avoid unwanted oscillations in the amplifier circuit. After the interaction, the spent electron beam is collected and its excess energy is dissipated.

Synchronism and bunching are two essential conditions for generation of coherent stimulated radiation in VEDs. Different classes of VEDs are characterized by their particular synchronism and bunching mechanisms. The synchronism condition that allows electrons to interact with an electromagnetic wave for a time longer than the wave period T_0 can be expressed as:

$$\omega - k_z v_z = n\Omega \tag{1.1}$$

where ω is the wave angular frequency, k_z is the axial wavenumber, v_z is the electron axial velocity, n is the harmonic number, and Ω is the angular frequency of electron oscillations due to external electric or magnetic fields.

In the absence of electron oscillations, the synchronism condition becomes $v_{ph} = \omega/k_z \approx v_z$ and it requires waves with phase velocity v_{ph} less than the speed of light in vacuum c to interact with electrons. This condition is fulfilled by sources of Cherenkov

radiation that utilizes slow-wave periodic structures, for example, helices and coupled cavities. These structures are found in devices such as TWTs and BWOs, which constitute a class of VEDs known as slow-wave devices. Following the dispersion relation of the interaction structure:

$$k^2 = k_\perp^2 + k_z^2 \tag{1.2}$$

where $k = \omega/c$ is the free-space wavenumber and $k_\perp$ is the transverse wavenumber, one has $k_\perp^2 < 0$ since $v_{ph} < c$. This implies that the fields are evanescent in the transverse direction and localized near the wall of the slow-wave structure. As a consequence, the electron beam should be located close to the structure wall for an effective coupling to the wave. Slow-wave structures have features with dimensions that are a fraction of the wavelength. This leads to the rapid miniaturization of these structures with increasing frequency, making their fabrication more difficult and their ability to handle power limited as indicated in Fig. 1-1.

If electron oscillations are present, the synchronism condition allows electrons to interact with electromagnetic waves with superluminal phase velocity, the so called fast waves. Members of this class of VEDs known as fast-wave devices include FELs, where electron oscillations are caused by a periodic static magnetic field, and gyrotrons, where a strong homogeneous static magnetic field B_0 makes electrons oscillate at the electron cyclotron frequency ω_c:

$$\Omega = \omega_c = \frac{eB_0}{m_e\gamma} \tag{1.3}$$

where e is the absolute value of the elementary electric charge, m_e is the electron rest mass, and γ is the relativistic factor, which is related to the beam voltage V_b by $\gamma = 1 + eV_b/m_ec^2 = 1 + V_b/511\text{k}$. Fast waves can be simply supported by smooth wall waveguides. At a given frequency, waveguides with large transverse dimensions, larger than the wavelength, can be employed since operation with high-order waveguide

modes is permitted by the synchronism condition.

These overmoded smooth wall waveguides are easier to be fabricated and have a competitive advantage in terms of breakdown and power handling due to their larger surface area and transverse dimensions. This enables fast-wave devices such as gyrotrons to deliver unprecedented power levels not only at microwave frequencies but also in part of the submillimeter band, helping to fill with more power the so called "THz gap" between conventional microwave sources and far-infrared lasers (see Fig. 1-1). Furthermore, the electron beam can be placed away from the waveguide walls since the fields are not evanescent inside the waveguide as it follows from the fast-wave condition $v_{ph} > c$.

Although operation with high-order modes enables larger structures that can withstand more power, issues with mode competition may arise due to the increased mode density. Mode competition can be addressed by choosing a high-order operating mode well isolated from its neighbors and/or by using structures with sparser mode density such as photonic-band-gap (PBG) [3] or confocal structure [4].

Classification of VEDs according to the electron bunching mechanism is often divided as M-type or O-type devices. In M-type devices such as magnetrons and CFAs, bunching occurs by modulating the spatial positions of electrons that move, for example, in crossed external electric and magnetic fields. In O-type devices such as klystrons, TWTs, and gyro-devices, bunching occurs by modulating electron momenta through interaction with a high-frequency electromagnetic field. In klystrons and TWTs, electron bunching is primarily caused by the electric-field component parallel to the electron velocity and to the external static magnetic field axis, leading to axial bunching and extraction of the axial beam energy to the electromagnetic wave. In fast-wave gyro-devices, the dominant electron bunching mechanism is the azimuthal bunching [5] which originates from the interaction between the perpendicular component of the electric field and the perpendicular component of the electron velocities with respect to the external static magnetic field axis. This process results in extraction of the perpendicular kinetic energy of the electron beam to the high-frequency field while the axial beam energy is left undisturbed.

1.2 Evolution of Vacuum Electron Devices

In 1873, James C. Maxwell (1831-1879) summarized what was known on electromagnetics and optics in a set of equations that led to the prediction of electromagnetic waves. The existence of these waves remained theoretical until 1888 when Heinrich R. Hertz (1857-1894) first produced and detected electromagnetic waves using a spark-gap generator and a loop antenna with a spark-gap detector. After the first wireless transmission in history performed by Hertz, the emergence and demand of wireless communications at longer distances drove the development of more powerful versions of the spark-gap transmitter as it was pursued for example by Guglielmo Marconi (1874-1937). Interference problems caused by the broad spectrum of spark signals encouraged the technical community in the early 20^{th} century to seek alternative ways of generating continuous sine waves at radio frequencies (RF). Among the options considered, one may cite a high-frequency mechanical alternator (known as Alexanderson alternator named after Ernst F. W. Alexanderson (1878-1975)) able to operate at frequencies up to 200 kHz and deliver up to 200 kW [6], or the use of the negative resistance of an electric arc to maintain the oscillation of a resonant LC circuit (known as the Poulsen-arc transmitter named after Valdemar Poulsen (1869-1942)). Operational frequencies up to 1 MHz and generated power up to 1 MW had been reported for the arc transmitter [7].

1.2.1 Triodes

Sources based on spark-gap, alternator, or arc-transmitter technologies would be soon replaced by the advent of vacuum electron devices. In 1883, Thomas A. Edison (1847-1931) observed that an electric current could be drawn between the heated filament (cathode) and the collector plate (anode) of an evacuated bulb if a positive voltage were applied to the plate with respect to the filament. These charges traveling through the vacuum were later identified as electrons following the work of J. J. Thomson (1856-1940) of 1897. In 1904, J. A. Fleming (1849-1945) showed that the unidirectional current in Edison's diode could be used as a rectifier or detector of radio

signals. In 1906, Lee de Forest (1873-1961) demonstrated that the flow of electrons in the diode could be controlled by inserting a grid between the cathode and the anode. As a consequence, a small time-varying signal applied between the grid and the cathode could result in an amplified signal in the cathode-anode circuit. The greater sensitivity provided by the triode amplifier not only extended the range of radio communications but also enabled a reduction of the transmitter power. Soon after its use as an amplifier was realized, the triode tube started to be employed in oscillating circuits for radio transmitters in as early as 1915 [8].

In 1920, H. Barkhausen (1881-1956) and K. Kurtz discovered that the triode tube could oscillate at higher frequencies by creating a potential well where electrons could oscillate back and forth. This well can be formed by biasing the grid at a positive voltage higher than the potential of the cathode and the anode while maintaining the anode potential slightly lower than the cathode potential to reflect electrons back through the grid. These sources are also known as reflex triodes and the angular frequency Ω of electron oscillation in the nonrelativistic case is approximately given by:

$$\Omega \sim \sqrt{\frac{eE_0}{m_e l}} \tag{1.4}$$

where E_0 is the amplitude of the electrostatic field, and l is a scale of the field inhomogeneity, which is on the order of the distance between the electrodes forming the potential well [9].

As communication systems moved toward higher operating frequencies motivated by the larger bandwidth available for faster data rates and more communication channels, smaller circuits and antenna dimensions, and larger antenna gain for a given antenna size, it was noticed by the 1930s that the performance of gridded-tube amplifiers degraded drastically at wavelengths comparable in size with the triode constituent elements. This degradation can be credited to wire inductance, interelectrode capacitance, and the variation of the phase of the radio signal during the electron transit from the cathode to the anode [10]. Although minimizing the size of gridded tubes

could alleviate these issues, the power-handling capability of these smaller tubes is reduced as shown in Fig. 1-1.

1.2.2 Klystrons

The frequency limitations of gridded tubes required a reinvention of vacuum tubes. Alternative devices emerged using waveguides and cavities instead of wires and electrode plates, and taking advantage of a new concept of electron velocity modulation that leads to *spatial bunching*. This concept of velocity modulation was developed in 1935 by A. Arsenjewa-Heil (1901-1991) and O. Heil (1908-1994). An example of such a device is the klystron invented by the brothers R. H. Varian (1898-1959) and S. F. Varian (1901-1961) in 1939 [11].

During World War II, the limited power provided by klystrons restricted their use as receiver tubes [10]. After the war, klystrons with more than two cavities were developed for higher gain and better efficiency driven by applications such as in particle accelerators and television transmitters. One example of such development began in 1948 with the fabrication of three-cavity S-band (2-4 GHz) klystrons for the Stanford Mark III electron linear accelerator (LINAC). These klystrons ultimately reached 30 MW of output power in 1-μs pulses.

The simplest configuration of a klystron amplifier is shown in Fig. 1-2 and consists of an electron gun, an input and output cavities, a drift tube between cavities, an external magnetic field to guide and confine the electron beam, and a collector. Klystrons are classified as linear-beam devices since the electron beam generated by an electron gun propagates linearly through the axis of the tube in parallel with the confining magnetic field. As the beam passes the input cavity, the electrons will interact with the electric field excited by the input RF signal during a transit time shorter than the RF period T_0. Depending on the phase of the electric field during the interaction in the first cavity, some electrons will be accelerated and others decelerated. Once in the field-free drift section, fast electrons will overtake slow electrons, leading to the formation of bunches that arrive at the second cavity at the period T_0 of the RF input signal as shown in the space-time diagram also known as Applegate diagram

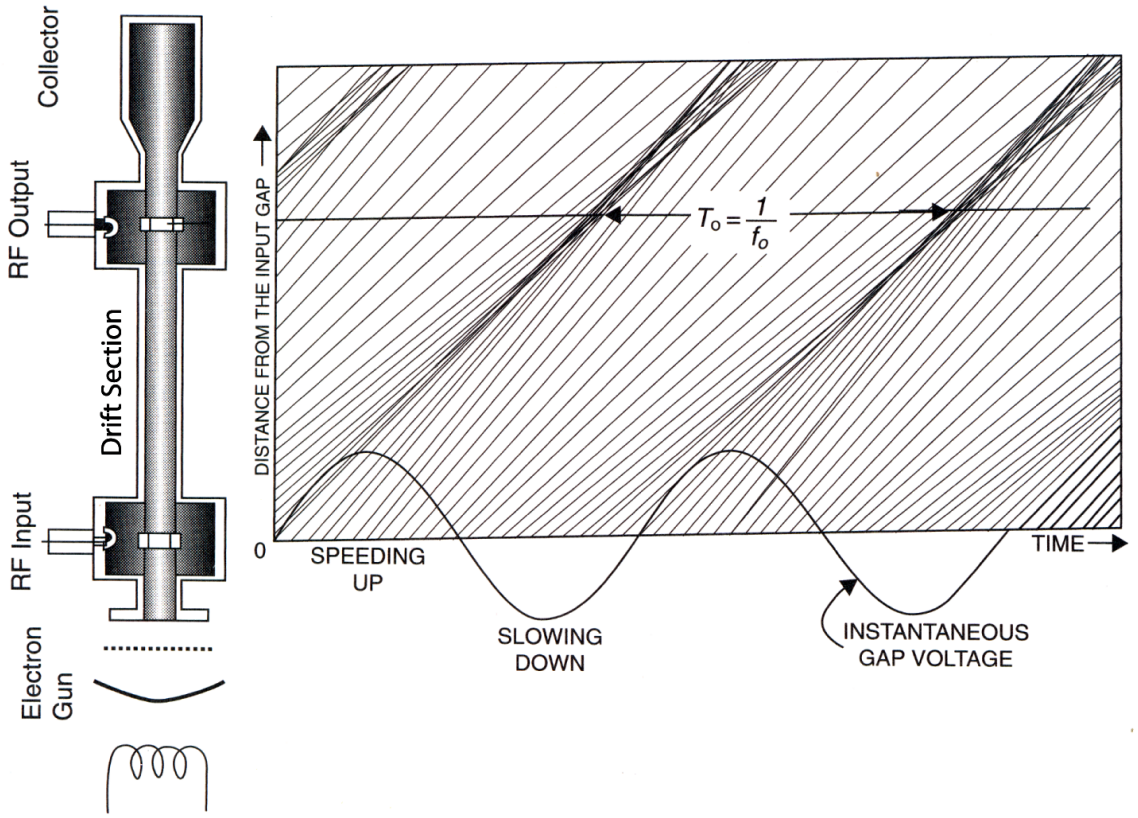

Figure 1-2: Two-cavity klystron configuration and space-time diagram (Applegate diagram) showing electron velocity modulation and electron bunching (Adapted from [1]).

in Fig. 1-2. As these bunches pass through a narrow gap in the output cavity, they will excite microwaves through coherent *transition radiation* and have their kinetic energy transferred to the wave, resulting in an output signal more powerful than the input one under proper conditions. In the sequence, the spent beam is collected. One major limitation of the klystron interaction circuit is its narrow bandwidth.

This ballistic description of the formation of electron bunches considers space-charge effects negligible. As the beam current density increases for higher beam power operation or lower voltage operation at a fixed beam power for simpler and cheaper power supplies, space-charge forces become more significant and prevent tighter bunches from being formed, resulting in lower efficiencies. In order to mitigate these space-charge effects, alternate configurations of klystrons were devised using multiple beams or a single beam extended in one transverse dimension. In

multiple-beam klystrons (MBK), the total current is distributed among several drift tubes so that the current density in each tube is low enough to allow efficient electron bunching that will interact with the field of a common microwave structure. When compared to single-beam klystrons, MBKs are more expensive and difficult to fabricate but they offer the possibility of reduced beam voltage operation with higher efficiency and broader instantaneous bandwidth [12]. Currently, some particle accelerator projects such as the X-ray free-electron laser (XFEL) and the TESLA linear collider at the Deutsches Elektronen Synchrotron (DESY) have chosen MBKs delivering 10 MW of peak output power at 1.3 GHz with efficiency of 65% as their RF source [13]. Another approach under development is the sheet-beam klystron (SBK) [14] where the beam is extended in one dimension to reduce space-charge effects and allow higher beam currents.

Limitations imposed by microwave breakdown and reduced beam-wave interaction in klystrons using a single-gap output cavity can be minimized by employing extended interaction structures to decelerate the electron beam. Examples of such extended output structures include multi-gap resonators, coupled cavities, or traveling-wave sections. A recent effort for the now ceased work on the Next Linear Collider (NLC) has developed X-band (8-12 GHz) pencil-beam klystrons able to generate 75 MW of peak output power with 50% efficiency [15]. These klystrons utilize periodic permanent magnets for electron beam focusing and a traveling-wave structure as an output circuit [16].

As klystrons have features that are a fraction of the wavelength such as the beam-wave interaction length, the average power capability of these devices dramatically reduces at millimeter-wave frequencies as indicated in Fig. 1-1. State-of-the-art CW extended-interaction klystrons (EIKs) are stretching the capabilities of the klystron technology toward the end of the microwave band, delivering 50 W of output power at 140 GHz and 6 W at 220 GHz [17].

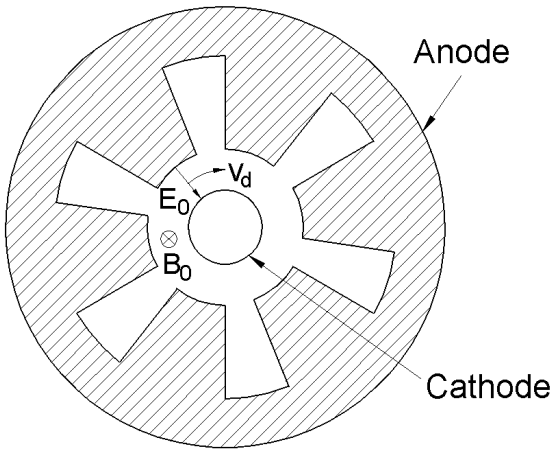

Figure 1-3: Schematic of a radial magnetron with a cathode at the center.

1.2.3 Crossed-Field Devices

In 1916, A. W. Hull (1880-1966) began experiments on the use of magnetic fields to control electrons in vacuum devices as an alternative to electrostatic control. This research led to the invention of the magnetron in 1921. This crossed-field oscillator that predates the klystron consisted of a coaxial diode geometry with an external axial magnetic field applied. In 1939-40, J. T. Randall (1905-1984) and H. A. H. Boot (1917-1983) greatly improved the magnetron by utilizing cavity resonators in the anode block and peak output power as high as 10 kW could be obtained at 3 GHz [18]. During World War II, cavity magnetrons were used by the Allied forces in their air defense radar systems and had a great impact on the war. Although the advent of other VEDs and solid-state devices after the war replaced magnetrons in many applications, magnetrons remained important and are used in compact airborne and marine radars and for heating applications in industry and in our homes as part of the microwave oven [10].

The configuration of a conventional cavity magnetron with a cathode at the center is shown in Fig 1-3. In this configuration, the applied electric field E_0 between cathode and anode and the external axial magnetic field B_0 are oriented at the right angle with respect to each other, making electrons drift perpendicularly to the crossed external fields at a velocity $\mathbf{v_d} = \mathbf{E_0} \times \mathbf{B_0}/B_0^2$. For a given beam voltage, the B_0 value should be higher than the Hull cutoff magnetic field in order to prevent electrons from reaching

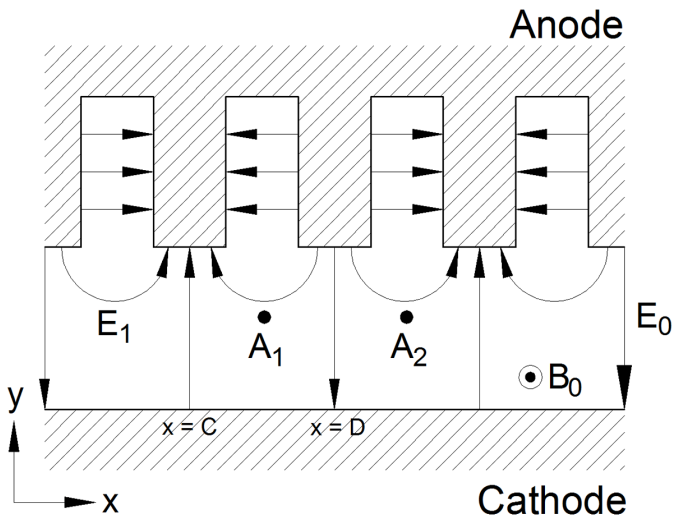

Figure 1-4: Planar magnetron configuration in π-mode operation depicting the static electric and magnetic fields E_0 and B_0, the microwave electric field E_1, and two test electrons A_1 and A_2.

the anode. The resonance condition for magnetrons to generate microwaves requires the electron drift velocity v_d to be in near synchronism with the phase velocity v_{ph} of an electromagnetic wave propagating in the slow-wave structure formed by the periodic anode circuit. The magnetic field B_0 that fulfills the synchronism condition is given by the Buneman-Hartree condition. Magnetrons oscillate at a magnetic field above the Hull cutoff and below or near the Buneman-Hartree threshold.

Unlike other VEDs, the beam formation and microwave generation in magnetrons are not separated in space, making its analysis more involved. A glimpse of the beam-wave interaction in the magnetron can be described with the assistance of Fig. 1-4, which shows the configuration of a planar magnetron with the microwave electric field E_1 in π-mode operation. Consider two test electrons, A_1 and A_2. Electron A_1 is in the decelerating phase of the field and is being moved toward a region of higher microwave electric field near the anode due to $\mathbf{E_1} \times \mathbf{B_0}$. As electron A_1 is closer to the anode, it will interact more strongly and have a reduced potential energy, transferring kinetic and potential energy to the electromagnetic wave. On the other hand, electron A_2 is in the accelerated phase of E_1, absorbing energy from the wave, and the $\mathbf{E_1} \times \mathbf{B_0}$ drift moves this electron downward toward the cathode, increasing the electron potential energy and weakening the beam-wave interaction. As these effects are stronger for

A_1 than A_2, the amplitude of the wave will grow.

The y-component of the microwave electric field E_{1y} is responsible for displacing electrons toward the region favorable for the beam-wave interaction where A_1 is located. For example, if electron A_1 has a drift velocity greater than v_{ph}, this electron will advance toward $x = C$ but as E_{1y} opposes E_0, the drift velocity $(E_0 + E_{1y})/B_0$ will be reduced and restored to synchronism. Conversely, if A_1 drifts slower than the wave and reaches $x = D$, the drift velocity will be increased since E_0 and E_{1y} reinforce each other, moving A_1 back to synchronism. On the other hand, if electron A_2 drifts faster than the wave, its drift velocity will increase even further when it reaches $x = D$, moving A_2 to the region favorable for interaction. The situation is analogous when the drift velocity of electron A_2 is slower than v_{ph}. This mechanism leads to the formation of electron spokes and it is known as phase focusing.

In the 1950s, while magnetrons had found a good match in high-power applications such as radars, other applications, including communications, drove the development of crossed-field amplifiers (CFAs). The configuration of a CFA is similar to that of a magnetron but it includes an input and output port for the signal to be amplified. The input microwave signal is coupled through one cavity and then circulates around the CFA circuit to be extracted at a higher amplitude from another cavity. The input and output ports in CFAs are isolated, ensuring that the amplification process occurs in a single pass.

Commercially available magnetrons for industrial heating are able to deliver 75 kW CW with an impressive 80% efficiency at 915 MHz [19]. Other commercial versions can produce 2.5 kW CW at 2.45 GHz with efficiency of 62% [19] or deliver peak output power of 3 MW between 2.7 and 2.9 GHz with efficiency of 4.6% for a duty cycle of 0.08% with pulse width of 2 μs [20]. Experimental versions of crossed-field oscillators have demonstrated higher output peak power such as the magnetron developed at the Institute of Applied Physics (IAP) in Nizhny Novgorod, Russia, which was able to produce a peak power as high as 4 GW at 9.2 GHz with pulse duration of 15 ns at 11% efficiency [21].

Commercial versions of CFAs can deliver output power of 900 kW between 9.0 and

9.5 GHz for a pulse width of 0.83 μs and duty cycle of 0.1% [22]. A lower frequency CFA operating in a frequency range of 1.28-1.35 GHz can achieve a gain of 11.2 dB and produce a peak power of 5.3 MW for a pulse width of 2 μs and duty cycle of 0.1% [23].

1.2.4 Slow-Wave Devices

Other VEDs were added to the tube family during World War II and a few years after its end. During his experiments with klystron amplifiers for radar receivers in the early 1940s, R. Kompfner (1909-1977) noticed one limitation of the klystrons he was dealing with at that time: the weak coupling between electrons and the electromagnetic fields in a klystron resonator gap. In order to obtain sufficient gain from his klystrons, Kompfner had to slow down the electron velocity so that the beam could interact for a longer time with the fields in the klystron resonator. This fact led him to suggest a structure where the electromagnetic fields would travel with electrons. As electromagnetic waves in free space move faster than electrons, Kompfner proposed a helical structure to slow down the waves and enable the beam-wave interaction. The outcome of this work was the invention of the traveling-wave tube (TWT) in 1943 [24].

A few years later in 1952, Kompfner realized he could turn his TWT in a voltage-tunable oscillator and that gave origin to the backward-wave oscillator (BWO). While Kompfner's oscillator utilized a linear beam, another contemporary version of the BWO developed by B. Epsztein utilized a crossed field and his device was called a carcinotron. Orotrons were invented and investigated in the 1960s [25].

As outlined in Section 1.1, TWTs and BWOs rely on periodic slow-wave structures that provide waves with subluminal phase velocity v_{ph} that are close to the electron axial velocity v_z in order to enable beam-wave interaction over distances longer than the wavelength. Examples of slow-wave structures include the aforementioned helix, coupled cavities for operation at higher powers, and rippled-wall cylindrical structures shown in Fig. 1-5a . If electrons and the axial component of the electric field E_{1z} are in perfect synchronism, half of the electrons will be accelerated while the other half

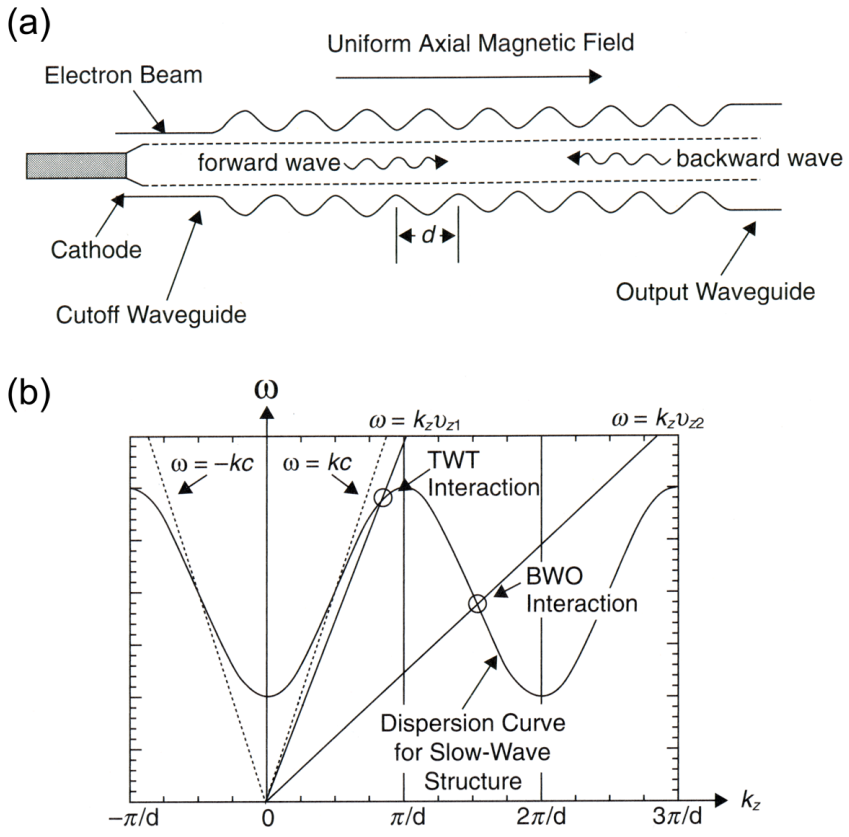

Figure 1-5: (a) Schematic of a rippled-wall slow-wave structure and (b) associated dispersion diagram for a TWT or a BWO (Adapted from [2]).

will be decelerated. The result of this interaction is the formation of electron bunches toward the field null without a net energy transfer. In case $v_z \gtrsim v_{ph}$, the bunches will gradually form in the decelerated phase of the field, resulting in a net energy transfer from the beam to the wave.

The electromagnetic fields in a slow-wave structure can be represented as a superposition of traveling waves with each wave having the same frequency ω and an axial wavenumber $k_{zs} = k_{z0} + s2\pi/d$. Here d denotes the structure period, s is the spatial harmonic number, and k_{z0} is the axial wavenumber for the zeroth-order harmonic ($-\pi/d < k_{z0} < \pi/d$). Slow waves will be formed because most of the components will have a large k_z yielding $v_{ph} = \omega/k_z > \omega/c$.

The dispersion diagram of a rippled-wall cylindrical structure is shown in Fig. 1-5b and its passband has a dependence on the depth of the wall ripples. For this particular

dispersion diagram, the region of TWT operation is in the zero spatial harmonic between $k_z = \omega/c$ and $k_z = \pi/d$. For the BWO operation, the region of interest is the first spatial harmonic between $k_z = \pi/d$ and $k_z = 2\pi/d$. In this first harmonic region, the electrons and the energy of the wave propagate in opposite direction due to the negative group velocity $v_g = d\omega/dk_z$, creating an internal feedback mechanism for oscillations.

Orotrons operate near $k_z = 2\pi/d$, resulting in radiation at fundamental wavelengths $\lambda \approx d/\beta$ much smaller than the period of the slow-wave structure for non-relativistic devices, where $\beta = v/c = (1 - \gamma^{-2})^{1/2}$ is the normalized electron velocity to the speed of light. This oscillator can be implemented in a two-mirror resonator formed by a concave mirror and a plane mirror with a periodic structure profiled on its surface. Stimulated diffraction radiation (Smith-Purcell radiation) is excited in the orotron by a linear beam propagating close to the periodic structure on the plane mirror [25].

In TWT amplifiers the excitation of parasitic backward waves can be prevented by dividing the amplifier circuit into sections intercalated by lossy parts named severs. In this configuration, initial modulation of the electron beam is provided by the small input signal in the amplifier input section. Although the electromagnetic fields are damped by the severs, the prebunched electron beam can propagate through the circuit and excite amplified microwaves at the ouput section of the TWT under proper conditions.

TWTs often operate at a fundamental transverse magnetic (TM) mode but other designs being proposed advocate the use of overmoded structures with selective suppression of competing modes for higher output power at high operating frequencies such as in the W-band (75-110 GHz) [26, 27].

The main feature of the TWT amplifier is its wide instantaneous bandwidth since there is no resonant structure. This feature makes the TWT attractive for applications in communications, radars, and in electronic countermeasure systems. The TWT technology achieved such a level of maturity that space-based TWTs for satellite communications can have an overall efficiency as high as 70% and provide an output

average power of hundreds of Watts at a gain of 50 dB or more at the Ku-band (12-18 GHz) in a package weighing about 1 kg [12, 28]. Efforts to build TWT amplifiers operating at frequencies as high as 220 GHz using microfabrication techniques are under way [29, 30].

For oscillators, the main attribute of BWOs is the broad electronic frequency tunability via beam voltage, where tuning ranges over 15% can be achieved [31]. BWOs can radiate at frequencies up to 1.4 THz with a milliwatt power level. At lower frequencies, these oscillators can deliver 1 W at 300 GHz and 10 W at 140 GHz [32]. Devices based on diffraction radiation such as orotrons can provide CW radiation up to 0.1-0.5 W at 300-375 GHz [25].

Oscillators can also be implemented by adding an external feedback to a slow-wave amplifier circuit. Using this approach, a compact 650-GHz source using a microfabricated folded waveguide slow-wave structure was able to generate 50 mW peak with an efficiency of 0.19% [33].

1.2.5 Gyro-Devices

While classical VEDs were maturing in the late 1950s, theoretical investigations of microwave generation by interaction between fast waves ($v_{ph} > c$) and electrons were being first described by R. Q. Twiss (1920-2005) [34], J. Schneider (1931-) [35], and A. V. Gaponov (1926-) [36]. The first experimental identification of the azimuthal bunching mechanism for fast-wave emission was performed in 1964 by J. L. Hirshfield and J. M. Wachtel [37], who named the device an electron cyclotron maser (ECM).

Gyrotron Oscillators

The first practical high-power ECM configuration was developed in a form of a gyrotron oscillator in the former Soviet Union at the IAP by the mid-1960s, inaugurating a new era for VEDs. This source operated at the fundamental harmonic ($n = 1$) of the electron cyclotron frequency, delivering 6 W CW at 8.8 GHz with a beam voltage of $V_b = 8$ kV. The source also at the second cyclotron harmonic ($n = 2$), producing

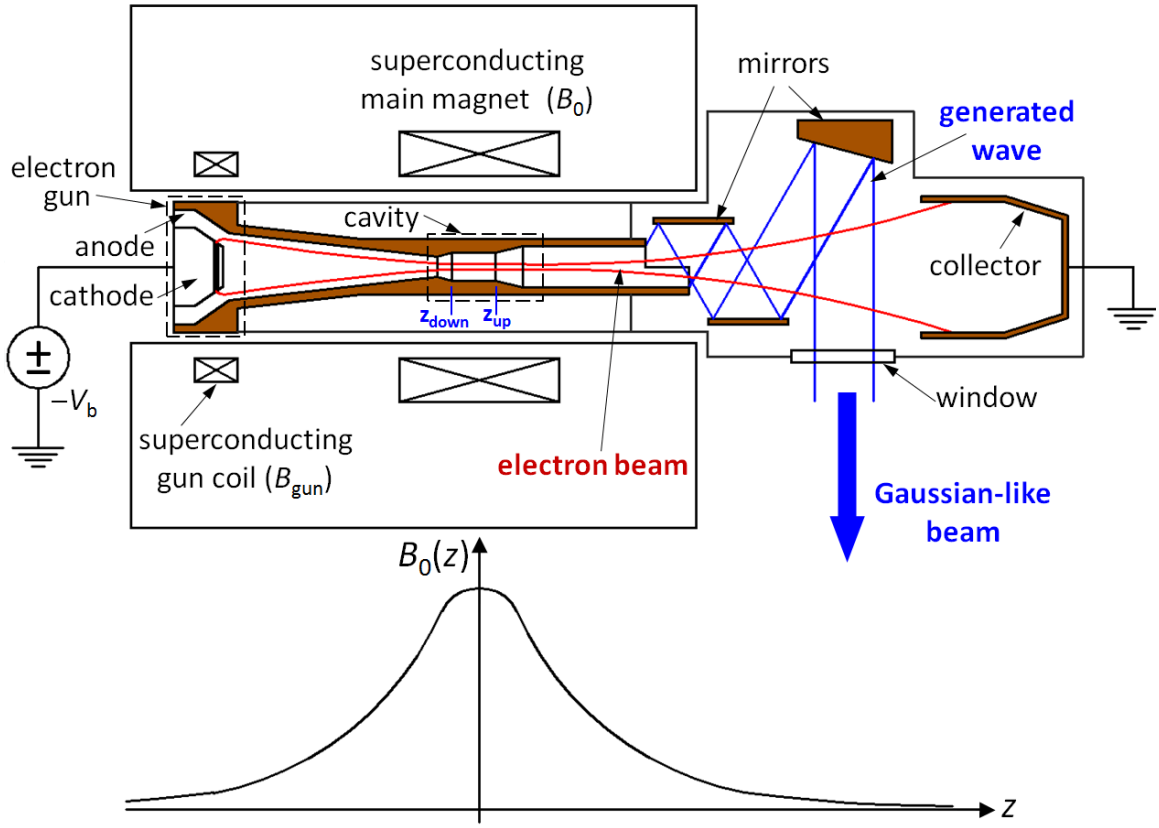

Figure 1-6: Configuration of a gyrotron oscillator and associated superconducting magnetic field profile $B_0(z)$ as a function of the longitudinal distance z.

190 W CW at 25 GHz with $V_b = 19$ kV. This first gyrotron incorporated several features still existent in present-day gyrotrons such as a magnetron injection gun (MIG), a region for beam formation, and an open resonator [38].

The configuration of a modern gyrotron is detailed in Fig. 1-6. Electrons are thermionically emitted from a cathode in a MIG and an initial transverse velocity is imparted due to the crossed static electric and magnetic fields at the gun location. After being accelerated to an usually weakly relativistic energy ($\gamma \lesssim 1.25$) due to a potential difference $-V_b$ applied between the cathode and anode electrodes, electrons follow the magnetic field lines in cyclotron motion and their transverse velocity increases in exchange of their axial velocity as the hollow electron beam is compressed until it reaches the gyrotron cylindrical cavity.

Once at the cavity, electrons may excite a transverse electric $\mathrm{TE}_{m,p,q}$ cylindrical mode and transfer part of their perpendicular energy to the wave. The indices m,

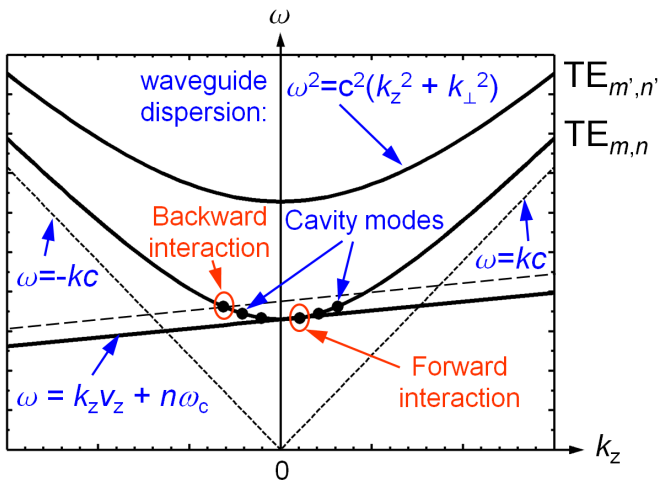

Figure 1-7: Dispersion diagram of a gyrotron oscillator operating at an electron cyclotron harmonic n and a waveguide mode $\mathrm{TE}_{m,n}$

p, and q denote the number of azimuthal, radial, and axial variations of the cavity mode, respectively. Modes with negative azimuthal number m designate modes that azimuthally counter-rotate with respect to the electron gyration in a static magnetic field. On the other hand, modes with a positive m represent co-rotating modes with respect to the electron gyration. The amount of transverse energy in the beam depends on the ratio of transverse electron velocity $v_\perp$ to axial electron velocity v_z, known as pitch factor $\alpha = v_\perp/v_z$, at the entrance of the interaction circuit. The parameter α is usually less than 2 in order to prevent reflections of the electron beam due to the lack of axial energy to overcome the magnetic hill determined by the external static magnetic field profile.

Some requirements must be observed for a net energy transfer from the beam to the wave to occur and for oscillations to be established. First, the beam-wave synchronism condition stated in Eq. (1.1) and shown in the dispersion diagram in Fig. 1-7 must be fulfilled in order to allow interaction over distances longer than the wavelength.

Second, the power transferred from the beam to the wave should be equal to or greater than the cavity losses, allowing oscillations to start. Threshold conditions for self-oscillations depend on cavity losses and the cavity interaction length, and also depend on beam parameters such as beam current, transverse beam energy, and beam

radius. These parameters determine the start oscillation current of the gyrotron as it will be discussed in Chapter 2.

Third, a feedback mechanism is necessary for oscillations to build up and sustain. In gyrotrons, this feedback mechanism is provided by reflections at both resonator ends. The forward-wave component of a resonant mode will interact with electrons and be reflected at the resonator end, becoming a backward wave. At the other cavity end, the backward wave will turn to a forward wave and interact with the beam again. This closed loop allows the wave amplitude to grow from noise level until it reaches steady state where the power transferred from the beam to the microwave equalizes the cavity losses. Another feedback mechanism for oscillations is an internal feedback loop between forward-moving electrons and a backward wave propagating with a group velocity opposing the electron axial motion. This condition is represented in the dispersion diagram in Fig. 1-7 and it forms the basis of a gyro-BWO oscillator [39].

In gyrotrons, electrons usually interact with waves close to cutoff as shown in the dispersion diagram in Fig. 1-7. These waves have a small axial wavenumber k_z and that prevent the broadening of the cyclotron resonance band associated with the Doppler shift term $k_z v_z$ and the electron axial velocity spread, allowing a better efficiency [40]. As a consequence, the synchronism condition in gyrotrons can be approximated as $f \approx n f_c$, where $f_c = (eB_0)/(2\pi m_e \gamma) = 27.9924 B_0/\gamma$ GHz/T is the electron cyclotron frequency in the cavity region. As detailed in Chapter 2, formation of electrons bunches in the decelerated phase of the electric field for a net energy transfer to the wave requires $\omega \gtrsim n\omega_c$.

Although TM cylindrical modes can also be excited in gyrotron resonators, their threshold for oscillations is $\approx 1/\beta_z^2$ higher than the threshold of TE modes [38, 41] and their associated beam-wave interaction is weaker since the TM transverse electric field scales as k_z/k. TM modes have been observed in few relativistic gyrotron experiments as pointed out in [42] and references therein.

Unlike conventional microwave tubes where an external static magnetic field is primarily utilized to confines the electron beam, in gyrotrons the external magnetic field

not only confine the beam but its value at the interaction region basically determines the frequency of the device $f \approx nf_c$. This marks another difference between gyrotrons and slow-wave devices besides azimuthal bunching and the use of overmoded smooth waveguide structures for fast-wave emission.

After the interaction, part of the microwaves will be dissipated in the cavity and the other portion will diffract out of the resonator, constituting the output power. Many gyrotrons feature internal converters to transform the cylindrical cavity mode into a Gaussian-like microwave beam as pioneered by S. N. Vlasov in 1975 [43] and later improved by G. G. Denisov in 1992 [44]. After exiting the gyrotron through a transparent window, the Gaussian output microwave beam can be transmitted to the final destination in a low-loss way using a set of mirrors and/or waveguides. Finally, the spent electron beam is collected, closing the power supply circuit.

Since its conception in the 1960s, gyrotrons have experienced rapid development which led to MW-level sources motivated by applications such as plasma heating. In addition to the aforementioned milestones, other improvements such as the use of CVD (chemical vapor deposition) diamond windows has enabled gyrotrons to handle higher output powers [45]. For instance, a 170-GHz gyrotron oscillator developed for the electron cyclotron heating and current drive (ECH-CD) system of the international fusion reactor ITER achieved an output power of 1 MW during 800 s with an efficiency of 55% [46] using a single-stage depressed collector. Recently, 2.2 MW peak power with efficiency of 30% has been obtained in a 170-GHz coaxial-cavity gyrotron for ITER operating in a pulse length of 1 ms and using a non-depressed collector [47].

Gyrotrons operating at the second cyclotron harmonic in CW regime have reached 2.4 kW at 157 GHz, 4.3 kW at 250 GHz, and 1.5 kW at 326 GHz, with efficiencies of 9.5%, 18%, and 6.2%, respectively [42, 48]. For pulsed operation, second-harmonic gyrotrons have achieved powers levels of 1-52 kW at discrete frequencies between 209 GHz to 576 GHz [42, 49, 50]. The maximum power of 52 kW was obtained at 349 GHz [50]. Efficiencies for these pulsed experiments were around or below 10%.

Gyrotron radiation at frequencies above 1 THz has been demonstrated at both fundamental and higher cyclotron harmonics. Experiments performed with a pulsed

magnet at the IAP, Nizhny Novgorod, Russia, radiated a fundamental harmonic mode at 1.022 THz with an output power of 1.5 kW and efficiency of 2.2% in pulses of 50 μs [51]. Radiation at 1.08 THz has been also obtained in a CW second-harmonic gyrotron at the University of Fukui, Fukui, Japan [52]. In addition, a third-harmonic gyrotron employing an axis-encircling electron beam, an arrangement also known as a large-orbit gyrotron (LOG), emitted 1.0 THz with peak power of 400 W in pulses of about 8 μs with efficiency of 0.7% [53].

Although operation in a high-order mode is advantageous in terms of breakdown and power handling, it brings forth the issue of mode competition. Mode selection in gyrotrons is often achieved by magnetic field selection and/or proper selection of the beam radius so that the start current of parasitic modes is higher than the operating current. Meanwhile other gyrotron interaction structures with sparser mode density than that of a cylindrical cavity have been tested to tackle the mode competition problem. Examples of such developments include a 140-GHz gyrotron using a PBG cavity, where no competing modes were observed in a frequency range of 30% about the operating mode [3], and a 140-GHz gyrotron utilizing a confocal resonator [4].

To this date, most of the experimental data available for oscillators coined as gyro-BWOs were taken at frequencies below 35 GHz [42]. One exception was a pioneering attempt made at the Massachusetts Institute of Technology (MIT), Cambridge, MA, USA, to build a pulsed 140-GHz fundamental-harmonic gyro-BWO. This device generated 2 kW of output power with an efficiency of 2%. Discontinuous frequency tuning with beam voltage reached a total range of 13 GHz [54]. Second-harmonic gyro-BWOs have been built at the IAP, where a 25-GHz CW gyro-BWO using a helically corrugated waveguide produced 7 kW of output power with an efficiency of 15% and magnetic tuning range of 2.2 GHz [55]. An attempt to scale this technology to the W-band is in progress [56]. This gyro-BWO review excludes gyrotrons that can be regarded as a reflective-type gyro-BWO due to interaction with backward waves.

Gyro-Amplifiers

CRMs can also be built in an amplifier configuration taking the form of gyroklystrons, gyrotwystrons, and gyro-TWTs. Gyroklystrons have been developed at frequencies up to 94 GHz, which is a frequency of interest for radars and communications due to the lower microwave absorption in the air by water and oxygen molecules, forming an atmospheric window. At 94 GHz, output powers from several tens of kilowatts to several hundreds of kilowatts have been obtained for gains up to 48 dB and bandwidths up to 0.75% [42]. The maximum efficiency obtained at this frequency was 34%.

Gyrotwystrons, which uses an input cavity for electron bunching like in a gyroklystron and an output waveguide section for larger bandwidth like in a gyro-TWT, have also been developed at 94 GHz for radar applications such as the MIT Lincoln Laboratory Haystack radar. This gyrotwystron produced 55 kW with an efficiency of 14.9% and a gain of 30 dB. The bandwidth obtained was twice as much as that of a gyroklystron, reaching 1.6% [57, 58].

Another gyro-amplifier being considered for radar applications is the gyro-TWT. The main feature of this device is its wide bandwidth, where 7.7 % bandwidth has been obtained in a 94-GHz gyro-TWT producing 1.5 kW with a gain of 42 dB and efficiency of 4.2% [58, 59].

Pioneering efforts are being made at MIT where gyro-TWTs are being developed at 140 GHz [60, 61], and 250 GHz [62] for spectroscopic applications such as nuclear magnetic resonance (NMR) and electron paramagnetic resonance (EPR). The 140-GHz amplifier utilizes overmoded confocal waveguide sections integrated with severs in a single block, where the sever loss mechanism relies on diffraction and not on microwave absorption by a lossy material. The role of severs was discussed in Section 1.2.4. The 140-GHz gyro-TWT has produced an output power of 820 W with bandwidth of 1.1% and gain of 34 dB with efficiency of 1% [61]. The 250-GHz gyro-TWT design proposes a high-gain single-stage PBG traveling-wave structure for lower-order mode suppression [62]. More details about this spectroscopic application, namely sensitivity enhanced nuclear magnetic resonance via dynamic nuclear

polarization (DNP/NMR), is given next.

1.3 Dynamic Nuclear Polarization (DNP)

Nuclear magnetic resonance is a spectroscopic tool employed in several areas of science including physics, chemistry, biology, materials science, and medicine. For the commonly studied spin $^1/_2$ nuclei such as protons (^{1}H), the NMR signal is proportional to the difference of population between the N_+ spins occupying the low energy level and the N_- spins in the high energy level. In thermal equilibrium, the relative population of these two states is given by Boltzmann's statistics as $N_-/N_+ = \exp(\Delta E/k_B T_s)$, where k_B is the Boltzmann constant, T_s is the sample temperature, and $\Delta E = \hbar\gamma_p B_{NMR}$ is the Zeeman energy splitting with $\hbar$ denoting Planck's constant, $\gamma_p = 2.675222 \times 10^8$ rad/s·T the proton gyromagnetic ratio, and B_{NMR} the static magnetic field applied to the NMR sample. In terms of frequency, the Zeeman energy splitting $\Delta E = hf_p$ can be determined by the proton Larmor frequency $f_p \approx 42.577 B_{NMR}$ MHz/T. The small Zeeman energy splitting associated with the nuclear spin results in a small polarization, limiting the sensitivity of NMR spectroscopy. For example at 300 K and 11.74 T, protons exhibit a polarization $P = (N_+ - N_-)/(N_+ + N_-) = \tanh(\Delta E/2k_B T_s)$ of 0.004% while electrons have a much higher one 2.6%.

One technique that exploits this property in order to enhance the signal-to-noise (SNR) ratio in NMR experiments is dynamic nuclear polarization. This technique consists of transferring the large polarization of exogenous or endogenous electron spins to the nuclear spins of a sample of interest by irradiating electromagnetic waves at a frequency close to the electron Larmor frequency $f_e \approx 28.024 B_{NMR}$ GHz/T. The electron Larmor frequency is also close to the electron cyclotron frequency. In theory, the maximum DNP enhancement attainable is given by the ratio f_e/f_p, which is ∼660 for protons [63, 64]. Polarization mechanisms in DNP/NMR experiments include the Overhauser effect, the solid effect, the cross effect, and thermal mixing, which are reviewed in Ref. [65].

In order to combine the signal enhancement provided by DNP with the improved spectral resolution and sensitivity in contemporary NMR spectrometers operating at magnetic fields $\geqslant$ 5 T, microwave sources radiating at frequencies $\geqslant$ 140 GHz are required [65]. These sources should deliver several watts to several tens of watts of output power in long-pulse or CW operation for an efficient transfer of polarization [66, 67]. Power and frequency fluctuations in the source should be kept below 1% and 1 MHz, respectively, so that long-term signal averaging can be carried out in DNP experiments [68].

As DNP depends on the electron spin resonance to drive the polarization of nuclear spins, it is paramount the ability to sweep the microwave source frequency within the EPR linewidth for a fixed B_{NMR} so that the operating point that maximizes the DNP enhancement can be found. Optimization of the DNP signal is also possible by sweeping the NMR magnetic field while keeping the frequency of the microwave source constant if sweep coils are installed in the NMR spectrometer. Sweeping B_{NMR} is a procedure that spends a considerable amount of liquid helium, it poses a risk of quenching the NMR magnet, and it requires further verification of the NMR field homogeneity once the procedure is finalized [69]. For these reasons, sweeping the frequency of the microwave oscillator is preferred. In addition, tunable sources would permit the implementation of DNP in NMR spectrometers without the need for sweep coils. A review of available sources in the frequency of interest for high-field DNP/NMR is presented below.

1.4 State of the Art of Submillimeter-Wave Sources

Among submillimeter sources available to date, solid-state sources such as IMPATT and Gunn diodes have power capability limited to hundreds of milliwatts and tens of milliwatts at 140 GHz, respectively, dropping to a few milliwatts at 300 GHz [70]. A solid-state DNP source consisting of an oscillator connected to an amplifier and a chain of frequency multipliers was able to deliver a maximum output power of 33 mW at 264 GHz with a 3-dB frequency tuning range of 13.9 GHz [71]. One of the factors

for limited output power in solid-state oscillators is the constrained input beam power. While the beam voltage is limited by breakdown, the collisional flow of electrons in the lattice restricts the beam current due to the saturated electron drift velocity, which is on the order of $\beta \sim 0.001$ for typical semiconductor doping concentration [70]. Another boundary is set by the maximum operating temperature of the device, which constrains the total beam power and the amount of heat associated with ohmic loss from collisional flow.

Optically pumped far-infrared gas lasers can provide a series of discrete lines between 0.16 and 7.5 THz [72], with a maximum power of 1.2 W at 2.5 THz [73] reducing to a few milliwatts below 600 GHz in commercial versions [74]. Another type of laser able to emit in the submillimeter band is the quantum cascade laser (QCL). Unlike conventional lasers that have their emission lines determined by the properties of the gain medium material, QCLs can have their emission frequency tailored by the thickness of alternate semiconductor layers that form quantum wells and control conduction intersubbands for cascaded electron transition. It has been demonstrated that QCLs can generate ∼15 mW CW at frequencies near 2 THz [75] and these lasers are able to radiate at frequencies as low as 680 GHz with the assistance of an external magnetic field [76]. One factor not favorable for THz lasers is the low energy of the photon in this part of the electromagnetic spectrum (1 THz = 4 meV).

In addition to solid-state oscillators and lasers, conventional microwave tubes also have limited power capability especially at submillimeter wavelengths. As outlined in Section 1.2, conventional microwave tubes have circuits with features smaller than the wavelength, which scale down with increasing frequency, limiting the average power capability of theses devices and making their fabrication more involved. For example, even though commercially available extended-interaction oscillators are able to generate 50 W of power at 140 GHz at continuous duty, the output power of these devices reduces to 6 W at 220 GHz [17]. Backward-wave oscillators (BWOs), which have covered frequencies up to 1.4 THz, follow a similar trend with power dropping from about 10 W at 140 GHz to 1 W at 300 GHz [32]. Oscillators based on diffraction radiation such as orotrons can provide CW radiation up to 0.1-0.5 W at 300-375 GHz

[25].

On the other hand, fast-wave vacuum electron devices such as gyrotrons allow interaction between electrons and waves with superluminal phase velocity. These fast waves are supported by overmoded smooth waveguides, which are simpler to fabricate and able to handle the average power required for high-field DNP/NMR and beyond as exemplified in Section 1.2.5. Free electron lasers can also provide radiation at submillimeter frequencies [77]. However, the main disadvantages of FELs are their bulkiness and cost since they require to be driven by an accelerator.

1.5 Gyrotrons for DNP

Gyrotrons were first developed for high-field DNP/NMR at MIT in the early 1990s initially at 140 GHz [63] and later at 250 GHz [78], corresponding to 211- and 380-MHz ^{1}H NMR frequencies, respectively. These gyrotrons operate at the fundamental harmonic of the cyclotron frequency and have generated 14 W at 140 GHz [79, 80], and 7 W at 250 GHz [68] using low beam power (300 W) and low beam current (25 mA). Long-term continuous operation with stable output power and frequency has been demonstrated for both gyrotrons. In particular, the 250-GHz gyrotron has achieved uninterrupted and stable CW operation for a period of 21 days [68]. The possibilities and results [63–68] provided by this new instrumentation have sparked the interest of other research laboratories [81–86] and companies [87–89], around the world, which are employing or developing gyrotrons for DNP/NMR spectrometers. A compilation of developed gyrotrons for high-field DNP/NMR is given in Table 1.1.

1.5.1 Second-Harmonic Operation

In order to extend the applicability of DNP/NMR to higher fields, the expensive cost of 10-23-T Nb_3Sn superconducting magnets can be avoided by operating the gyrotron at a cyclotron harmonic while utilizing less expensive NbTi superconducting magnets with fields up to 10 T. However, operation at a cyclotron harmonic brings forth extra challenges due to the lower beam-wave interaction efficiency for a given

beam power (see Section 1.2.5 - Gyrotron Oscillators), higher start oscillation current, and additional competition with neighboring lower-harmonic modes as detailed in Chapter 3. The harmonic gyrotron option for DNP was first considered at MIT with the development of a second-harmonic 460-GHz gyrotron for a 700-MHz ^{1}H NMR system in 2004 [90]. The first version of this gyrotron was able to generate up to 8.4 W of output power for a 12.4-kV 135-mA electron beam. The start current of the operating mode $TE_{0,6}$ was measured to be 67 mA, and stable continuous operation was demonstrated for a period of 1 hour [91]. Other second-harmonic gyrotrons were developed recently at the University of Fukui, Fukui, Japan [81, 84, 85] and by the Russian company GYCOM [88, 89]. Prospects to employ DNP to even higher NMR frequencies may be envisaged from a recent demonstration of 1-THz generation from a CW second-harmonic gyrotron [52].

1.5.2 Frequency Tunability

As mentioned in Section 1.3, the ability to continuously tune the gyrotron frequency is of great interest for DNP/NMR since it simplifies DNP operation by not requiring the NMR magnet to be swept. A tunable gyrotron also allows DNP to be implemented in NMR spectrometers without sweep coils. Gyrotrons usually employ resonators with high quality factor Q for efficient beam-wave interaction. However this condition poses a challenge if continuous frequency tunability on the order of a 1 GHz or more is a matter of concern. Following the dispersion diagram in Fig. 1-7, the gyrotron frequency can be tuned basically either by cavity perturbation or by changing the electron cyclotron frequency via magnetic or voltage tuning.

Cavity perturbation can be realized by altering the cavity geometry, for example. As gyrotrons operate at frequencies close to cutoff where $k_\perp \gg k_z$, the operating frequency of the device is relatively insensitive to the cavity length. For this reason, tunability by changing the cavity radius is preferred, which can be devised in a quasi-optical structure [92] or a split-cavity configuration [93–95]. Spurious second-harmonic emission at 200 GHz was observed simultaneously with the design fundamental mode in a 100-GHz quasi-optical pulsed gyrotron [96], where a continuous

tuning range of 1.6 GHz and 0.88 GHz were obtained for the second-harmonic and fundamental modes, respectively, as a function of the separation between the mirrors forming the quasi-optical interaction structure. For the split-cavity CW gyrotron reported in [94], which could be step tunable over the 100-325 GHz frequency range, continuous tunability less than 2 GHz was observed for a given fundamental-harmonic mode. A critical issue of the split structure is the precise alignment required between the two cavity halves and the need of additional vacuum feedthroughs depending on the implementation.

In gyrotrons the tuning range associated with a single $TE_{m,p,q}$ cavity mode is limited by its Q factor [97], which is often on the order of a few thousands to tens of thousands. Considering this fact, continuous broadband tunability may be achieved by exciting successive cavity modes that are close to each other in frequency as the cyclotron frequency is swept via magnetic or voltage tuning. In gyrotron cavities $TE_{m,p,q}$ modes that only differs by the axial mode number q have close eigenfrequencies following the condition $k_z \ll k_\perp$. This scheme for continuous frequency tunability was demonstrated in the MIT 250- and 460-GHz gyrotrons with the excitation of successive high-order axial modes as a function of magnetic field [68, 90]. While a tuning range broader than 2 GHz was observed for fundamental-harmonic modes, the continuous frequency tunability of second-harmonic modes was limited to a mere 50 MHz. Wideband magnetic tuning, which is similar to the tuning reported in [90], has recently been reported in a fundamental-harmonic 140-GHz gyrotron oscillator, with up to 6 GHz of magnetic tuning obtained [82]. For a low-frequency gyrodevice operating at the second cyclotron harmonic, a smooth broadband magnetic tuning of 2.2 GHz has been observed in a 25-GHz CW gyro-BWO [55].

1.6 Motivation of this Research

The motivation of this research is the development of a CW 330-GHz gyrotron oscillator operating at the second cyclotron harmonic with broadband continuous frequency tunability for DNP experiments in a 500-MHz ^{1}H NMR spectrometer without sweep

coils installed. The microwave frequency that maximizes the DNP/NMR enhancement corresponds to 329.4 GHz. The CW 330-GHz gyrotron should deliver several watts to several tens of watts of output power in a stable regime with a continuous tuning range of 1.5 GHz centered at the optimum DNP frequency of 329.4 GHz.

Despite the simpler implementation of continuous tuning via cyclotron frequency by using knobs already available to the gyrotron operator such as beam voltage and magnetic field, skepticism about adopting this approach was expressed considering the available experimental data in the early stage of this project with magnetic tuning restricted to 50 MHz for second-harmonic modes in high-frequency gyrotrons. Following details described in this thesis, this work demonstrated for the first time that a continuous tuning range $\geqslant 1$ GHz can be achieved via magnetic, voltage, and thermal tuning for second-harmonic modes in submillimiter-wave gyrotrons. This result constitutes a major advance in the state of the art of gyrotrons. Besides frequency tunability, other gyrotron features of interest for DNP/NMR were evaluated such as stability of the gyrotron output and field profile of the microwave output beam. After the major findings of this work were published [98–101], which are summarized in the highlighted rows of Table 1.1 and detailed in this thesis, a continuous magnetic tuning range of 0.5 GHz has been reported very recently for a second-harmonic mode in a 395-GHz gyrotron [84].

1.7 Thesis Outline

After introducing the rationale behind building a 330-GHz continuously tunable CW gyrotron operating at the second cyclotron harmonic for a spectroscopic application, additional details of the gyrotron operation are given in Chapter 2 including a qualitative description of the azimuthal electron bunching process. The second chapter also reviews a nonlinear single-particle theory to describe the beam-wave interaction in a structure with a fixed axial field profile, and a linear theory to determine the threshold current for oscillations. Additional tools utilized for the gyrotron design such as a code to determine the axial field profile in gyrotron cavities with the electron

beam absent and a self-consistent code for design under more realistic conditions are also mentioned.

Once the theoretical foundations are laid, the design of the different parts of the gyrotron is described in Chapter 3 including the superconducting magnet, the electron gun, the cavity interaction circuit, and the converter from a cylindrical waveguide mode to a Gaussian-like microwave beam for low-loss transmission to the desired application. Chapter 4 describes the experimental setup and diagnostics utilized in the characterization of the gyrotron. Experimental results for output power and frequency tunability as a function of magnetic field, beam voltage, and cavity cooling temperature are presented in this chapter. Other experimental data mentioned in this chapter include the start oscillation current of the operating mode, ohmic loss, frequency and power stability in long-run continuous operation, and the output microwave beam profile.

The design and evaluation of a 460-GHz second-harmonic CW gyrotron are presented in Chapter 5. This gyrotron also features broadband continuous frequency tunability and it provided valuable information for the design of the subsequent 330-GHz project described in the previous chapters. The thesis is finalized with conclusions and directions for future work in Chapter 6.

Table 1.1: CW gyrotrons for high-frequency DNP/NMR spectrometers

Year	Institution	Cyclotron harmonic n	Frequency (GHz)	Mode ($TE_{m,p,q}$)	V_b (kV)	I_b (mA)	Power (W)	Continuous frequency tuning (GHz)
1993	MIT [63, 79, 80]	1	140	$TE_{0,3,1}$	12.3	25	14	–
1998	MIT [68, 78]	1	250	$TE_{0,3,2}$	12.2	26	7	[a]
2004	MIT [90, 91, 102]	2	460	$TE_{0,6,1}$	12.4	135	8.4	0.05[b]
2007	Univ. of Fukui [81, 83]	2	395	$TE_{0,6}$	16.5	400	40	–
2008	**MIT (this thesis) [98, 101]**	**2**	**460**	$\mathbf{TE_{11,2}}$	**13**	**100**	**2-16**	**1.0**
2009	**MIT (this thesis) [98–100]**	**2**	**330**	$\mathbf{TE_{-4,3}}$	**13**	**190**	**1-19**	**1.2**
2009	Univ. of Fukui [82]	1	137	$TE_{1,2}$	19	400	5-63	6
2009	CPI, Bruker [87]	1	263	$TE_{0,3,1}$	12	75	90	0.1
2009	GYCOM [88, 89]	2	260	$TE_{-2,3}$	14	450	170	0.06
2009	Univ. of Fukui [85]	1 2	200 395	$TE_{4,2}$ $TE_{1,6}$	15 15	250 325	130 15	– –
2010	Univ. of Fukui [84]	1 2	395	$TE_{0,6}$	12	300	8-34 6-16	1.65 0.5

[a] Continuous magnetic tuning of up to 1.8 GHz observed in pulsed operation for fundamental-harmonic modes. Tunability for second-harmonic modes limited to 50 MHz.

[b] Continuous magnetic tuning of up to 2.2 GHz observed in pulsed and CW operation for fundamental-harmonic modes.

Chapter 2

Theory of Gyrotron Oscillators

After the introductory remarks that outlined the motivation and relevance of this research, this chapter reviews the theoretical basis necessary for the understanding and design of gyrotron oscillators. Section 2.1 gives more details than that provided in the previous chapter about the gyrotron operation, including a classical relativistic description of the gyrotron radiation mechanism. Interpretation of the ECM mechanism using a quantum approach is also possible as indicated in [38] and references therein. In the sequence, the electromagnetic fields and associated losses in a cylindrical resonant metallic structure that forms the gyrotron interaction circuit are derived in Section 2.2. Once the field configuration is known assuming a fixed axial profile in the interaction structure, figures of merit of the oscillator such as efficiency and threshold oscillation current can be estimated using single-mode, single-particle nonlinear and linear theories as outlined in Sections 2.3 and 2.4, respectively. An overview of a self-consistent code for gyrotron design under more realistic conditions is presented in Section 2.5.

2.1 Gyrotron Overview

The gyrotron oscillator configuration utilized in this work was shown schematically in Fig. 1-6. The electron beam is generated by thermionic emission from an indirectly heated ring cathode of radius r_c and slant length l_c, overcoming the work function

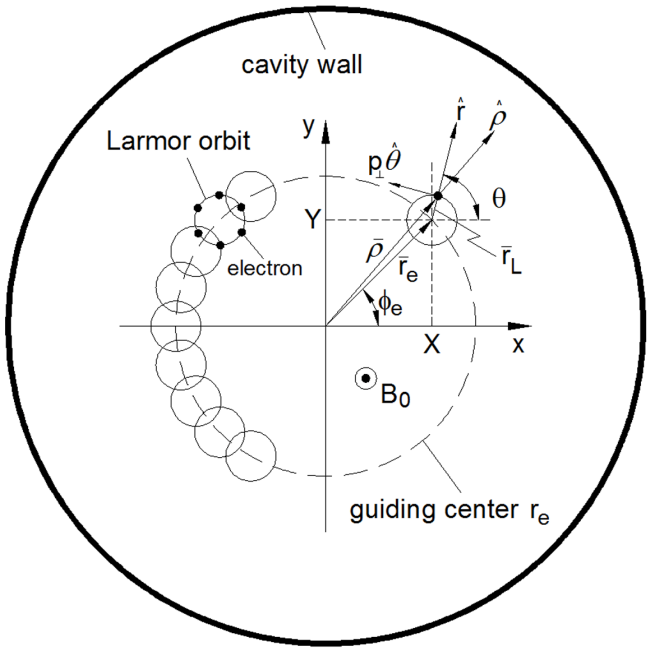

Figure 2-1: Cross-section of small-orbit electron beam with beam radius r_e, showing electrons gyrating in a Larmor orbit of radius r_L.

of the elements forming the emitting surface in a magnetron injection gun (MIG). A DC beam voltage $-V_b$ applied between the cathode and grounded anode electrodes accelerates the electrons, which have an initial transverse velocity due to the crossed configuration of the DC electric E_c and magnetic B_c fields at the emitter location denoted by the subscript c. A cross-section of the hollow electron beam is depicted in Fig. 2-1. While electrons follow the magnetic field lines created by the superconducting magnet in cyclotron motion along the drift section, the beam guiding center r_e is compressed following $r_e(z) = r_c(B_c/B_0(z))^{1/2}$, a result from Busch's theorem [103]. At the same time the electron transverse velocity $v_\perp$ is increased according to the adiabatic invariant quantity $p_\perp^2/B_0$, where p is the electron linear momentum [103].

The electron beam configuration utilized in this work is known as a small orbit beam since $r_L < r_e$. As outlined above, the small orbit beam can be generated using a MIG and a monotonic magnet field profile between the cathode and the gyrotron cavity provided by the superconducting magnet. Other gyrotrons called large orbit gyrotrons (LOG) utilize a large orbit electron beam or an axis-encircling beam where $r_L \geqslant r_e$. One of the main benefits of the large orbit scheme is the better mode

selectivity since an electron beam with $r_e = 0$ only interacts with co-rotating TE modes whose azimuthal index m is equal to the cyclotron harmonic n. [104]. This result follows from the beam-wave coupling coefficient, Eq. (2.64), derived in Section 2.3. However, the generation of an axis-encircling electron beam is more involved, requiring an electron gun with a reverse (cusp) of the magnetic field near the cathode or a kicker [53].

At the cavity entrance, the pitch factor $\alpha = v_\perp/v_z$ should be high since the electron beam will interact with a $\mathrm{TE}_{m,p,q}$ electromagnetic wave supported by the cavity at a frequency near cutoff, transferring part of its perpendicular kinetic energy to the wave. A pitch factor less than 2 is usually employed in order to avoid reflected electrons due to the magnetic mirror effect. Although TM cylindrical modes can also be excited, their threshold for oscillations is $\approx 1/\beta_z^2$ higher than the threshold of TE modes [38, 41]. Also the beam-wave interaction for TM modes is weaker than that of TE modes since the TM transverse electric field scales as k_z/k. Excitation of TM modes has not been observed in gyrotron oscillators operating in weakly or mildly relativistic conditions ($\gamma \lesssim 1.25$), which constitute the majority of gyrotrons [42]. Therefore only TE modes will be considered.

Two fundamental conditions are required for the generation of electromagnetic waves in the interaction region: bunching and synchronism. Azimuthal electron bunching in a Larmor orbit is a process stimulated by the wave and imparts an AC component to the DC electron beam. The AC current component will interact with the electromagnetic cavity field and a net energy transfer to the wave will occur if electrons remain in close synchronism with the wave.

The azimuthal bunching process is illustrated in Fig. 2-2 and it is a result from simulations performed using a single-mode single-particle nonlinear theory derived in Section 2.3. Here each frame was taken at a different axial location z along the cavity longitudinal axis and at a multiple of the microwave period $T = 2\pi/\omega$. As the microwave field E is synchronous with the second cyclotron harmonic ($\omega \approx 2\omega_c$), the electric field lines seen by the electron beam have a quadrupole configuration as demonstrated in Section 2.3. The interaction calculation was performed for an axial

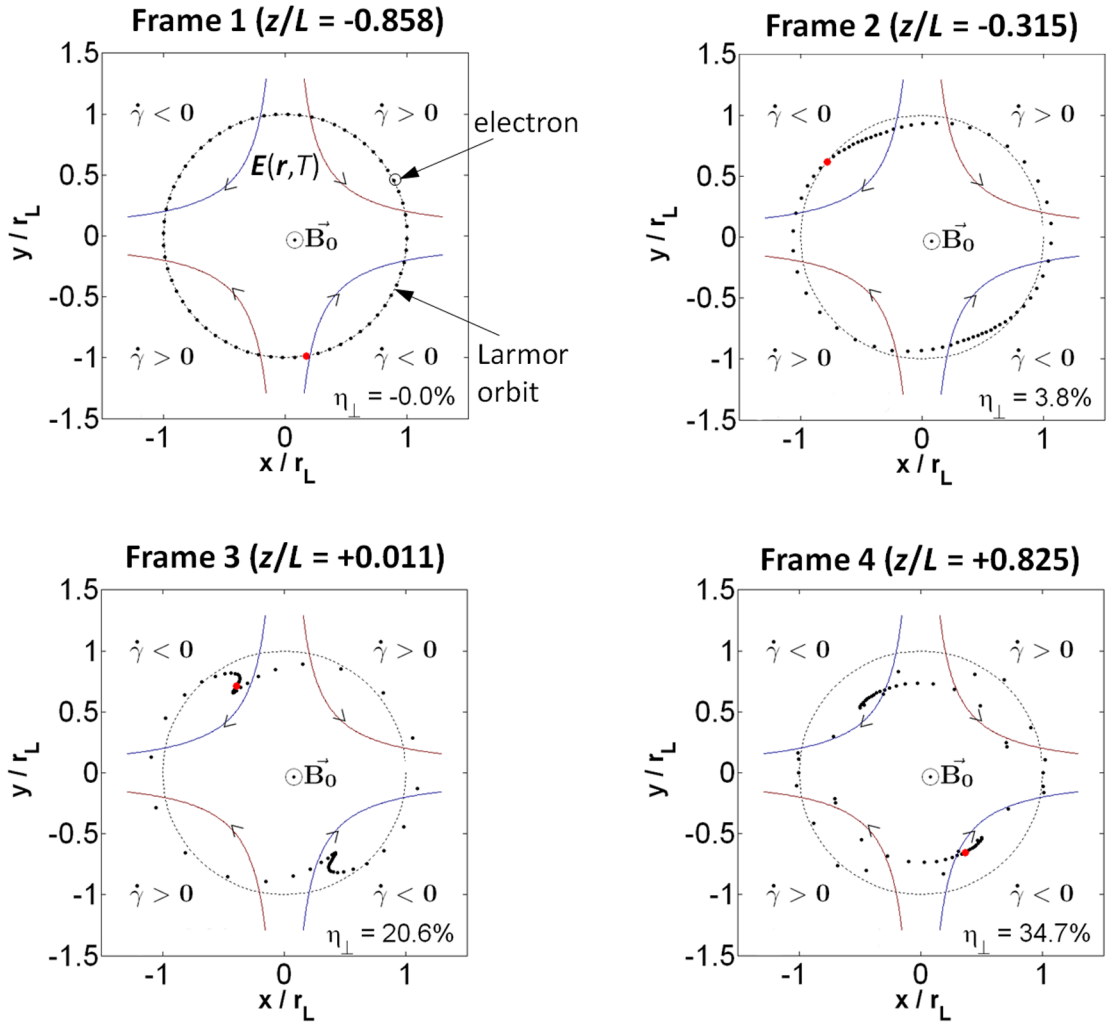

Figure 2-2: Azimuthal bunching for an electron beam interacting with a microwave field **E** synchronous with the second cyclotron harmonic ($n = 2$). The synchronous electric field component **E** has a quadrupolar configuration as shown by the electric field lines in each graph. Each frame was taken at a multiple of the microwave period T and at a different axial location z in the cavity interaction region. The orbital efficiency is denoted by $\eta_\perp$ and the simulation parameters are described in the text.

range of $-\sqrt{3}/2 < z/L < \sqrt{3}/2$ and it assumed a $\mathrm{TE}_{-4,3,1}$ cylindrical cavity mode with a Gaussian axial field profile $f(z) = \exp\left(-(2z/L)^2\right)$, where L is the cavity effective length. This cavity mode is the design mode for the 330 GHz gyrotron oscillator as described in Chapter 3 and it was assumed to already exist in the resonator with a normalized amplitude $F = 0.024$, simulating steady state operation above the minimum threshold for oscillations. The static magnetic field $B_0 = 5.99$ T is oriented along the cavity axis. The other simulation parameters are number of electrons = 64, $V_b = 10$ kV, $I_b = 190$ mA, $\alpha = 1.8$, $r_L = 50$ μm, $f = 330$ GHz, $r_e = 1.08$ mm, cyclotron harmonic $n = 2$, $L/\lambda = 31$, and cavity quality factor $Q \approx 9,000$. The code utilized for this simulation is based on a single-particle single-mode nonlinear gyrotron theory described in Section 2.3.

Frame 1 shows electrons at the cavity entrance randomly distributed around a Larmor orbit of Larmor radius $r_L = v_\perp/\omega_c$. Each individual Larmor orbit shares a common guiding center of radius r_e with electrons rotating counterclockwise. As electrons advance in the cavity, electrons in a region where $\mathbf{v}_\perp \cdot \mathbf{E} < 0$ or $\dot{\gamma} > 0$ are accelerated. This gain in energy will make these electrons rotate slower with an increased Larmor radius as it follows from the dependence of the cyclotron frequency $\omega_c \propto 1/\gamma$ and Larmor radius $r_L \propto \gamma v_\perp$ on beam energy. Meanwhile, electrons in the decelerated phase of the electromagnetic field, characterized by $\mathbf{v}_\perp \cdot \mathbf{E} > 0$ or $\dot{\gamma} < 0$, will lose energy and rotate faster with a decreased r_L as shown in Frame 2. This process leads to the formation of two electron bunches at the decelerated phase of the field as seen in Frame 3. Formation of two bunches follows from the synchronism between the microwave field and the second cyclotron harmonic. Extrapolation of this result may suggest that the number of bunches formed from the interaction with a given cyclotron harmonic is equal to the harmonic number [105]. Electron bunches will be located in the decelerated phase of the field for a net energy extraction to the wave as long as the microwave frequency is greater than the second cyclotron harmonic at the entrance of the cavity. The condition for synchronism and favorable beam-wave interaction can be summarized as $\omega \gtrsim 2\omega_{c0}$, where the subscript 0 denotes the value taken at the entrance of the gyrotron resonator. Frame 4 shows the distribution of

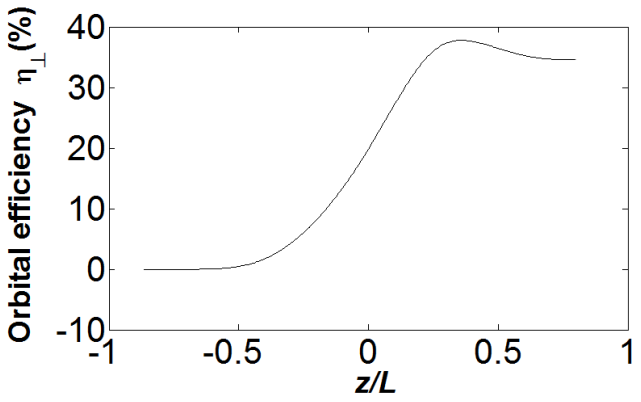

Figure 2-3: Orbital efficiency $\eta_\perp$ as a function of the normalized distance z/L for the same simulation parameters utilized in Fig. 2-2.

electrons at the exit of the cavity with final orbital efficiency of $\eta_\perp = 34.7\%$. The variation of the efficiency $\eta_\perp$ as a function of the normalized distance z/L can be seen in Fig. 2-3.

Part of the power transferred from the beam will diffract out of the resonator, constituting the output power P_{OUT} of the device, while the remaining portion P_{load} will be dissipated on the cavity walls. The diffractive loss is characterized by the diffractive quality factor Q_D and the ohmic loss is represented by the ohmic quality factor Q_O. Based on the aforementioned description, the gyrotron efficiency η can be written as [106]:

$$\eta = \frac{P_{OUT}}{V_b I_b} = \frac{\gamma_0 - \gamma_{out}}{\gamma_0 - 1} = \frac{\beta_{\perp 0}^2}{2(1-\gamma_0^{-1})}\eta_\perp \eta_{RF} \tag{2.1}$$

where the first term accounts for the amount of transverse beam kinetic energy available for interaction with a TE cavity mode and $\eta_\perp$ represents the beam-wave interaction efficiency. The last term η_{RF} denotes the microwave extraction efficiency from the gyrotron resonator and it depends on the cavity losses:

$$\eta_{RF} = \left(1 + \frac{Q_D}{Q_O}\right)^{-1} \tag{2.2}$$

For weakly relativistic operation where the beam energy at the entrance of the cavity fulfills $\beta_0^2 \ll 1$, Eq. (2.1) can be approximated as:

$$\eta \approx \left(\frac{\alpha_0^2}{1+\alpha_0^2} \right) \eta_\perp \eta_{RF} \tag{2.3}$$

After transferring part of its perpendicular energy to the electromagnetic wave, the spent beam is separated from the wave by an internal mode converter, and it is allowed to expand in the decaying field of the superconducting magnet until it is collected on a water-cooled copper collector at ground potential in a non-depressed collector configuration. The internal mode converter not only allows a reduction of the thermal load on the collector but also permits a better vacuum conductance throughout the tube, contributing to the CW operation of a gyrotron. Meanwhile the converter transforms the cylindrical waveguide into a Gaussian-like beam, which is guided to a transparent output window by a set of mirrors and sent to the NMR probe using a low-loss corrugated waveguide.

2.2 Gyrotron Interaction Structure

The gyrotron interaction structure considered here takes the form of a cylindrical cavity of radius r_{cav} and length L where the axial boundaries are defined by a section of downtapered waveguide at one cavity end and by a section of uptapered waveguide at the other cavity end as seen in Fig. 1-6. Modes excited by an electron beam in this resonant structure have the transverse pattern of a TE cylindrical waveguide mode with an axial field profile $f(z)$ along the cavity axis z. TM cavity modes will not be included due to the reasons outlined in Section 2.1.

2.2.1 Cavity Electromagnetic Fields

In a free-space medium without charge and current sources ($\rho = 0, \mathbf{J} = \mathbf{0}$) and with constitutive relations $\mathbf{B} = \mu_0 \mathbf{H}$, and $\mathbf{D} = \varepsilon_0 \mathbf{E}$, Maxwell's equation can be written as

below for a time-harmonic solution $\mathbf{E}(\mathbf{r},t) = \mathrm{Re}\{\mathbf{E}(\mathbf{r})e^{j\omega t}\}$ at a frequency ω:

$$\nabla \times \mathbf{E} = -j\omega\mu_0\mathbf{H} \tag{2.4}$$

$$\nabla \times \mathbf{H} = j\omega\varepsilon_0\mathbf{E} \tag{2.5}$$

$$\nabla \cdot \mathbf{E} = 0 \tag{2.6}$$

$$\nabla \cdot \mathbf{H} = 0 \tag{2.7}$$

where $\mathbf{E}$ represents the electric field in V/m, $\mathbf{D}$ represents the electric displacement in C/m^2, $\mathbf{H}$ represents the magnetic field in A/m, $\mathbf{B}$ represents the magnetic flux density in Wb/m^2, $\varepsilon_0 = 8.854187817 \times 10^{-12}$ F/m is the permittivity of free space, and $\mu_0 = 4\pi \times 10^{-7}$ H/m is the permeability of free space. Following (2.6) and (2.7), $\mathbf{E}$ and $\mathbf{H}$ can be expressed as functions of the electric vector potential $\mathbf{F}$ and magnetic vector potential $\mathbf{A}$:

$$\mathbf{E} = -\nabla \times \mathbf{F} \tag{2.8}$$

$$\mathbf{H} = \nabla \times \mathbf{A} \tag{2.9}$$

Combining Eqs. (2.5) and (2.8), one can write the magnetic field $\mathbf{H}$ as:

$$\mathbf{H} = -j\omega\varepsilon_0\mathbf{F} + \nabla\phi^e \tag{2.10}$$

with ϕ^e denoting an arbitrary scalar function. Replacing (2.8) and (2.10) into (2.4) and making use of the Lorenz gauge condition:

$$\nabla \cdot \mathbf{F} - j\omega\mu_0\phi^e = 0 \tag{2.11}$$

one can obtain the wave equation for the electric vector potential $\mathbf{F}$:

$$\left(\nabla^2 + \omega^2\mu_0\varepsilon_0\right)\mathbf{F} = \mathbf{0} \tag{2.12}$$

where the fields are represented as:

$$\mathbf{E} = -\nabla \times \mathbf{F} \tag{2.13}$$

$$\mathbf{H} = -j\omega\varepsilon_0\mathbf{F} - j\frac{\nabla\left(\nabla\cdot\mathbf{F}\right)}{\omega\mu_0} \tag{2.14}$$

In cylindrical coordinates (ρ, ϕ, z) and considering $\mathbf{F} = \psi\hat{z}$ for the TE case, the electromagnetic fields $\mathbf{E}$ and $\mathbf{H}$ are written as:

$$\mathbf{E} = -\frac{1}{\rho}\frac{\partial\psi}{\partial\phi}\hat{\rho} + \frac{\partial\psi}{\partial\rho}\hat{\phi} \tag{2.15}$$

$$\mathbf{H} = -\frac{j}{\omega\mu_0}\frac{\partial^2\psi}{\partial\rho\partial z}\hat{\rho} - \frac{j}{\omega\mu_0\rho}\frac{\partial^2\psi}{\partial\phi\partial z}\hat{\phi} - \frac{j}{\omega\mu_0}\left(\omega^2\mu_0\varepsilon_0\psi + \frac{\partial^2\psi}{\partial z^2}\right)\hat{z} \tag{2.16}$$

where the function ψ can be found as a solution of the wave equation $\left(\nabla^2 + \omega^2\mu_0\varepsilon_0\right)\psi = 0$ using separation of variables $\psi(\rho,\phi,z) = AR(\rho)\Phi(\phi)Z(z)$ where A is a constant:

$$\frac{1}{\rho R}\frac{\partial}{\partial\rho}\left(\rho\frac{\partial R}{\partial\rho}\right) + \frac{1}{\rho^2\Phi}\frac{\partial^2\Phi}{\partial\phi^2} + \frac{1}{Z}\frac{\partial^2 Z}{\partial z^2} + \omega^2\mu_0\varepsilon_0 = 0 \tag{2.17}$$

which results in the following set of equations for each function $R(\rho)$, $\Phi(\phi)$, and $Z(z)$, after using the dispersion relation $k^2 = k_\perp^2 + k_z^2$ (1.2):

$$\frac{\partial^2\Phi}{\partial\phi^2} + m^2\Phi = 0 \tag{2.18}$$

$$\frac{\partial^2 Z}{\partial z^2} + k_z^2 Z = 0 \tag{2.19}$$

$$\rho\frac{\partial}{\partial\rho}\left(\rho\frac{\partial R}{\partial\rho}\right) + \left(k_\perp^2\rho^2 - m^2\right) = 0 \tag{2.20}$$

Combining the solution of each equation, $\Phi(\phi) = e^{-jm\phi}$, $Z(z) = f(z)$, and $R = J_m(k_\perp\rho)$, where $J_m(x)$ is a Bessel function of the first kind and m is the azimuthal mode number, the solution for the wave equation (2.12) is written as:

$$\psi(\rho,\phi,z) = AJ_m(k_\perp\rho)e^{-jm\phi}f(z) \tag{2.21}$$

Once the function ψ is known with the constant A chosen as $A = E_1/k_\perp$, where E_1 is the electric field amplitude, the expression for each field component of a TE cylindrical waveguide mode can be found from Eqs. (2.15) and (2.16):

$$
\begin{aligned}
E_\rho &= jE_1 \frac{m}{k_\perp \rho} J_m(k_\perp \rho) e^{-jm\phi} f(z) && (2.22)\\
E_\phi &= E_1 J'_m(k_\perp \rho) e^{-jm\phi} f(z) && (2.23)\\
E_z &= 0 && (2.24)\\
H_\rho &= -jE_1 \frac{1}{\omega \mu_0} J'_m(k_\perp \rho) e^{-jm\phi} f'(z) && (2.25)\\
H_\phi &= -E_1 \frac{m}{\omega \mu_0 k_\perp \rho} J_m(k_\perp \rho) e^{-jm\phi} f'(z) && (2.26)\\
H_z &= -jE_1 \frac{k_\perp}{\omega \mu_0} J_m(k_\perp \rho) e^{-jm\phi} f(z) && (2.27)
\end{aligned}
$$

From the boundary conditions $E_\phi(\rho = r_{cav}) = 0$ and $H_\rho(\rho = r_{cav}) = 0$, one has $J'_m(k_\perp r_{cav}) = 0$, which yields the following expression for the transverse wavenumber $k_\perp$:

$$k_\perp = \frac{\nu'_{mp}}{r_{cav}} \tag{2.28}$$

where p denote the radial mode number, and ν'_{mp} is the pth non-vanishing zero of the derivative of the Bessel function $J'_m(x)$.

2.2.2 Cavity Losses

As mentioned previously, there are two sources of losses in the gyrotron resonant structure: ohmic and diffractive losses. The power deposited in the cavity walls as ohmic loss is represented by the quantity P_{load} while the power lost by diffraction corresponds to the output power P_{OUT}. These two quantities constitute the total power lost $P_T = P_{load} + P_{OUT}$ in the resonator and they relate to the cavity quality factor Q at a cavity resonant frequency ω as:

$$Q = \frac{\omega U}{P_T} = \frac{\omega U}{dU/dt} \tag{2.29}$$

where U denotes the stored energy in the gyrotron resonator of volume V which is given by the following expression after utilizing Eqs. (2.22)-(2.24):

$$\begin{aligned} U &= \frac{\varepsilon_0}{2}\int_V |\mathbf{E}|^2 dV \\ &= E_1^2 \varepsilon_0 \frac{\pi}{2k_\perp^2}(\nu_{mp}'^2 - m^2) J_m^2(\nu_{mp}') \int_0^L |f(z)|^2 dz \end{aligned} \tag{2.30}$$

If one represents the ohmic loss by its ohmic quality factor $Q_O = \omega U/P_{load}$ and the diffractive losses by its diffractive quality factor $Q_D = \omega U/P_{OUT}$, the resonator Q-factor can be rewritten as:

$$\frac{1}{Q} = \frac{1}{Q_O} + \frac{1}{Q_D} \tag{2.31}$$

and the cavity losses can be related as:

$$\frac{P_{load}}{P_{OUT}} = \frac{Q_D}{Q_O} \tag{2.32}$$

For a gyrotron cavity with metallic walls with finite conductivity σ, the ohmic loss P_{load} on the cavity surface S can be evaluated as:

$$P_{load} = \frac{1}{2\sigma\delta}\int_S |\mathbf{H_{tan}}|^2 dS \tag{2.33}$$

with the skin depth δ being:

$$\delta = \sqrt{\frac{2}{\omega\mu_0\sigma}} \tag{2.34}$$

Replacing Eqs. (2.30), (2.33), and (2.34) in the expression for Q_O and using the gyrotron operating condition $k_z \ll k_\perp$, one obtains:

$$Q_O = \frac{r_{cav}}{\delta}\left(1 - \frac{m^2}{\nu'^2_{mp}}\right) \tag{2.35}$$

The diffractive quality factor can be computed considering the cavity decay time and absolute value of reflections R_{down} and R_{up} at the downtapered and uptapered ends of the resonator, respectively [41]:

$$Q_D = \frac{\omega L}{v_g(1 - R_{down}R_{up})} \tag{2.36}$$

Approximating the axial field profile by a sinusoid $f(z) = \sin q\pi z/L$ with q axial mode variations and axial wavenumber $k_z = q\pi/L$, and considering $v_{ph}v_g = c^2$ as well as $v_{ph} = \omega/k_z$, expression (2.36) can be rewritten as:

$$Q_D = \frac{4\pi}{q}\frac{(L/\lambda)^2}{(1 - R_{down}R_{up})} \tag{2.37}$$

In order to prevent electromagnetic waves in the gyrotron resonator from travelling toward the electron gun, which would compromise the quality of the incoming electron beam, it is reasonable to consider $R_{down} \simeq 1$. For high Q_D resonators, R_{up} can be approximated as $R_{up} \approx (k - k_z)/(k + k_z)$, which yield $(1 - R_{down}R_{up})^{-1} \sim q^{-1}(L/\lambda)$. Under these conditions, Q_D have a q^{-2} dependence on the axial mode number [107, 108]:

$$Q_D = \frac{4\pi}{q^2}\left(\frac{L}{\lambda}\right)^3 \tag{2.38}$$

Unlike gyrotrons operating at long wavelengths where losses are dominated by diffraction [109, 110], yielding $\eta_{RF} \sim 1$, the output power of submillimeter-wave gyrotrons can be severely reduced by ohmic loss.

2.2.3 Cold Cavity Parameters

The resonant frequency ω, the axial field profile $f(z)$ and the diffractive quality factor Q_D of a gyrotron resonator can be found by solving Eq. (2.19) as implemented in a computer code developed by [111] and utilized in this work. Considering that these solutions do not include the presence of an electron beam or any other source in Maxwell's equations like in Section 2.2.1, the code is referred here as a cold-cavity code.

For a gyrotron resonator where the waveguide radius is far from critical and weakly varying as a function of the longitudinal distance z, the dispersion relation (1.2) and one-dimensional wave equation of a single TE mode (2.19) without mode coupling can be rewritten as:

$$\left(\frac{\omega}{c}\right)^2 - k_\perp^2(z) = k_z^2(z) \tag{2.39}$$

$$\left[\frac{\partial^2}{\partial z^2} + k_z^2(z)\right] f(z) = 0 \tag{2.40}$$

If one assumes that the operating mode is cutoff in the downtapered section ($z < z_{down}$) and propagating in the uptapered section ($z > z_{up}$) (see Fig. 1-6), the appropriate radiation boundary condition at $z = z_{down}$ and $z = z_{up}$ are:

$$\left[\frac{\partial f(z)}{\partial z} - jk_z(z)f(z)\right]_{z=z_{down}} = 0 \tag{2.41}$$

$$\left[\frac{\partial f(z)}{\partial z} + jk_z(z)f(z)\right]_{z=z_{up}} = 0 \tag{2.42}$$

where $\mathrm{Re}(k_z) > 0$ when $\mathrm{Re}(k_z^2) > 0$, and $\mathrm{Im}(k_z) < 0$ when $\mathrm{Re}(k_z^2) > 0$. These conditions assume that the cavity cross section is far from critical ($\mathrm{Re}(k_\perp^2) \gg \mathrm{Im}(k_\perp^2)$) and weakly varying in the downtapered and uptapered sections ($dk_\perp/dz \ll k_\perp^2$).

The solutions of Eq. (2.40) that fulfill the boundary conditions (2.41) and (2.2.3) have complex eigenfrequencies. Following the field dependence on $\exp(j\omega t)$, the definition of quality factor in Eq. (2.29) and neglecting ohmic losses, the diffractive Q_D can be obtained as:

$$Q_D = \frac{\mathrm{Re}(\omega)}{2\mathrm{Im}(\omega)} \tag{2.43}$$

In order to solve Eq. (2.40) numerically, one can separate the real and imaginary parts and solve the following set of second order coupled differential equations:

$$\left[\frac{\partial^2}{\partial z^2} + \mathrm{Re}\left(\frac{\omega}{c}\right)^2 - k_\perp^2\right] \mathrm{Re}(f) = \mathrm{Im}\left(\frac{\omega}{c}\right)^2 \mathrm{Im}(f) \tag{2.44}$$

$$\left[\frac{\partial^2}{\partial z^2} + \mathrm{Re}\left(\frac{\omega}{c}\right)^2 - k_\perp^2\right] \mathrm{Im}(f) = -\mathrm{Im}\left(\frac{\omega}{c}\right)^2 \mathrm{Re}(f) \tag{2.45}$$

Although perturbations in the calculated cold parameters are expected if beam effects are taken into account [112], the axial field profile can be considered fixed in gyrotron cavities with Q_D much higher than the minimum diffractive quality factor $Q_D^{min} = 4\pi(L/\lambda)^2$ [41, 106].

2.3 Nonlinear Gyrotron Theory

Once the profile of the electric and magnetic microwave fields are known in the gyrotron resonator as derived in Section 2.2.1, the beam-wave efficiency $\eta_\perp$ can be estimated using a classical relativistic approach where the equations of motion of a single electron moving in a combined field formed by the cavity fields and the external static magnetic field are solved. For an electron gyrating in a Larmor orbit of radius r_L, which is centered at the guiding center r_e and angle ϕ_e as shown in Fig. 2-1, the equations of motion are:

$$\frac{d\epsilon}{dt} = -e\mathbf{E}\cdot\mathbf{v} \tag{2.46}$$

$$\frac{d\mathbf{p}}{dt} = -e(\mathbf{E} + \mathbf{v}\times\mathbf{B}) \tag{2.47}$$

where $\epsilon = \gamma m_e c^2$ is the electron energy, and $\mathbf{p} = \gamma m_e \mathbf{v}$ is the electron linear momentum.

The microwave electric field $\mathbf{E}$ of a TE cylindrical cavity mode is given by Eqs. (2.22)-(2.24) in cylindrical coordinates (ρ, ϕ, z) and phasor form. The microwave magnetic field $\mathbf{B_1}$ is related to the electric field E using Faraday's law where $\mathbf{B_1} = \mathbf{k}\times\mathbf{E}/\omega$. The force terms produced by the transverse component $\mathbf{B_{1\perp}} = (k_z/\omega)\hat{z}\times\mathbf{E}_\perp$, including one term $\mathbf{v}_\perp \times \mathbf{B_{1\perp}}$ associated with axial bunching by moving electrons in the z direction, can be neglected since gyrotrons operate near the cutoff of a $\mathrm{TE}_{m,p,q}$ cavity mode where $v_{ph} = \omega/k_z > c$. Therefore even though azimuthal and axial bunching are both present and compete with each other in gyrotrons, the first mechanism dominates in fast-wave interaction ($v_{ph} > c$) [5]. The other microwave magnetic field component scales as $|B_z| = (k_\perp/\omega)|E_\perp|$ and it can be discarded for a weakly relativistic electron beam. After these considerations, the magnetic field is taken to be the static magnetic field $\mathbf{B} = \mathbf{B_0}\hat{z}$ and p_z is constant [106]. Here the axial microwave field profile $f(z)$ is assumed to be fixed despite the presence of an electron beam, which is a good approximation for gyrotron resonators with Q_D much higher than Q_D^{min}.

The electromagnetic fields seen by electrons in a Larmor orbit can be expressed in a coordinate system (r, θ, z) with origin at $(\rho = r_e, \phi = \phi_e)$ by using Graf's theorem [113]. The result is:

$$E_r = jE_1 f(z) e^{j\omega t} \sum_{s=-\infty}^{\infty} \frac{s}{k_\perp r} J_{m\pm s}(k_\perp r_e) J_s(k_\perp r) e^{j(s-m)\phi_e} e^{-js\theta} \tag{2.48}$$

$$E_\theta = E_1 f(z) e^{j\omega t} \sum_{s=-\infty}^{\infty} J_{m\pm s}(k_\perp r_e) J'_s(k_\perp r) e^{j(s-m)\phi_e} e^{-js\theta} \tag{2.49}$$

with $\theta = \omega_c t + \theta_0$ denoting the electron phase where θ_0 corresponds to the initial electron phase. A net beam-wave energy transfer occurs for electrons that remain in phase with the n^{th}-harmonic field component ($s = n$). This requires:

$$\omega = n\omega_c + k_z v_z \tag{2.50}$$

which is the synchronism condition. As gyrotrons operate near cutoff, one has $\omega \approx$

$n\omega_c$. For weakly relativistic beams, the quantity $k_\perp r = k_\perp r_L \approx n\beta_\perp$ is small so that the functions $J_n(k_\perp r)$ and $J_n'(k_\perp r)$ can be approximated as $J_n(k_\perp r) \approx (k_\perp r/2)^n/n!$ and $J_n'(k_\perp r) \approx n(k_\perp r)^{n-1}/(2^n n!)$. From these results, one can obtain an expression in the time domain for the electric field component in synchronism with the electrons:

$$\begin{aligned}\mathbf{E}(\mathbf{r},t) &= E_1'(k_\perp r)^{n-1} f(z)[-\sin(\omega t - n\theta + (n-m)\phi_e)\hat{r} \\ &\quad + \cos(\omega t - n\theta + (n-m)\phi_e)\hat{\theta}] \end{aligned} \tag{2.51}$$

with $E_1' = E_1[n/(2^n n!)]J_{m\pm s}(k_\perp r_e)$. The field $\mathbf{E}(\mathbf{r},t)$ has a rotating multipole configuration and for the second cyclotron harmonic $n = 2$ it takes a quadrupolar form as seen in Fig. 2-2. Each frame in Fig. 2-2 was obtained at a multiple of the microwave period T with $(n-m)\phi_e = -\pi/2$, where the field takes the form $E_x \propto \cos\theta = x$ and $E_y \propto -\sin\theta = -y$ in cartesian components, leading to the quadrupolar solution $xy = \text{cte}$ for the field line equation $dx/dy = E_x/E_y = -x/y$.

Using $dz/dt = v_z$, $\nu \equiv \omega t - n\theta$, and choosing $(n-m)\phi_e = -\pi/2$, the equations of motion (2.46) and (2.47) become:

$$\frac{d\epsilon}{dz} = -e\frac{p_\perp}{p_z}(k_\perp r)^{n-1} E_1' f(z)\sin(\nu) \tag{2.52}$$

$$\begin{aligned}\frac{d\nu}{dz} &= -\frac{ne\gamma m_e}{p_\perp p_z}(k_\perp r)^{n-1} E_1' f(z)\cos(\nu) + \left(1 - \frac{n\omega_{c0}}{\omega}\right)\frac{\omega}{\beta_{z0}c} \\ &\quad + \left(\frac{\gamma}{\gamma_0} - 1\right)\frac{\omega}{\beta_{z0}c} \end{aligned} \tag{2.53}$$

with the subscript 0 denotes quantities at the entrance of the interaction region. After defining the normalized energy parameter u, the normalized length ζ, and the detuning parameter Δ:

$$u \equiv \frac{2}{\beta_{\perp 0}^2}\left(1 - \frac{\gamma}{\gamma_0}\right) \tag{2.54}$$

$$\zeta \equiv \frac{\beta_{\perp 0}^2}{\beta_{z0}}\frac{\omega}{c}\frac{z}{2} \tag{2.55}$$

$$\Delta \equiv \frac{2}{\beta_{\perp 0}^2}\left(1 - \frac{n\omega_{c0}}{\omega}\right) \tag{2.56}$$

and using the approximation:

$$k_\perp r_L = \frac{\omega}{\omega_{c0}}\left(\beta_{\perp 0}^2 - 1 + \frac{\gamma^2}{\gamma_0^2}\right)^{1/2} \approx n\beta_{\perp 0}(1-u)^{1/2}$$

equations (2.52) and (2.53) can be rewritten as:

$$\frac{du}{d\zeta} = 2F(1-u)^{n/2} f(\zeta)\sin(\nu) \tag{2.57}$$

$$\frac{d\nu}{d\zeta} = \Delta - u - nF(1-u)^{n/2-1} f(\zeta)\cos(\nu) \tag{2.58}$$

where F is the normalized field amplitude given by:

$$F \equiv \frac{E_1}{B_0 c}\beta_{\perp 0}^{n-4}\left(\frac{n^{n-1}}{n!2^{n-1}}\right) J_{m\pm n}(k_\perp r_e) \tag{2.59}$$

For a given interaction length $\mu = \zeta(L)$, normalized field F, detuning Δ, and initial conditions $u_0 = 0$, $\nu_0 \in [0, 2\pi)$, the set of equations (2.57) and (2.58) can be solved numerically. The interaction efficiency $\eta_\perp$ is calculated by:

$$\eta_\perp = \frac{1}{2\pi}\int_0^{2\pi} u(\zeta_{out}) d\nu_0 \tag{2.60}$$

At steady state the power transferred from the electron beam (see Eq. (2.1)) is equal to the total losses P_T in the gyrotron cavity from (2.29):

$$\frac{\omega U}{Q} = \frac{\beta_{\perp 0}^2}{2(1-\gamma_0^{-1})}\eta_\perp V_b I_b = \frac{p_{\perp 0}^2}{2\gamma_0 m_e e}\eta_\perp I_b \tag{2.61}$$

After multiplying both sides of Eq. (2.61) by $|F|^2$ and using Eq. (2.30), the energy balance equation can be rewritten as:

$$|F|^2 = \eta_\perp I \tag{2.62}$$

with the normalized current I defined as:

$$I = 2\left(\frac{e}{m_e\varepsilon_0 c^3}\right)\left(\frac{QI_b}{\gamma_0}\right)\left(\frac{n^n}{n!2^n}\right)^2\left(\frac{J^2_{m\pm n}(k_\perp r_e)}{(\nu'^2_{mp}-m^2)J^2_m(\nu'_{mp})}\right)\frac{\beta_{\perp 0}^{2(n-3)}}{\left(\frac{\pi^2}{\lambda}\right)\int_0^L |f(z)|^2 dz} \tag{2.63}$$

The quantity $C_{m,p}$ shown below is a measure of the beam-wave coupling strength for a given $\mathrm{TE}_{m,p,q}$ mode and electron beam of radius r_e, and hence is referred to as the beam-wave coupling coefficient. The order of the Bessel function $m-n$ and $m+n$ correspond to waves azimuthally co-rotating and counter-rotating with respect to the electron gyration, respectively.

$$C_{m,p} = \frac{J^2_{m\pm n}(k_\perp r_e)}{(\nu'^2_{mp}-m^2)J^2_m(\nu'_{mp})} \tag{2.64}$$

Based on the formalism described in this section, an interaction efficiency $\eta_\perp$ map for the second cyclotron harmonic $n = 2$ can be generated and it is shown in Fig. 2-4. Each point (μ, I) of the map is optimized with respect to the detuning parameter Δ and a Gaussian axial field profile $f(\zeta) = e^{-(2\zeta/\mu)^2}$ or $f(z) = e^{-(k_z z)^2}$ integrated over $-\sqrt{3}/2 < \zeta < \sqrt{3}/2$ was assumed in the computation. In theory, orbital efficiencies $\eta_\perp$ on the order of 70% can be reached for second-harmonic modes.

2.4 Linear Gyrotron Theory and Threshold for Oscillations

Besides the interaction efficiency $\eta_\perp$, another parameter of interest for gyrotron oscillators is the start oscillation current I_{st}. This parameter is defined as the minimum current on which the power extracted from the electron beam equalizes or overcomes the cavity losses so that the electromagnetic fields are allowed to reach steady state operation or to grow. In this regime, the interaction efficiency is described by linear theory as [38]:

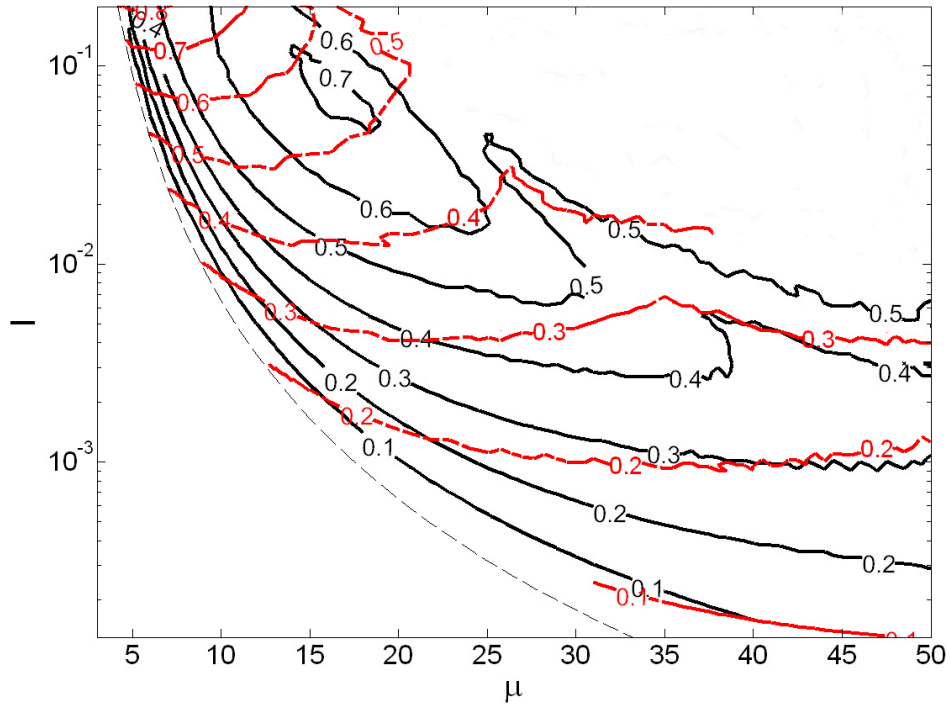

Figure 2-4: Contour plot of the orbital efficiency $\eta_{\perp}$ (solid black lines) as a function of the normalized length μ and the normalized current I for second-cyclotron harmonic interaction ($n = 2$) and Gaussian axial field profile $f(\zeta) = e^{-(2\zeta/\mu)^2}$. The red lines represent the optimum detuning Δ while the dashed black line indicates the normalized minimum start current I_{MIN}.

$$\eta_{\perp\_lin} = \frac{|F|^2}{I_{st\_norm}} \tag{2.65}$$

where the normalized start current I_{st_norm} is given by:

$$I_{st\_norm} = -\frac{1}{\left(n + \frac{\partial}{\partial\Delta}\right)\left|\int_0^{\mu} f(\zeta)\exp\left(j\int_0^{\zeta}\Delta d\zeta'\right)d\zeta\right|^2} \tag{2.66}$$

Substituting Eq. (2.66) into Eq. (2.63), one obtains the start current expression I_{st} in amperes:

$$I_{st} = -\frac{1}{2}\left(\frac{m_e \varepsilon_0 c^3}{e}\right)\left(\frac{\gamma_0}{Q}\right)\left(\frac{n!2^n}{n^n}\right)^2 \frac{\beta_{\perp 0}^{2(3-n)}}{C_{m,p}} \frac{\left(\frac{\pi^2}{\lambda}\right)\int_0^L |f(z)|^2 dz}{\left(n+\frac{\partial}{\partial\Delta}\right)\left|\int_0^\mu f(\zeta)\exp\left(j\int_0^\zeta \Delta d\zeta'\right)d\zeta\right|^2} \tag{2.67}$$

For the special case where the axial field profile is approximated by a Gaussian profile $f(\zeta) = e^{-(2\zeta/\mu)^2}$, the normalized start current I_{st_norm} takes the form:

$$I_{st\_norm} = \frac{4}{\pi\mu^2}\frac{e^{(\Delta\mu)^2/8}}{\left(\frac{\Delta\mu^2}{4}-n\right)} \tag{2.68}$$

which can be minimized with respect to Δ by taking $\Delta_{MIN} = (2/\mu)[n/\mu + (n^2/\mu^2 + 1)^{1/2}]$, yielding $I_{MIN} = I_{st\_norm}(\Delta_{MIN})$. For $n = 2$, the parameter I_{MIN} is plotted as a a function of μ in Fig. 2-4.

An extension of Eq. (2.67) that takes into account effects of tapering of the external static magnetic field, finite beam thickness, electron velocity spread, and tapering of the cavity wall radius, is provided in Ref [114]. Computer codes based on (2.67) and its extended formulation in [114] were written and they are utilized in this work to estimate the threshold current for gyrotron oscillations.

2.5 Self-Consistent Gyrotron Code

The design of gyrotrons under more realistic conditions than that provided in Section 2.3 can be obtained by self-consistent simulations where the electrons are sources for the electromagnetic fields and the fields are part of the forces driving the electrons. In this work the self-consistent code Maryland Gyrotron (MAGY) [115] is utilized for gyrotron modeling and design.

Instead of the full solution of Maxwell's equations, MAGY represents the electromagnetic fields as a superposition of TE and TM eigenmodes of a cylindrical waveguide where the interaction takes place and solves a reduced set of coupled partial

differential equations obtained from Maxwell's equations. Coupling between modes occurs due to the finite conductivity σ of the metallic wall of the interaction structure, the electron beam, and the variation of the structure wall radius as a function of the longitudinal position. The surface impedance Z_s utilized in the code is in Gaussian units and it can be obtained from the surface impedance in SI units as:

$$Z_{s\_CGS} = \frac{Z_{s\_SI}}{377} = \frac{1}{377}\sqrt{\frac{\omega\mu_0}{2\sigma}} \tag{2.69}$$

As the complex amplitude of each mode evolves slowly compared to the microwave period, the electromagnetic fields are updated at a fraction of the cavity fill time Q/ω and not at a fraction of the much shorter microwave period $2\pi/\omega$. The fields are only determined at the location of the electron beam for faster processing. In addition, MAGY assumes that the electrons traverse the cavity in a time shorter than the cavity fill time and that the particles are confined by a strong static magnetic field, essentially following the magnetic field lines.

Chapter 3

Design of a Tunable 330-GHz Second-Harmonic Gyrotron

Once the theoretical basis of gyrotrons and the main tools for gyrotron design have been reviewed and described in Chapter 2, the current chapter details the design of a continuous-wave frequency-tunable 330-GHz gyrotron oscillator operating at the second harmonic of the electron cyclotron frequency. The target application of this gyrotron is sensitivity-enhanced nuclear magnetic resonance via dynamic nuclear polarization (DNP/NMR). After reviewing the gyrotron requirements for this particular application in Section 3.1, Section 3.2 outlines the advantages and challenges of second-harmonic operation. Section 3.3 discusses the tradeoffs of the gyrotron cavity design in order to achieve the desired requirements. Evaluation of the electromagnetic properties of the fabricated gyrotron cavity with the electron beam absent, here referred as a cold test, is also presented in this section. Section 3.4 details the design of a quasi-optical internal mode converter utilized to transform the generated cylindrical waveguide mode to a Gaussian-like beam for low-loss transmission to the NMR sample. The design and description of auxiliary components necessary for the gyrotron operation such as a superconducting magnet, an electron gun, a high voltage power supply, a gyrotron collector, and a transparent window are the subject of Section 3.5. A schematic of the designed 330-GHz gyrotron is shown in Fig. 3-1.

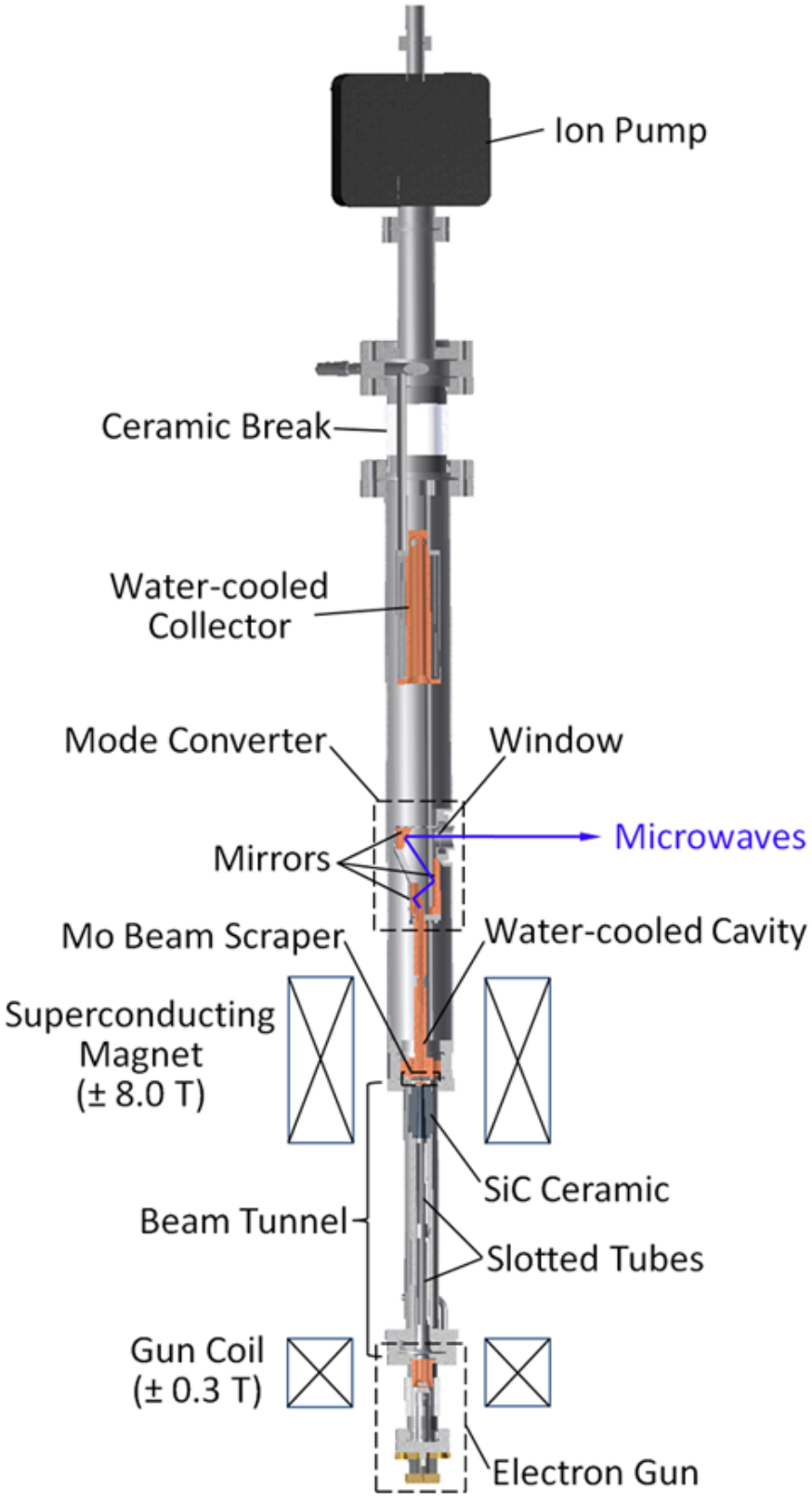

Figure 3-1: Schematic of the 330-GHz gyrotron.

3.1 Gyrotron Requirements for DNP

As already introduced in Section 1.3, dynamic nuclear polarization is a technique utilized to enhance the signal-to-noise (SNR) ratio in NMR experiments by transferring the large polarization of exogenous or endogenous electron spins to the nuclear spins of a sample of interest. This is performed by irradiating the sample with electromagnetic waves at a frequency close to the electron Larmor frequency $f_e \approx 28.024 B_{NMR}$ GHz/T, which is also close to the electron cyclotron frequency. In order to implement DNP in a 500 MHz NMR spectrometer with a fixed $B_{NMR} = 11.74$ T, one needs a gyrotron oscillating at a frequency near 330 GHz. For an efficient transfer of spin polarization [66, 67], the 330 GHz gyrotron should deliver several watts to several tens of watts of output power in CW regime. Power and frequency fluctuations in the gyrotron should be kept on the order of 1% and 1 MHz, respectively, so that long-term signal averaging can be carried out in DNP experiments [68].

Considering that the DNP enhancement depends on the electron paramagnetic resonance (EPR) to drive the polarization of nuclear spins, the ability to sweep the gyrotron frequency across the EPR bandwidth is paramount so that the DNP signal can be optimized. A continuously tunable gyrotron not only simplifies the DNP operation since the NMR magnet field does not have to be swept but also permits the implementation of DNP in NMR spectrometers with fixed magnetic field, without sweep coils installed. The 500 MHz NMR spectrometer that will be part of the DNP system for which the gyrotron described in this thesis was developed does not have sweep coils. The 330 gyrotron should have a continuous tuning range of 1.5 GHz, which corresponds to the EPR spectrum of endogenous electron spins in nitroxide

Table 3.1: Specifications of a continuously tunable 330 GHz gyrotron for 500 MHz DNP/NMR experiments

Frequency range	329.4 ± 0.75 GHz
Output power	> 5 W
Operation	Continuous wave
Frequency stability	≈ 1 MHz
Power stability	$\approx 1\%$

radical polarizing agents. This tuning range should be centered around 329.4 GHz, which is the microwave frequency for the optimum DNP/NMR enhancement. A summary of the gyrotron specifications for a 500 MHz DNP/NMR system is given in Table 3.1.

3.2 Second-Harmonic Considerations

According to the synchronism condition in Eq. (1.1) and the fact that gyrotrons operate near the cutoff of a waveguide mode, gyrotrons radiate at a frequency near a harmonic n of the electron cyclotron frequency $f \approx nf_c$. This requires the value of the magnetic field in the interaction region to be $B_0 = 0.036\gamma f/n$ T/GHz.

The main advantage of a harmonic gyrotron is the reduced magnetic field required for oscillation at a given frequency f, a field reduced by a factor $1/n$ when compared to fundamental-harmonic operation. For example, while a weakly relativistic 330 GHz gyrotron would need an expensive Nb_3Sn superconducting magnet to provide $B_0 \approx 12$ T, a second-harmonic version could utilize a cheaper NbTi superconducting magnet for a $B_0 \approx 6$ T. This fact motivated the operation of the 330 GHz gyrotron described in this thesis at the second cyclotron harmonic. From another viewpoint, harmonic gyrotrons can radiate at frequencies n times higher for a given magnetic field, extending the usage of gyrotrons and related applications such as high-field DNP/NMR to higher frequencies. For instance, a weakly relativistic gyrotron utilizing a state-of-the-art 23.5-T Nb_3Sn could generate frequencies up to 1.25 THz in CW second-harmonic operation.

Despite these advantages, operation at a cyclotron harmonic brings forth extra challenges due to a reduced orbital efficiency $\eta_\perp$, higher start oscillation current I_{st}, and additional mode competition with neighboring fundamental modes.

The reduced efficiency and higher start current at harmonic operation is primarily a consequence of the lower gain $\beta_{\perp 0}^{2n}$ and in a lesser extent due to the lower coupling coefficient. The gain term is related to the normalized field amplitude F in synchronism with electrons as seen in Eq. (2.59). Following the normalized current I in

Eq. (2.63), which is related to $\eta_\perp$ as seen in Fig. 2-4 and to the start current I_{st} in Eq. (2.67), the ratio I_2/I_1 between second-harmonic ($f_c' = f/2$) and fundamental-harmonic operation ($f_c = f$) at a given frequency f, $\mathrm{TE}_{m,p}$ mode, cavity geometry, and beam power is:

$$\frac{I_2}{I_1} = \beta_{\perp 0}^2 \left(\frac{J_{m\pm 2}(k_\perp r_e')}{J_{m\pm 1}(k_\perp r_e)} \right)^2 \tag{3.1}$$

The first term is the gain $\beta_{\perp 0}^2$ which is equal to 1/30 for a beam voltage $V_b =$ 10 kV and $\alpha = 2$. The second term comes from the coupling coefficient $C_{m,p}$. Choosing close values of beam radius r_e and r_e' that maximizes the coupling at fundamental and second-harmonic operation for a given azimuthal rotation, one has $0.47 < J_{m\pm 2}^2(k_\perp r_e')/J_{m\pm 1}^2(k_\perp r_e) < 2.1$. For example, for a co-rotating mode at 330 GHz with azimuthal index $m = 0$, the second peak for fundamental interaction $J_{m-1}^2(k_\perp r_e) = 0.35$ is located at $r_e = 0.77$ mm, while the second peak for second-harmonic interaction $J_{m-2}^2(k_\perp r_e') = 0.31$ is located at $r_e' = 0.97$ mm. This results to $J_{-2}^2(k_\perp r_e')/J_1^2(k_\perp r_e) = 1.13$. Therefore for a given mode $\mathrm{TE}_{m,p}$ operating at the second cyclotron harmonic, the lower ratio I_2/I_1 yields a lower orbital efficiency $\eta_\perp$ and a start current I_{st} about one order of magnitude higher when compared to fundamental-harmonic operation in the same mode and frequency.

For a comparison between an operating second-harmonic mode and a neighbor fundamental mode, the ratio I_2/I_1 for a given beam radius r_e, beam power, and cavity geometry is:

$$\frac{I_2}{I_1} = \frac{\beta_{\perp 0}^2}{2} \frac{(C_{m,p})_{2\omega_c}}{(C_{m,p})_{\omega_c}} \frac{(Q)_{2\omega_c}}{(Q)_{\omega_c}} \tag{3.2}$$

where the gain term $\beta_{\perp 0}^2$ gives the fundamental modes an edge in terms of better efficiency and lower start current for comparable coupling coefficients.

For a gyrotron resonator of radius r_{cav}, the possible frequencies of $\mathrm{TE}_{m,p}$ modes that can be excited in the device is given by $f = (c\nu_{mp}')/(2\pi r_{cav})$. Hence the spacing

between the zeros ν'_{mp} of the derivative of the Bessel function $J'_m(x)$ results in a discrete spectrum with gaps between consecutive $\mathrm{TE}_{m,p}$ modes. However as gyrotrons radiate at a frequency near a harmonic of the cyclotron frequency, the mode spectrum as a function of magnetic field becomes denser since a second-harmonic mode with ν'_{mp2} and a fundamental mode with $\nu'_{mp1} \approx \nu'_{mp2}/2$ may be excited at a similar B_0. As a consequence, it is important to choose an operating second-harmonic mode that is isolated from neighboring second-harmonic and fundamental modes. Fundamental modes pose a higher threat since they can be easily excited due to their lower start current as discussed.

3.3 Design of a Tunable Cavity

In order to minimize the issues associated with second-harmonic operation, the mode $\mathrm{TE}_{-4,3}$ was chosen as the operating mode due to its high coupling coefficient among second-harmonic modes to an electron beam of radius $r_e = 1.08$ mm. The mode search also excluded cases where a high coupling occurred for $r_e \leqslant 0.9$ mm due to constraints set by the electron gun and beam compression, cases where $r_e/r_{cav} > 0.75$ since the electron beam would be too close to the wall, and modes that required $r_{cav} < 1.5$ mm due to possible beam interception in the downtapered section of the gyrotron cavity. Previous observation of this mode in a 460-GHz gyrotron as described in Chapter 5 also motivated its choice. The coupling coefficient $C_{m,p}$ for the operating mode and nearby fundamental and second-harmonic modes are shown in Fig. 3-2.

The mode $\mathrm{TE}_{-4,3}$ is supported by a 35-mm long cylindrical cavity with radius $r_{cav} = 1.834$ mm. A long cavity ($L \sim 38\lambda$ at 330 GHz where λ is the free-space wavelength) was preferred in order to lower the start oscillation current (*cf.* Eq. (2.63)) and enable excitation of high-order axial modes for frequency tunability via cyclotron frequency. Low start current is particularly important for gyrotrons operating with reduced beam power and beam current due to limitations set by the electron gun and/or the power supply. As detailed in Section 3.5.3, the beam current for CW operation in the 330 GHz gyrotron is restricted to 200 mA by the power supply.

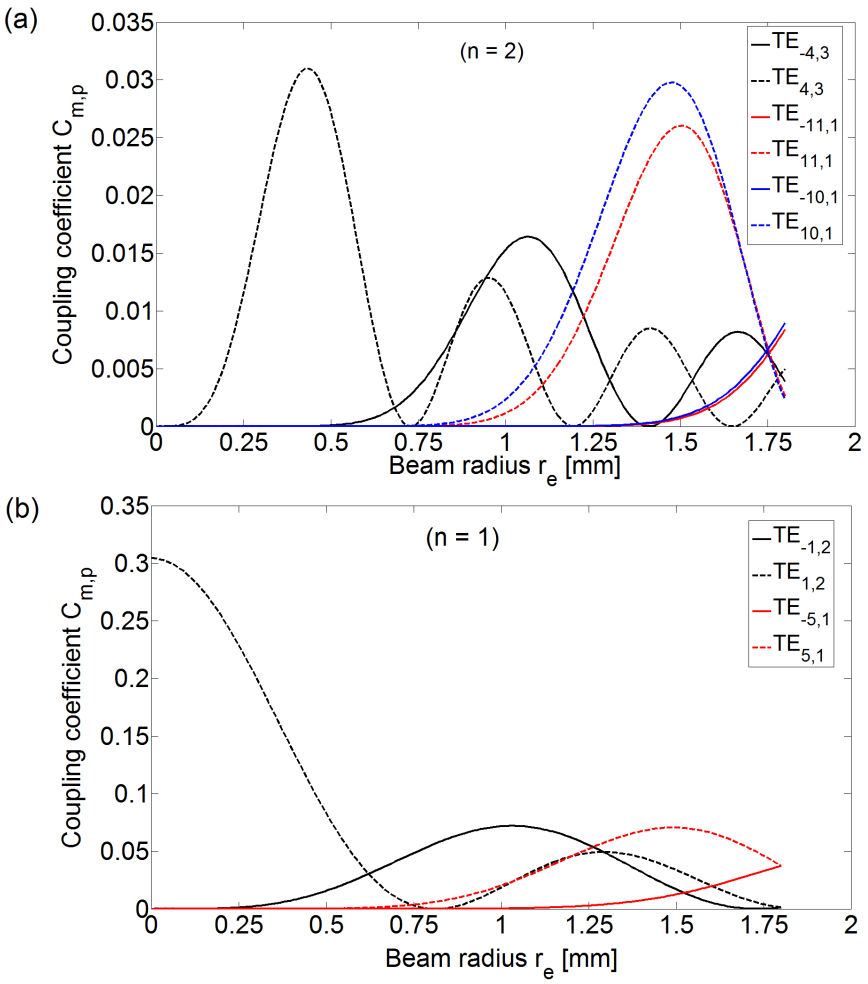

Figure 3-2: (a) Coupling coefficient $C_{m,p}$ of the operating mode $\mathrm{TE}_{-4,3}$ along with nearby second-harmonic modes and (b) nearby fundamental-harmonic modes.

The interaction circuit geometry comprising a downtapered section, a cavity straight section, and an uptapered section is shown in Fig. 3-3. The axial electric field profile of the first axial mode $\mathrm{TE}_{-4,3,1}$ was calculated using the cold-cavity code [111] detailed in Section 2.2.3 and it is represented in Fig. 3-3 by a red line. The transverse electric field profile of the operating mode and the location of the electron beam are depicted as an inset in Fig. 3-3.

At a submillimeter wavelength, a considerable part of the power extracted from the beam is dissipated in the cavity walls as ohmic loss. The ohmic Q, Q_O, for the different axial modes $\mathrm{TE}_{-4,3,q}$ was computed to be $Q_O = 10149$ using Eq. (2.35) and assuming an electrical conductivity σ half that of ideal copper (5.8×10^7 S/m).

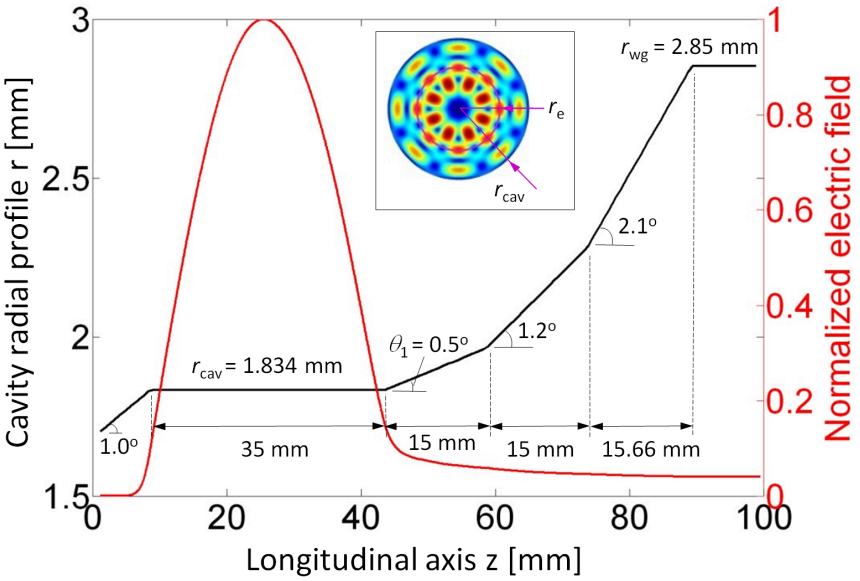

Figure 3-3: 330-GHz gyrotron circuit profile (black line) featuring a downtapered section, cavity (straight section), and an uptapered section. The red line corresponds to the normalized axial electric field profile of the operating mode $TE_{-4,3,1}$. The inset shows the transverse electric field profile of the mode $TE_{-4,3}$ and the electron beam radius r_e.

Another factor for a reduced power extraction η_{RF} from the gyrotron resonator is the lower diffraction loss as a consequence of using a long cavity to decrease the start oscillation current. The diffractive Q, Q_D, has a $(L/\lambda)^2$ dependence according to Eq. (2.37) and it was calculated using the cold-cavity code. For $TE_{-4,3,q}$ modes, one has $Q_{D,q} = 81530/q^2$, following the q^{-2} dependence outlined in Section 2.2.2. In order to avoid Q_D to be even higher and η_{RF} lower, a shallow uptaper angle $\theta_1 = 0.5°$ was selected for reduced wave reflection R_{up} at the uptapered end. The higher the angle θ_1, the higher the reflection R_{up}. For example, for the same cavity length $L = 35$ mm and mode $TE_{-4,3,1}$ at 330 GHz, an increase in θ_1 from 0.2° to 0.5° changes Q_D from 63350 to 81530 and η_{RF} from 13.8% to 11.4%. In addition to lower reflection, the uptapered section was also designed for reduced mode conversion, which was found to be less than 0.3% according to calculations using the scattering matrix code Cascade [116].

The start oscillation current I_{st} of the operating mode $TE_{-4,3,1}$ was computed using the linear theory described in Section 2.4 and the result is shown in Fig. 3-

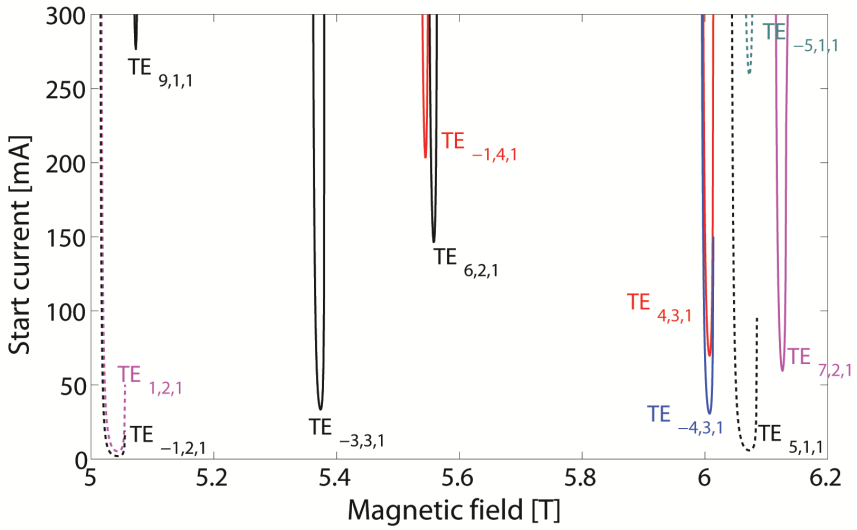

Figure 3-4: Start oscillation current of cavity $TE_{m,p,1}$ modes adjacent to the operating mode $TE_{-4,3,1}$. Dashed lines represent fundamental-harmonic modes while solid lines refer to second-harmonic modes. For each $TE_{m,p,q}$ mode, only the lowest axial mode ($q = 1$) is shown (Beam parameters: $V_b = 10.1$ kV, $r_e = 1.08$ mm, $\alpha = 1.8$, and no velocity spread).

4. The minimum I_{st} was computed to be 31 mA for beam parameters $V_b = 10.1$ kV, $\alpha = 1.8$, and no velocity spread. The axial field profile $f(z)$ was obtained from the cold-cavity code. Utilizing similar procedure, the start currents for neighboring modes $TE_{m,p,1}$ were also calculated and they are displayed in Fig. 3-4 as well. From a cold cavity perspective, the counter-rotating mode $TE_{-4,3,1}$ should prevail over the co-rotating mode $TE_{4,3,1}$ due to the higher coupling and lower start current [117].

3.3.1 Frequency Tunability

As mentioned previously, the gyrotron cavity was made long in order to enable excitation of high-order axial modes for frequency tunability via cyclotron frequency. A long cavity not only lowers the start current of each axial mode but also make their eigenfrequencies to be closer to each other for continuous tunability. Even though the best magnetic tuning result for a second-harmonic submillimeter-wave gyrotron was limited to 50 MHz [68, 90] at the beginning of this project, experiments performed at MIT at 460 GHz [98, 101] and 332 GHz [98] successfully demonstrated continuous frequency tunability up to 1 GHz as a function of magnetic field and beam voltage

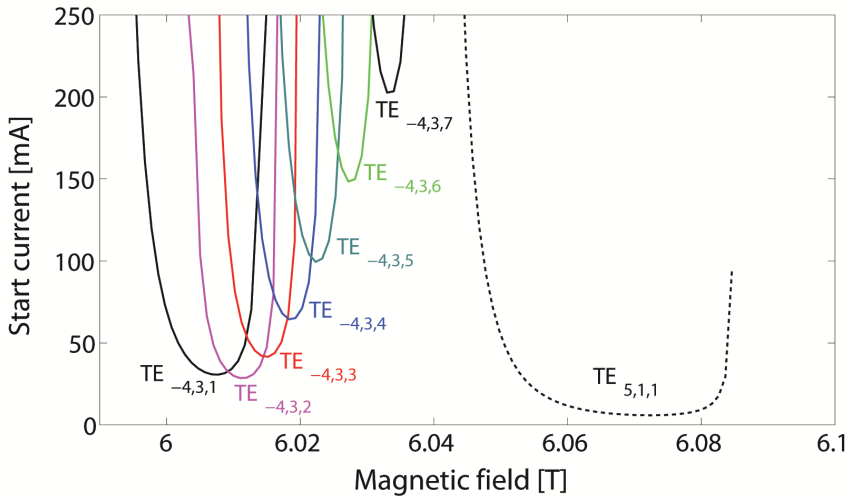

Figure 3-5: Start oscillation current of high-order axial modes $TE_{-4,3,q}$, $q = 1$ to $q = 7$, and neighboring fundamental mode $TE_{5,1,1}$ (Beam parameters: $V_b = 10.1$ kV, $r_e = 1.08$ mm, $\alpha = 1.8$, and no velocity spread).

as presented in Chapter 5. For this reason, tunability via cyclotron frequency was selected instead of a more complex approach involving, for example, a mechanically tunable structure.

One method to estimate the frequency tunability of the current design is by computing the start oscillation of each axial mode $TE_{-4,3,q}$. The axial field profile $f(z)$ was assumed to be the one obtained from the cold-cavity code. The result of the start current calculation is shown in Fig. 3-5 for beam parameters $V_b = 10.1$ kV, $\alpha = 1.8$, and no velocity spread. The fundamental mode $TE_{5,1,1}$ is also displayed as a reference. If one considers the current limit of 200 mA in the CW power supply

Table 3.2: Cold resonant frequencies and diffractive Q_D of different axial modes $TE_{-4,3,q}$ for the gyrotron cavity geometry displayed in Fig. 3-3

Axial mode number q	Cold resonant frequency [GHz]	Q_D
1	329.96	81530
2	330.03	20379
3	330.15	9053
4	330.32	5081
5	330.54	3233
6	330.81	2234
7	331.13	1668

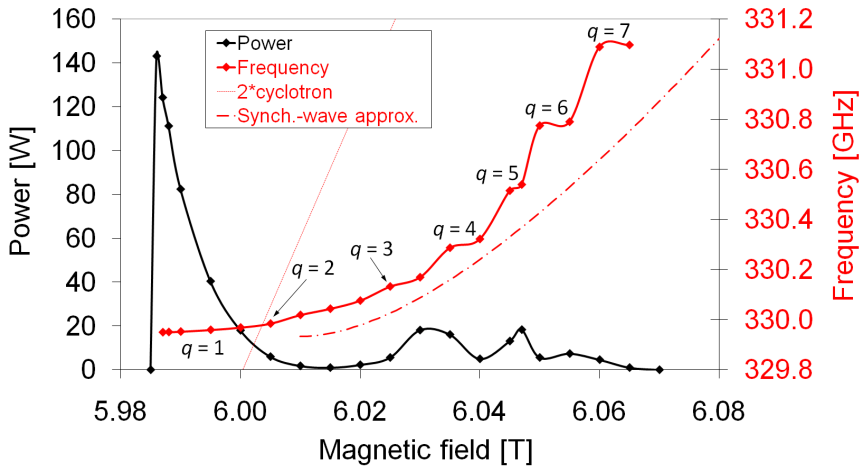

Figure 3-6: Self-consistent simulation (MAGY code) of output power and frequency tuning as a function of magnetic field for the operating $TE_{-4,3}$ mode (Beam parameters: $V_b = 10.1$ kV, $I_b = 190$ mA, $r_e = 1.08$ mm, $\alpha = 1.8$, $\Delta v_\perp / v_\perp = 5\%$). The red dash-dotted line represents the intersection between the operating mode waveguide dispersion and the synchronism condition.

utilized in this experiment (*cf.* Section 3.5.3), it may possible to excite axial modes ranging from $q = 1$ to $q = 7$ with frequencies between 329.96 GHz to 331.13 GHz as summarized in Table 3.2.

Another approach to evaluate the frequency tunability is by using the self-consistent code MAGY [115] reviewed in Section 2.5. The simulation result as a function of magnetic field is shown in Fig. 3-6 where seven axial modes could be excited with frequencies similar to the ones predicted by the cold-cavity code. The highest power is obtained in the forward interaction with the first axial mode $q = 1$ and then the interaction switches to the backward-wave component of high-order axial modes $q \geqslant 2$. As seen in Fig. 1-7, a forward interaction is characterized by the microwave frequency being greater than the cyclotron harmonic while in a backward interaction one has the opposite case.

The theoretical tuning range provided by high-order axial modes in backward interaction can be compared with the estimated operating frequency obtained from the intersection between the synchronism condition (*cf.* Eq. (1.1)) and the operating mode waveguide dispersion (*cf.* Eq. (1.2)). Equating Eq. (1.1) and Eq. (1.2), the resultant frequency ω for backward interaction is given by:

Table 3.3: Design parameters of tunable 330-GHz gyrotron

Mode	$TE_{-4,3,q}$
Frequency	330 GHz
Harmonic n	2
Voltage V_b	10.1 kV
Current I_b	190 mA
Tuning range	> 1 GHz
Power	> 1 W (CW)

$$\omega = \frac{n\omega_c - \beta_z\sqrt{(n\omega_c)^2 - (1-\beta_z^2)(ck_\perp)^2}}{(1-\beta_z^2)} \tag{3.3}$$

The result of this approximation is plotted as a red dash-dotted line in Fig. 3-6 and it is comparable to the frequency curve obtained using the self-consistent code MAGY. Besides the described tuning via cyclotron frequency, extra frequency tunability can be obtained by thermally expanding the gyrotron cavity if one changes the water temperature T_{cav} in the cavity cooling channel. Considering the operating frequency $f = 330$ GHz and the linear thermal expansion coefficient for copper $\alpha_{Cu} = 17 \times 10^{-6}/℃$, the tuning rate $|\Delta f/\Delta T_{cav}| = f\alpha_{Cu}$ is expected to be 5.6 MHz/℃ in an unconstrained gyrotron cavity. A summary of the design parameters is given in Table 3.3.

3.3.2 Cavity Cold Test

Once the cavity design was completed, the gyrotron cavity was fabricated by electroforming where oxygen-free copper was deposited on a stainless steel mandrel precisely machined to a 2.5 μm tolerance in cavity diameter and with a surface finishing better than 0.2 μm. The cavity was cold tested using a vector network analyzer (VNA) Agilent E8363B with a 90-140-GHz frequency extension and a Vlasov antenna connected to the cavity to couple microwaves into the structure as seen in Fig. 3-7.

As explained in Section 3.4, the modes in a cylindrical waveguide of radius r_{wg} can be represented as a superposition of rays propagating tangentially to a caustic radius

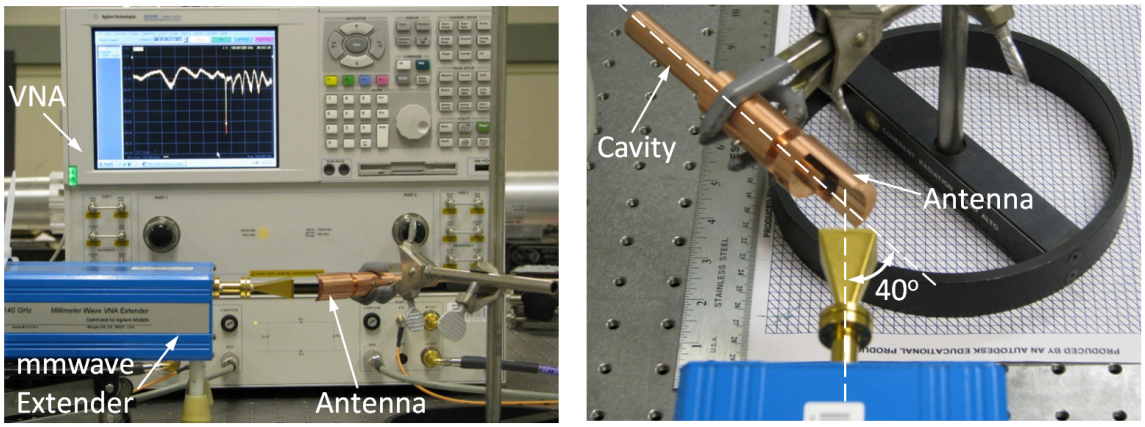

Figure 3-7: Gyrotron cavity cold test setup depicting a vector network analyzer (VNA), a 90-140-GHz millimeter-wave VNA extender, a Vlasov antenna, and the fabricated gyrotron cavity. The angle $\theta_B = 40°$ corresponds to the Brillouin angle.

$r_{caustic} = m/k_\perp = r_{wg}(m/\nu'_{mp})$ and at a Brillouin angle $\theta_B = \arcsin(k_\perp/k)$, which can be approximated as $\theta_B = \arcsin(r_{cav}/r_{wg})$ for gyrotron operation near cutoff and with negligible mode conversion in the uptapered section. For cylindrical modes with no or small caustic radius, the transformation of cylindrical modes to linearly polarized modes can be performed by using a Vlasov antenna as displayed in Fig. 3-8. The variable f_p denotes the focal length of the parabolic mirror and $L_{STEP-CUT} = 2r_{wg}\cot\theta_B$ is the step-cut length to couple electromagnetic waves into/out of the waveguide and gyrotron cavity. The numerical values of the parameters of the Vlasov antenna are given in Table 3.4.

The reflection measurements using the VNA are shown as a black line in Fig. 3-9, where the cavity modes $TE_{0,1}$ ($r_{caustic}/r_{wg} = 0$) and $TE_{1,2}$ ($r_{caustic}/r_{wg} = 0.188$) were observed. In order to ensure that the modes are being excited in the cavity straight section, a hollow metallic plunger was inserted half way trough the straight section as indicated in Fig. 3-10 . The reflection measurements taken with the plunger inserted

Table 3.4: Vlasov antenna parameters for cavity cold test

Cavity radius r_{cav}	1.834 mm
Waveguide radius r_{wg}	2.85 mm
Brillouin angle θ_B	40°
Step-cut length $L_{STEP-CUT}$	6.8 mm
Focal length f_p	5.70 mm

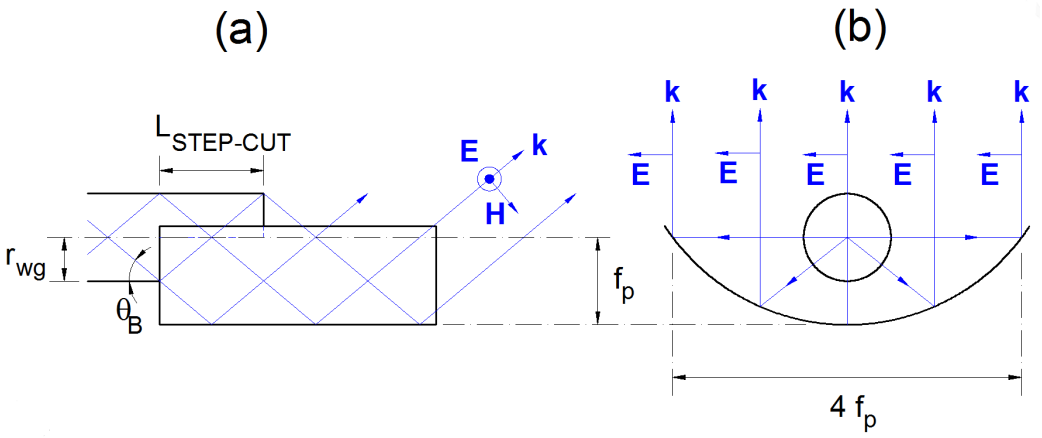

Figure 3-8: Schematic of a Vlasov antenna for cold test of the gyrotron cavity: (a) side view and (b) front view.

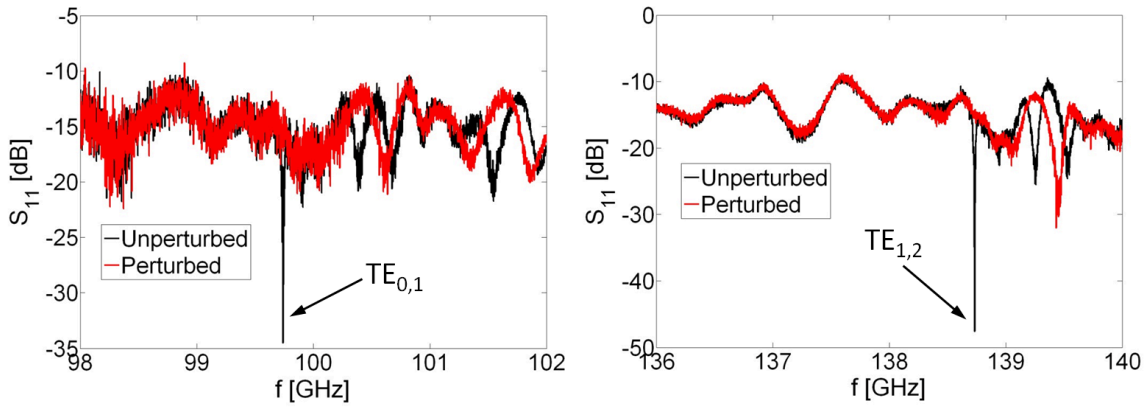

Figure 3-9: Reflection measurements (S_{11}) showing coupling of the modes $TE_{0,1}$ and $TE_{1,2}$ in the gyrotron cavity straight section.

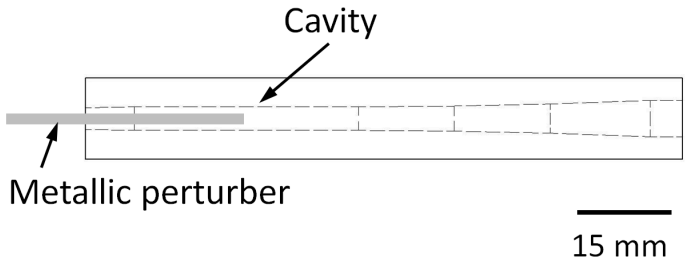

Figure 3-10: Schematic showing the position of a metallic perturber inside the gyrotron cavity.

are shown in Fig. 3-9 as red lines. If one compares the unperturbed (black line) and perturbed (red line) measurement for a given mode, one can verify that for frequencies below the observed resonance, the two curves are identical. This indicates that the observed resonance corresponds to the cutoff frequency of that particular mode so that it cannot propagate in the cavity straight section at frequencies below cutoff. For frequencies above the measured cutoff, the mode can propagate in the straight section and the presence of the plunger disturbs the reflection measurement as verified by the differences between the unperturbed and perturbed lines. In addition, the observed resonance in the unperturbed case is no longer observed with the plunger inserted.

Once the measured resonances in air were corrected for a vacuum medium [118], yielding 99.77 ± 0.01 GHz for the $TE_{0,1}$ mode and 138.78 ± 0.01 GHz for the $TE_{1,2}$ mode, the cold-cavity code was utilized to determine the cavity radius that would match these values. Based on that, the cavity radius was estimated to be within the fabrication tolerance of the design value $r_{cav} = 1.834$ mm with a cold resonant frequency of 329.99 ± 0.02 GHz for the $TE_{4,3}$ gyrotron operating mode.

3.4 Mode Converter Design

Considering the integral form of the Bessel functions $J_m(x)$ and $J'_m(x)$ [119],

$$\frac{m}{x}J_m(x) = \frac{1}{2\pi}\int_0^{2\pi}\cos\theta e^{j(x\sin\theta - m\theta)}d\theta \tag{3.4}$$

$$J'_m(x) = -\frac{j}{\pi}\int_0^{2\pi}\sin\theta e^{j(x\sin\theta - m\theta)}d\theta \tag{3.5}$$

the electric fields for a TE mode in a cylindrical waveguide from Eqs. (2.22)-(2.24) can be represented as a superposition of plane waves as:

$$E_\rho = j\frac{E_1}{2\pi}\int_0^{2\pi}\cos\theta e^{j(\omega t - k_z z + k_\perp \rho\sin\theta + m(\phi-\theta))}d\theta \tag{3.6}$$

$$E_\phi = -j\frac{E_1}{\pi}\int_0^{2\pi}\sin\theta e^{j(\omega t - k_z z + k_\perp \rho\sin\theta + m(\phi-\theta))}d\theta \tag{3.7}$$

$$E_z = 0 \tag{3.8}$$

At very high frequencies in the geometrical optics limit, the solution of Maxwell's equation have the form $\mathbf{E}(\mathbf{r},t) = \mathrm{Re}\{\mathbf{E}e^{j(kS(\mathbf{r})+\omega t)}\}$, where the phase function $S(\mathbf{r})$ is called the eikonal [120]. For the fields in a cylindrical waveguide, the eikonal S is given by:

$$S(\rho,\phi,z) = \frac{1}{k}\left(-k_z z + k_\perp \rho \sin\theta + m(\phi-\theta)\right) \tag{3.9}$$

Following the eikonal equation $|\nabla S(\mathbf{r})|^2 = 1$, where $\nabla S(\mathbf{r})$ gives the direction of the rays, one has:

$$\begin{aligned} |\nabla S|^2 &= \left(\frac{\partial S}{\partial \rho}\right)^2 + \frac{1}{\rho^2}\left(\frac{\partial S}{\partial \phi}\right)^2 + \left(\frac{\partial S}{\partial z}\right)^2 = 1 \\ &= \frac{1}{k^2}\left(k_\perp^2 \sin^2\theta + \frac{m^2}{\rho^2} + k_z^2\right) = 1 \end{aligned} \tag{3.10}$$

Using the dispersion relation $k^2 = k_\perp^2 + k_z^2$ and $k_\perp = \nu'_{mp}/r_{wg}$ for a waveguide of radius r_{wg}, Eq. (3.10) can be solved for θ, which gives:

$$\theta(\rho) = \arccos\left(\frac{m}{\rho}\frac{r_{wg}}{\nu'_{mp}}\right) \tag{3.11}$$

At $\rho = r_{wg}$, one obtains the azimuthal bounce angle ψ of the rays at the waveguide wall:

$$\psi = \arccos\left(\frac{m}{\nu'_{mp}}\right) \tag{3.12}$$

From Eq. (3.11), the eikonal in Eq. (3.9) can be simplified as:

$$S(\rho,\phi,z) = \frac{1}{k}\left[-k_z z + k_\perp \rho\sqrt{1 - r_{caustic}^2} + m\left(\phi - \arccos\left(\frac{r_{caustic}}{\rho}\right)\right)\right] \tag{3.13}$$

where the quantity $r_{caustic}$ is the caustic radius:

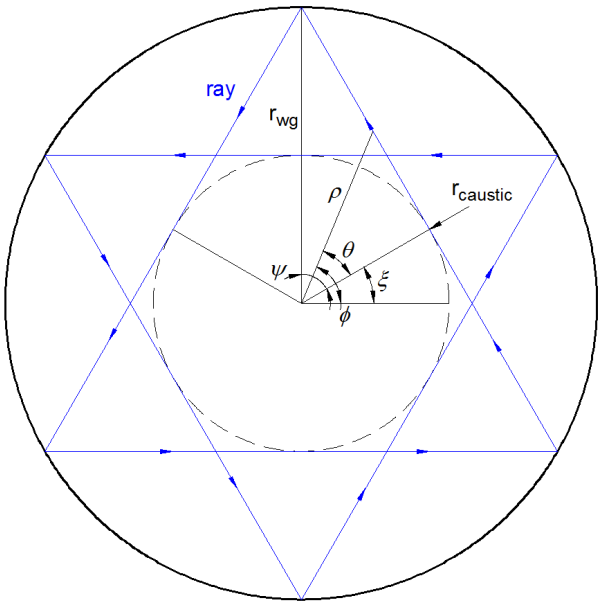

Figure 3-11: Geometrical optics view of a cylindrical waveguide mode as a set of rays traveling tangent to a caustic radius $r_{caustic}$ with an azimuthal bounce angle ψ and a helical pitch angle θ_B.

$$r_{caustic} = \frac{m}{k_\perp} = r_{wg}\frac{m}{\nu'_{mp}} \tag{3.14}$$

It is interesting to note that in this representation of the cylindrical waveguide mode where the fields are proportional to $e^{jkS(\mathbf{r})}$, the fields are exponentially decaying for $\rho < r_{caustic}$. As illustrated in Fig. 3-11, in the geometrical optics limit the waveguide mode can be represented as a set of rays traveling tangent to a caustic surface of radius $r_{caustic}$ with an azimuthal bounce angle ψ and a helical pitch angle $\theta_B = \arcsin(k_\perp/k)$ also known as the Brillouin angle. The equation of a ray is given by [121]:

$$\xi = \phi - \arccos\left(\frac{r_{caustic}}{\rho}\right) = \text{constant} \tag{3.15}$$

After receiving part of the transverse electron energy, the generated electromagnetic wave diffracts out of the gyrotron resonator and propagates through the uptapered section followed by an output cylindrical waveguide of radius r_{wg}. Following

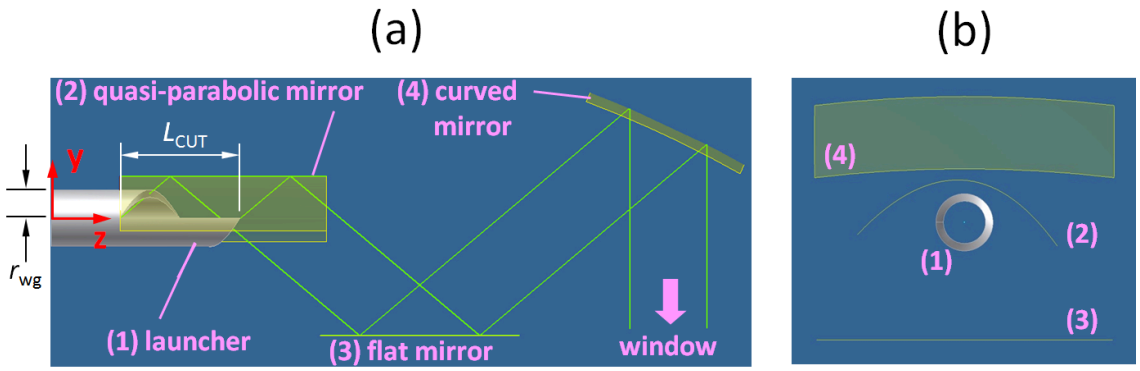

Figure 3-12: Schematic of the 330-GHz quasi-optical internal mode converter: (a) side view and (b) front view.

the described geometrical optics approximation, the cylindrical waveguide mode can be converted to a linearly polarized Gaussian-like microwave beam using the configuration shown in Fig. 3-12. A helical cut in the cylindrical waveguide allow the rays to propagate radially, where the cut length is given by [43]:

$$L_{CUT} = 2\cot\theta_B r_{wg}\left(\frac{\pi}{\psi}\right)\sqrt{1-\left(\frac{r_{caustic}}{r_{wg}}\right)^2} \tag{3.16}$$

These rays are collected by a quasi-parabolic mirror that will transform the set of incoming rays from the waveguide into a set of parallel rays with linear polarization. From the configuration seen in Fig. 3-13, the profile of the quasi-parabolic mirror is given by [38]:

$$y = f_p\left[\tan^2\left(\frac{\varphi}{2}\right)-1\right]+r_{caustic}\left[\frac{\varphi}{2}\tan^2\left(\frac{\varphi}{2}\right)+\tan\left(\frac{\varphi}{2}\right)-\frac{\varphi}{2}\right] \tag{3.17}$$

$$x = 2f_p\tan\left(\frac{\varphi}{2}\right)+r_{caustic}\left[1+\varphi\tan\left(\frac{\varphi}{2}\right)\right] \tag{3.18}$$

The numerical values for the 330 GHz mode converter are summarized in Table 3.5. The profile of the quasi-parabolic mirror is shown in Fig. 3-14.

Table 3.5: Parameters of the quasi-optical 330 GHz internal mode converter

Operating mode	$TE_{-4,3}$
Waveguide radius r_{wg}	2.85 mm
Caustic radius $r_{caustic}$	0.90 mm
Brillouin angle θ_B	40°
Bounce angle ψ	71.6°
Cut length L_{CUT}	16.2 mm
Focal length f_p	5.70 mm

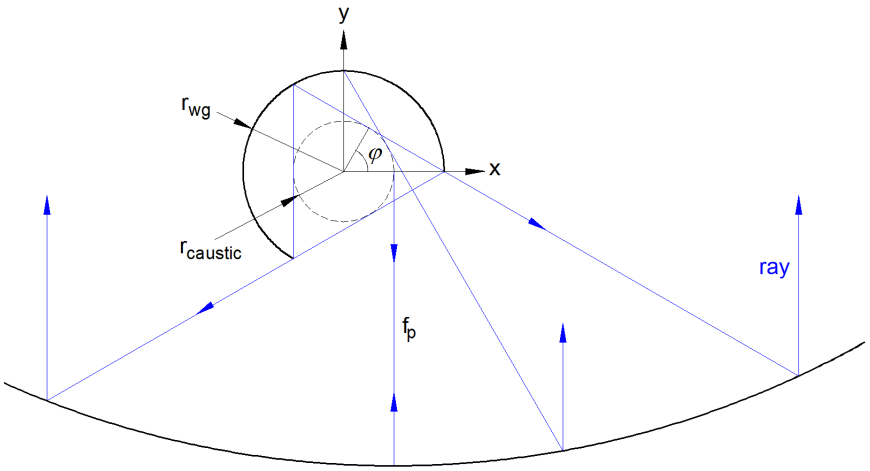

Figure 3-13: Conversion of a cylindrical waveguide mode with caustic $r_{caustic}$ into a linearly polarized wave.

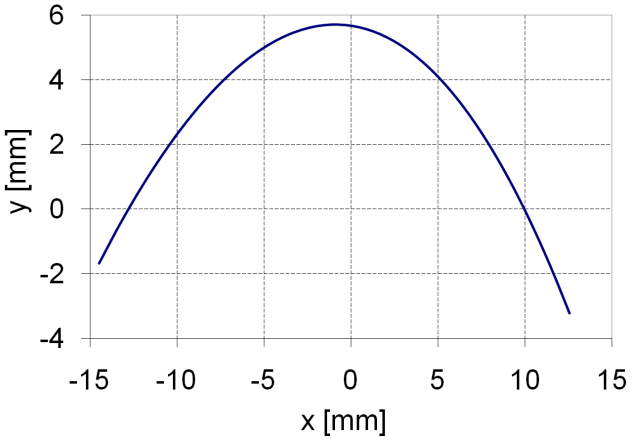

Figure 3-14: Profile of the quasi-parabolic mirror.

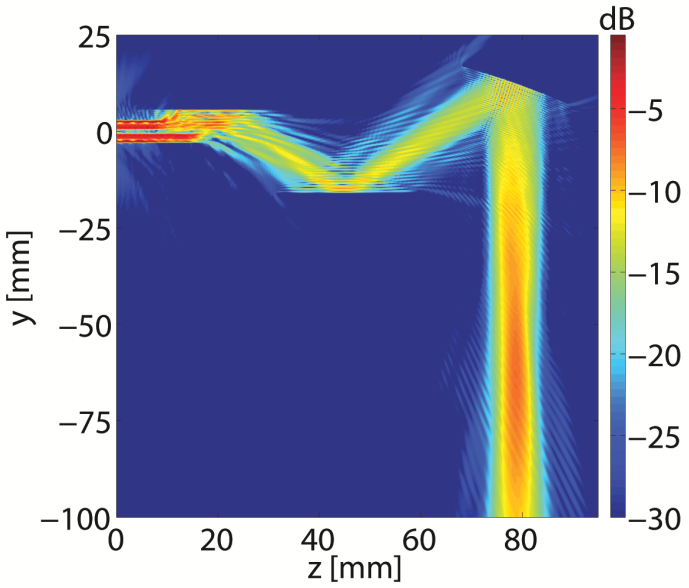

Figure 3-15: Simulated electric field of the microwave output beam at 330 GHz.

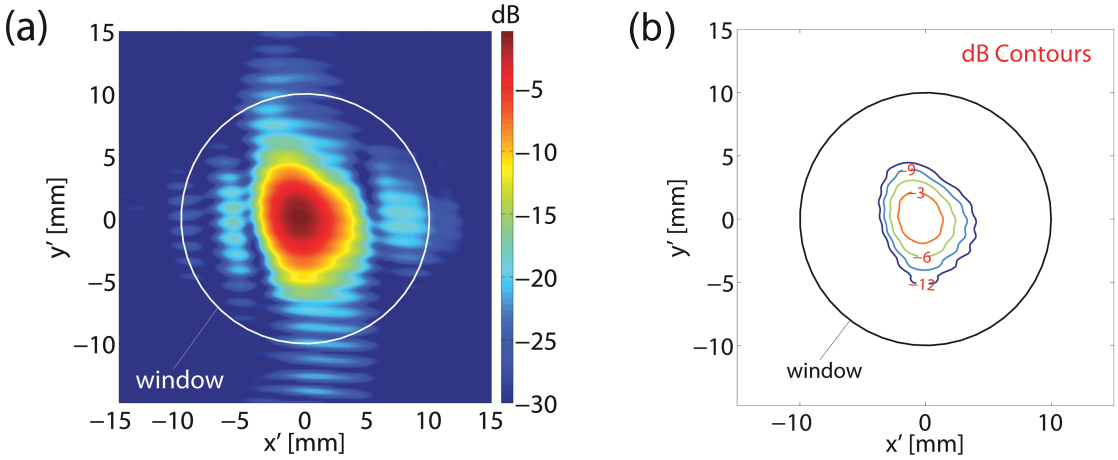

Figure 3-16: Simulated electric field profile of 330-GHz microwave output beam at the focal plane $y = -60$ mm in (a) dB color scale and (b) dB contours. The gyrotron window is shown as a reference.

The mode converter design was evaluated using an electric field integral equation code Surf3d [122, 123]. The results from these calculations are shown in Figs. 3-15 and 3-16. Fig. 3-15 displays the electric field propagation in the helical launcher, the quasi-parabolic mirror, and two additional mirrors to deflect the microwave beam out of the gyrotron through a transparent window located at $y = -20$ mm. The simulated electric field profile at the focal plane $y = -60$ mm is shown in Fig. 3-16 in

dB scale, where the Gaussian-like content was computed to be $\eta_{Gaussian} = 92\%$ with beam radii $w_x = 3.3$ mm and $w_y = 4.2$ mm. The Gaussian-like content $\eta_{Gaussian}$ was obtained from the calculated electric field profile $E(x, y)$ over an area A through the expression [124]:

$$\eta_{Gaussian} = \frac{\left[\int_A E(x,y) \exp\left(-\frac{(x-x_0)^2}{w_x^2} - \frac{(y-y_0)^2}{w_y^2}\right) dxdy\right]^2}{\int_A E^2(x,y)dxdy \int_{-\infty}^{+\infty} \exp\left(-2\frac{(x-x_0)^2}{w_x^2} - 2\frac{(y-y_0)^2}{w_y^2}\right) dxdy} \tag{3.19}$$

where x_0 and y_0 denotes the coordinates of the center of the Gaussian-like beam.

3.5 Auxiliary Components

Besides the cavity and the internal mode converter, other critical components necessary for the gyrotron operation such as the superconducting magnet, the electron gun, the high voltage power supply, the gyrotron window, and the gyrotron collector are described in this section.

3.5.1 Superconducting Magnet

A superconducting magnet is an essential component of the gyrotron since it does not only take part in the electron beam formation and guidance but also it provides the required peak magnetic field $B_0(z = 0) = 0.036\gamma f/n$ T/GHz in the cavity region for an output frequency f at a cyclotron harmonic n. An 8-T unshielded superconducting magnet with an 127-mm-diameter room-temperature bore was ordered from Bruker Biospin AG. A schematic of the magnet is shown in Fig. 3-17 with dimensions in mm. The cavity coil provides the magnetic field in the interaction region and the field-to-current ratio for this coil is 0.06565 T/A according to the vendor. The calibration of the magnet power supply is accurate within 0.2%. The magnetic field is homogeneous within 0.11% in a cylindrical volume of diameter 10 mm and length 30 mm centered at $z = 0$. This is an important requirement in order to keep electrons in synchronism

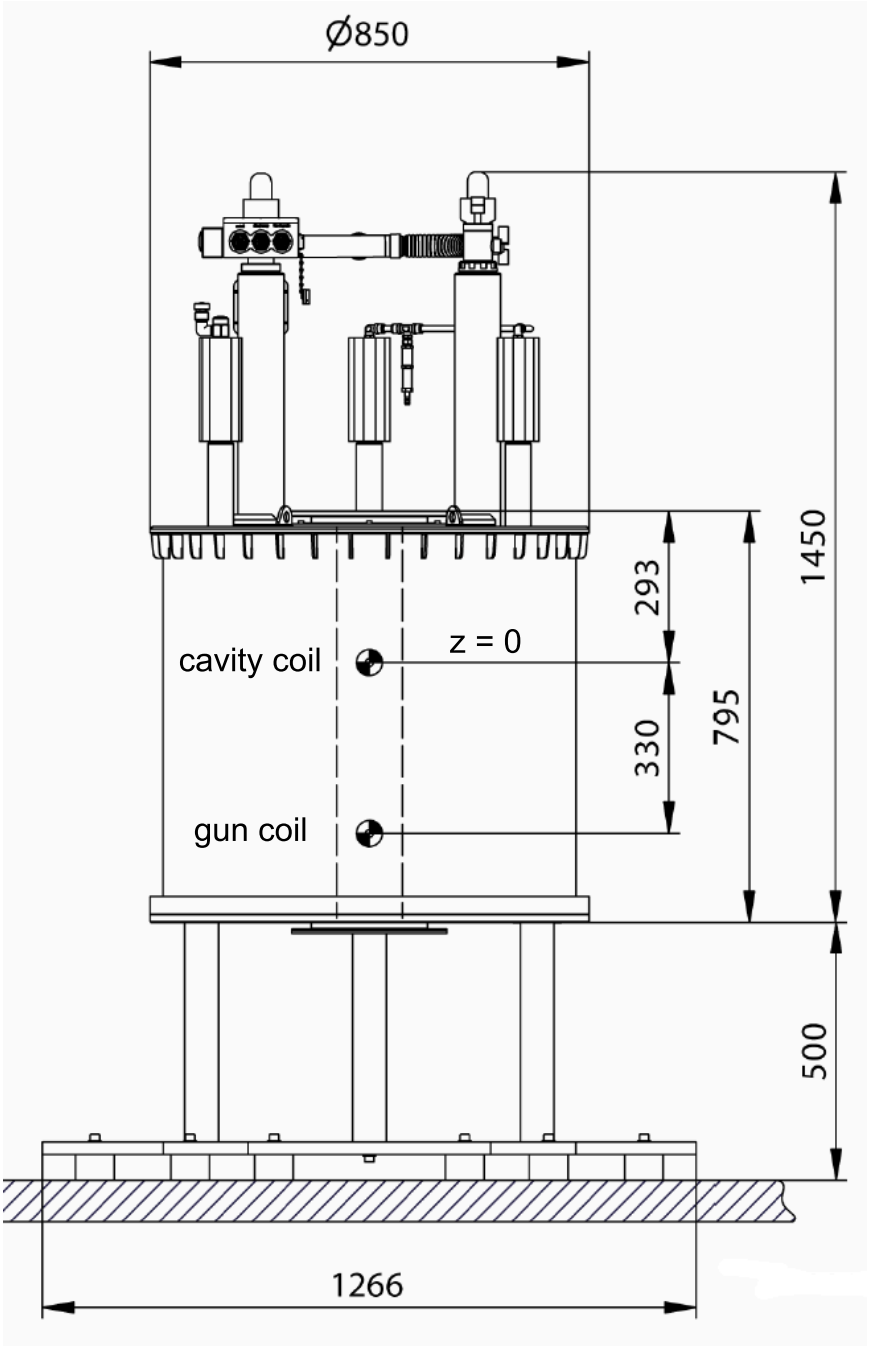

Figure 3-17: Schematic of the Bruker superconducting magnetic. The cavity coil and gun coil are located at $z = 0$ and $z = -330$ mm, respectively. Dimensions are in mm.

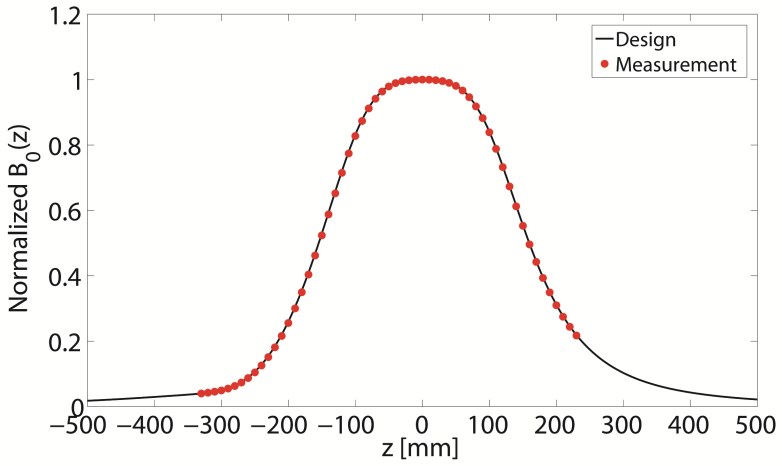

Figure 3-18: Measured and designed magnetic field profile of the Bruker superconducting magnet for gun coil current $I_{gun} = 0$ A.

with the electromagnetic wave. The transverse field tolerance was specified to be $B_\perp/B_z < 0.15\%$.

As shown by experimental results for the 330 GHz gyrotron in Chapter 4, a magnetic shift of 0.03 T can considerably change the radiating frequency/power and a shift greater than that value can cease the excitation of the operating second-harmonic mode. For this reason, the stability of the magnetic field is crucial for a stable gyrotron operation, which is a requirement for long-term DNP/NMR experiments. The drift rate of magnetic field was specified to be -0.01 ppm/h and the value measured by the vendor in persistent mode was found to be -0.009 ppm/h, fulfilling the specification.

An auxiliary coil here referred as a gun coil is located at a position where the peak magnetic field generated by the cavity coil drops to $B_0(z = 0)/25$, which corresponds to the location $z = -330$ mm. The gun coil provides $B_{gun} = \pm 0.31$ T with a field-to-current ratio of 15.5 mT/A and it is utilized to fine tune electron beam parameters such as beam radius and pitch factor α. The theoretical magnetic field profile and the field profile measured by the vendor for $B_{gun} = 0$ are shown in Fig. 3-18 with good agreement. Considering that the magnetic field scales as $B_z(z) \sim 1/z^a$, the fall-off factor a is plotted in Fig. 3-19 for different gun coil currents I_{gun}. A fall-off factor greater than a normal one $a = 3$ for a single coil is observed for $z < 0$ since the field profile had to be shaped so that the field at the gun position $z = -330$ mm would be

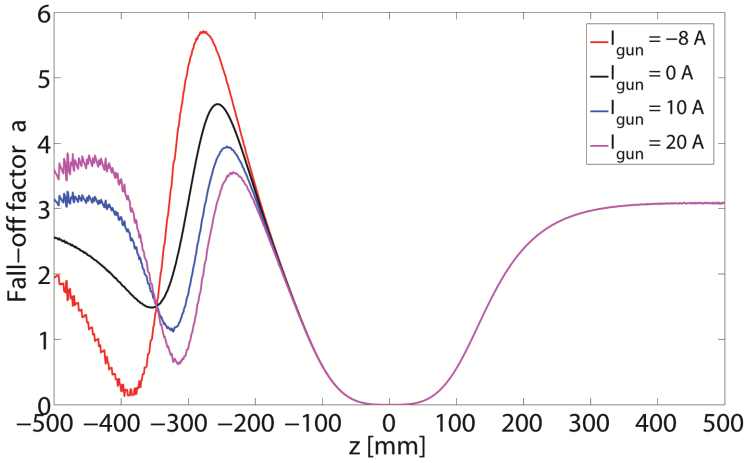

Figure 3-19: Fall-off factor a of the Bruker superconducting magnet for different values of gun coil current I_{gun}.

Table 3.6: Main specifications of the 330 GHz gyrotron magnet

Maximum magnetic field	8.0 T
Operating magnetic field	6.0 T
Cavity coil current	0 - 122 A
Gun coil field	±0.31 T
Cun coil current	±20 A
Field drift rate in persistent mode[i]	-0.009 ppm/h
Field homogeneity in cylinder of height = 30 mm and diameter = 10 mm[i]	$< 0.11\%$
Transverse field tolerance $B_\perp/B_z$[i]	$< 0.13\%$
Room temperature bore ⌀	127 mm
Liquid nitrogen refill time	7 days
Liquid helium refill time in persistent mode	14 days

[i] Measured by the manufacturer.

$B_0(z = 0)/25$. Table 3.6 summarizes the key parameters of the gyrotron magnet.

The 330 GHz gyrotron was first tested in a different superconducting magnet manufactured by Cryomagnetics, Inc. This magnet has a field homogeneity of 0.6% on axis over a 2-cm length around the magnet peak position. According to a NMR probe measurement, the field-to-current ratio for this magnet was estimated to be 0.20084 T/A and the magnetic field drift rate was measured to be less than 0.02 ppm/h [101]. The magnetic field at the cathode location can be adjusted by using a 103-mT water-cooled copper electromagnet installed at the bottom of the magnet and the field-to-current ratio of this electromagnet is 3.4 mT/A according to the vendor. More details about this superconducting magnet are given in Ref. [125]. After the initial evaluation of the 330-GHz gyrotron using the Cryomagnetics magnet, the gyrotron was moved to the Bruker superconducting magnet described here.

3.5.2 Diode Electron Gun

The electron beam in the 330 GHz gyrotron is formed in a diode magnetron injection gun (MIG) composed of a hollow anode electrode and a cathode electrode with a ring emitter of radius $r_c = 5.38$ mm and slant length $l_c = 1.09$ mm. The cathode utilized in this work is referred as a M-type cathode and a typical configuration of this type of cathode utilizes a tungsten matrix impregnated with a compound of BaO among other materials so that the work function of the emitting surface can be reduced. A thin film of a material such as osmium is usually applied to the cathode surface in order to enhance the emission even further [126]. The MIG geometry is shown in Fig. 3-20 along with equipotential lines and electron trajectories using the code EGUN [127] for gyrotron parameters $V_b = 10.1$ kV and $I_b = 190$ mA. The maximum electric field observed in the MIG cathode is 80.8 kV/cm at 10.1 kV, which is below the maximum recommended value of 100 kV/cm to avoid arcing [128].

The beam tunnel section between the MIG and the gyrotron cavity is composed of slotted tubes and a piece of a lossy SiC ceramic (*cf.* Fig. 3-1) in order to lower the quality factor and prevent spurious beam tunnel oscillations that could compromise

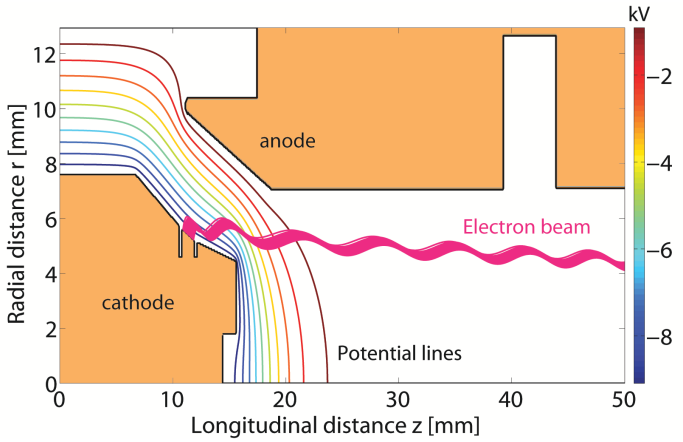

Figure 3-20: Magnetron injection gun geometry along with simulated electron trajectories and equipotential lines for $V_b = 10$ kV, $I_b = 190$ mA, and gun coil field $B_{gun} = 5$ mT.

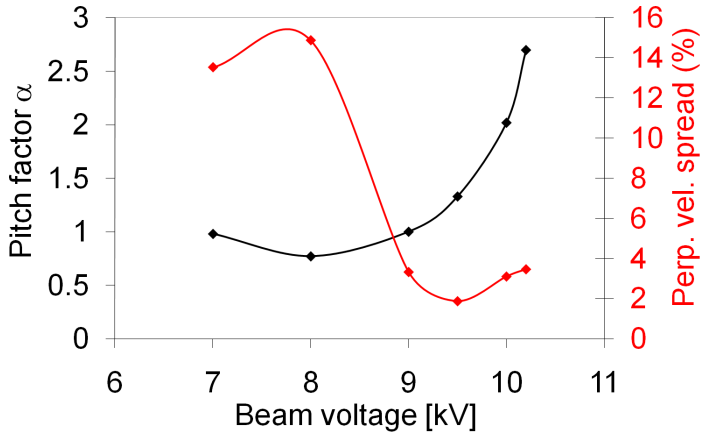

Figure 3-21: Calculated pitch factor α and perpendicular electron velocity spread $\Delta v_\perp / v_\perp$ at the cavity entrance for $I_b = 190$ mA. The gun coil field was set at $B_{gun} = 5$ mT for optimized beam parameters at 10.1 kV.

the beam quality. The beam parameters at the cavity entrance such as perpendicular electron velocity spread $\Delta v_\perp / v_\perp$ and pitch factor α were computed using the code EGUN [127]. The results from these simulations are plotted in Fig. 3-21 where a high α ($\cong 2.0$) and a low spread $\Delta v_\perp / v_\perp$ ($< 4\%$) favorable for beam-wave interaction were obtained at the design voltage $V_b = 10.1$ kV.

3.5.3 High Voltage Power Supply

For CW operation, the beam voltage V_b is provided by a high voltage power supply manufactured by Spellman High Voltage Electronics Corporation, model DF4, and able to generate up to 25 kV, 200 mA, and 4 kW. The power supply was modified from its original application for X-rays generators so that the cathode filament current and the high voltage could be set independently. The supply has a RS232 interface which enables the control of the beam voltage and the cathode filament current along with the monitoring of the beam current. The maximum power output can be adjusted manually below the limit of 4 kW for the protection of the power supply. Stable output voltage is important for reasons similar to the ones described for magnetic field stability in Section 3.5.1. According to the vendor, the long-term stability of the

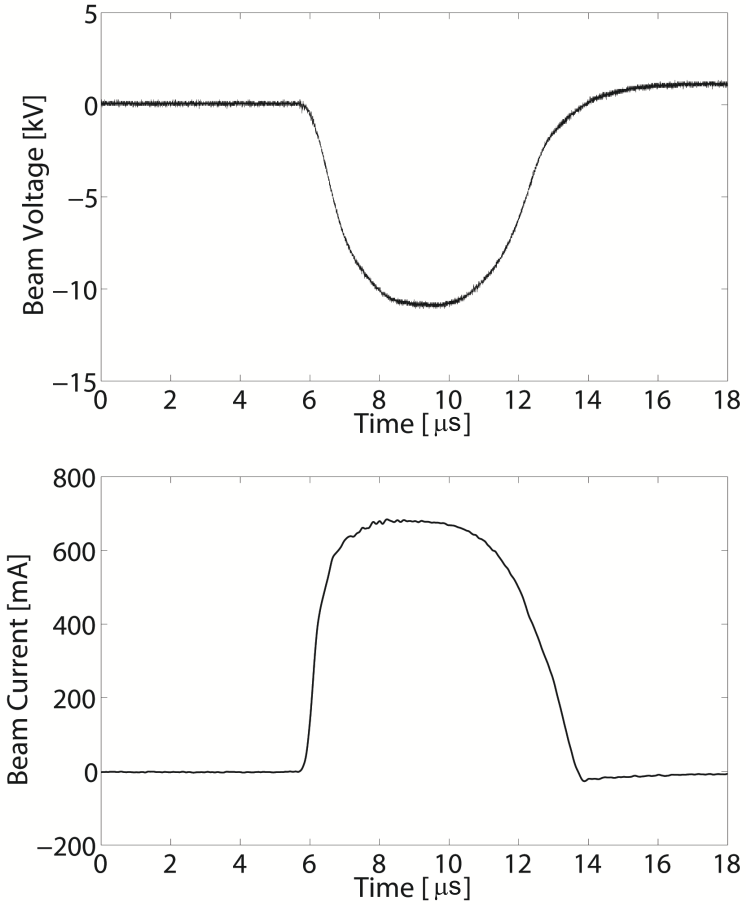

Figure 3-22: Typical beam voltage and beam current traces obtained from pulsed power supply.

output voltage is 0.01% over 8 hours [129].

The 330 GHz gyrotron was also operated in pulsed mode as described in Chapter 4 so that the gyrotron performance could be evaluated at currents higher than limit of 200 mA in the CW power supply. The pulsed power supply consists of a 12-element LC transmission line pulse forming network (PFN) charged by a high voltage power supply and triggered by a thyratron, followed by a pulse transformer to step the voltage pulse up to the required value. The cathode voltage is measured by a capacitive divider that provides a reference voltage. The ratio between the high voltage and the reference voltage was measured to be 5.1 kV/V using a calibrated high voltage probe Tektronix P6015, probe n^{o} 1. A typical high voltage and beam current traces from the pulsed power supply are shown in Fig. 3-22. The beam current during pulsed operation was measured using a 1-V/A Rogowski coil with a 50-Ω termination.

3.5.4 Gyrotron Window

After the mode conversion from a cylindrical waveguide mode to a linearly polarized Gaussian-like beam, the microwave beam is extracted from the gyrotron through a transparent window. For the power levels of several watts to several tens of watts required by DNP/NMR, no cooling has been required for the gyrotron window. For total transmission at a frequency f and normal incidence, the required thickness t of a gyrotron window made of a material with relative permittivity $\varepsilon_r = \varepsilon/\varepsilon_0$ is:

$$t = N\frac{c}{2f\sqrt{\varepsilon_r}} \tag{3.20}$$

where N is a positive integer.

The material chosen for the 330-GHz gyrotron window was fused silica (SiO_2, Corning 7980 UV) with $\sqrt{\varepsilon_r} \cong 1.955$ for broadband transmission. The window was fabricated by Specialty Glass Products with diameter 31.75 ± 0.13 mm, thickness 2.090 ± 0.013 mm, top and bottom surface finishing ≤ 50 nm, 20/10 scratch/dig, and

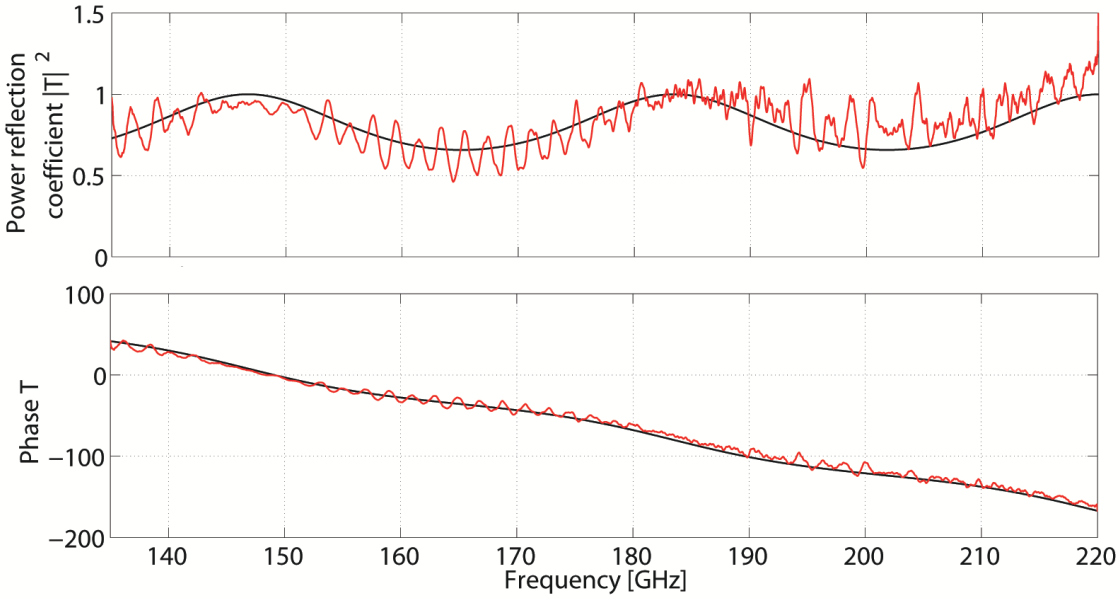

Figure 3-23: Amplitude and phase of the transmission wave coefficient T through the fabricated gyrotron window. The design is shown as a black line while the measurement is indicated by a red line.

parallelism $\leqslant 5$ μm.

The transmission of the fabricated window was evaluated using an Agilent E8363B VNA and the results are shown in Fig. 3-23 in good agreement with the design for a normal incident wave where total transmission is expected at 146.67 GHz, 183.34 GHz, 220 GHz, 256.67 GHz, 293.34 GHz, and 330 GHz. The design curve in Fig. 3-23 was obtained from a computer code written to calculate the transmission and reflection of a TE plane wave at an arbitrary incident angle traveling through a stratified medium composed of layers made of different lossless non-magnetic dielectric materials [120]. For the frequency range of interest between 328 and 332 GHz, the gyrotron window has good transmission with a calculated power transmission coefficient being greater than 0.983.

3.5.5 Collector

After being separated from the microwaves by the internal mode converter, the spent electron beam is allowed to expand in the decaying field of the superconducting

magnet, reducing the thermal load deposited on a water-cooled grounded collector to levels manageable by a single-phase water cooling circuit. In the worst case scenario where no microwaves are generated, the collector has to withstand the full CW beam power P. The temperature rise ΔT of water in the cooling circuit due to P is given by:

$$\Delta T_{water} = \frac{P}{\rho_{water} \dot{V}_{water} c_p} \tag{3.21}$$

where ρ_{water} is the water density ($\rho_{water} = 1000$ kg/m^3 at 0℃), $\dot{V}_{water}$ is the water volumetric flow rate, and c_p is the water specific heat capacity ($c_p = 4.1813$ kJ/kg·K). For a water flow rate $\dot{V}_{water}$ in U.S. liquid gallons per minute (gpm), one has $\Delta T_{water} = 0.0038 P/\dot{V}_{water}$ for ΔT in K and thermal load P in W. For a load $P = 3$ kW and a water flow rate of 1 gpm, one obtains $\Delta T_{water} = 11.4$℃.

The power density of the collector wall can be determined by the area of interception of the electron beam at the collector. Following a result from Busch's theorem in Section 2.1, the axial beam width of electrons incident on a 18-mm diameter collector wall is 7.1 cm. This results in an area of interception of 39.66 cm^2 and in a power density $P_{coll} = 76$ W/cm^2 for a spent beam power of 3 kW. For a collector with a copper wall of thickness $t_{coll} = 3.8$ mm, the estimated temperature difference $\Delta T_{wall} = P_{coll} t_{coll}/k_{Cu}$ is 7.2℃, where k_{Cu} is the copper thermal conductivity ($k_{Cu} = 401$ W/m·K).

Chapter 4

Operation of a Tunable 330-GHz Second-Harmonic Gyrotron

After the design phase was completed, the tunable 330-GHz second-harmonic gyrotron was fabricated and its performance was experimentally evaluated as described in this chapter. The experimental setup to run the 330-GHz gyrotron is explained in Section 4.1 while the diagnostics utilized to measured the gyrotron power, frequency, ohmic loss, and microwave beam profile are detailed in Section 4.2. Experimental results for output power and frequency tunability as a function of magnetic field, beam voltage, and cavity cooling temperature are presented in Sections 4.3 and 4.4 for measurements carried out in the Cryomagnetics superconducting magnet and in the Bruker superconducting magnet, respectively. Other experimental data mentioned in these sections include the start oscillation current of the operating mode, ohmic loss, frequency and power stability in long-run continuous operation, and the output microwave beam profile. This chapter is finalized with discussions in Section 4.5.

4.1 Experimental setup

In addition to the high-voltage CW power supply and the superconducting magnet detailed in Section 3.5.3 and Section 3.5.1, respectively, the other components necessary for the gyrotron operation are shown in Fig. 4-1. The ultra-high vacuum level

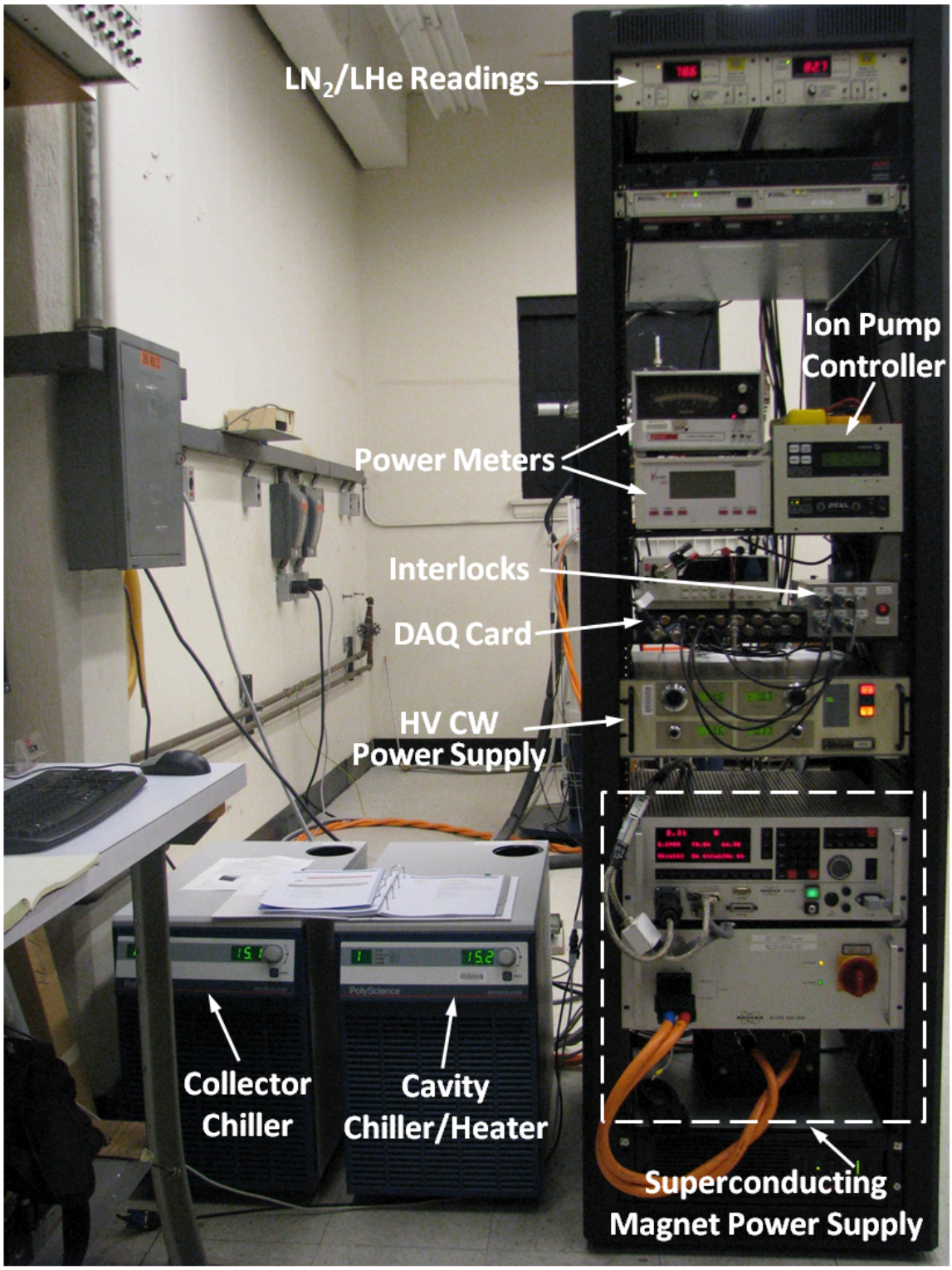

Figure 4-1: Control rack and chillers for the 330-GHz CW gyrotron system.

on the order of 10^{-9} to 10^{-8} Torr is maintained in the tube by a Varian ion pump, model Vaclon Plus 20 StarCell with capacity of 20 l/s, connected to a Varian Dual ion pump controller. The pump controller has an interlock relay that trips for a pressure above 10^{-6} Torr and the pressure reading can be monitored via a RS232 interface.

For CW operation, the cavity temperature is stabilized by a Polyscience chiller / heater, model 5706T, with cooling capacity of 2.5 kW at 20℃ and temperature stability of ±0.1℃. This chiller has an operating temperature range from -10℃ to 70℃, enabling thermal tuning of the gyrotron cavity. The electron beam power dissipated on the collector is removed using a Polyscience chiller, model 6106T, with cooling capacity of 2.9 kW at 20℃. The water temperature and flow rate at both the cavity and collector cooling channels are monitored using the analog outputs of flowmeters fabricated by Proteus Industries Inc., model 4004PN4-T. Besides these analog outputs, the flowmeters also have a built-in relay with trip points manually adjusted for temperature and flow rate. The relays existent in the flowmeters and in the ion pump controller form a hardware safety interlock network able to shut off the beam voltage and the cathode filament current to protect the gyrotron. The external part of the electron gun is cooled by forced air.

The gyrotron is computer controlled and monitored using the software LabVIEW. A picture of the computer user interface for the gyrotron control is shown in Fig. 4-2. Interlocks are also implemented in software and they provide extra protection for variables not covered by hardware interlocks such as beam voltage, beam current, body current, and cathode filament current. Body current refers to the beam current intercepted by the body of the tube and its level during the 330-GHz operation is usually below 0.1% of the beam current value. The body current and other analog inputs such as the flowmeter readings and diode voltage for power measurement are interfaced with the computer through a data acquisition (DAQ) card manufactured by Measurement Computing, model USB-1616HS-BNC. In order to reduce the noise in these analog readings, each analog input is connected to a 33-Hz low-pass filter before being sampled. The body current is measured through a 49.9-Ω resistor connected between the tube body and ground. The body current DAQ channel is protected by

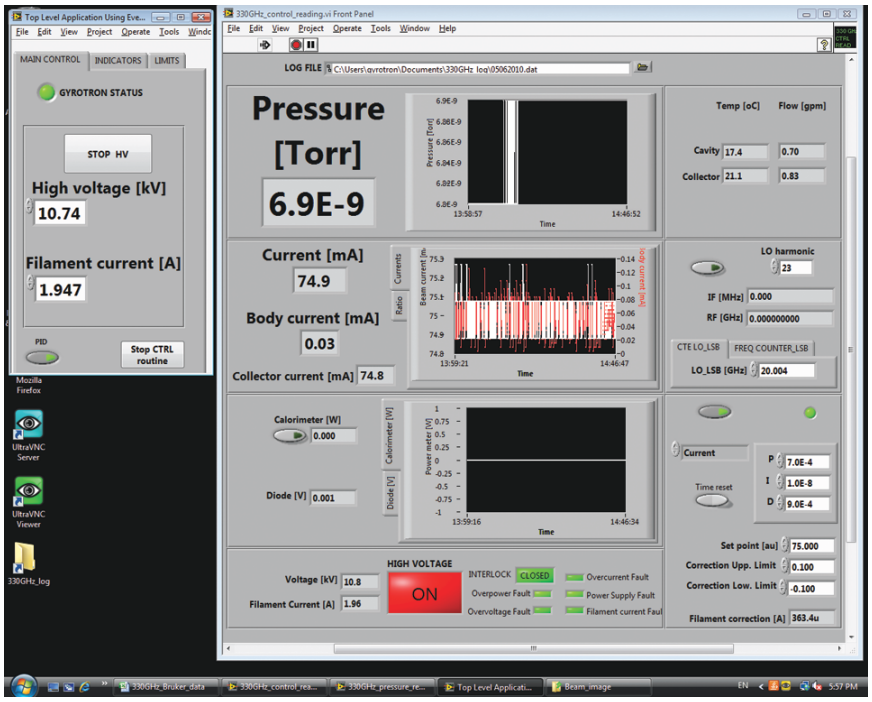

Figure 4-2: Front panel user interface for gyrotron monitoring and control.

a Zener diode clipper that restricts the voltage across the body resistor to 11 V.

4.2 Diagnostics

This section details the various diagnostics utilized to evaluate the gyrotron output power, frequency, ohmic loss, and microwave output beam profile.

4.2.1 Power

In CW operation, the output power of the 330-GHz gyrotron was measured using a laser disc calorimeter fabricated by Scientech Inc., model 36-0401 (serial nº 477), connected to a Scientech analog reader 364. In a disc calorimeter, a thermopile is located between an absorbing disc and a heat sink. When the absorbing disc is heated by the incoming radiation, a temperature difference is developed between the disc and the heat sink, generating a heat flow and a measurable potential difference through the thermopile. The calorimeter head used in the experiment has a circular absorbing area with a 10-cm diameter and the power reflection coefficient on its surface was

measured to be 23% at 330.1 GHz using a diode detector and considering an incident angle of 40°. The accuracy of the analog reader was found to be better than 10% according to measurements using the built-in DC heater in the calorimeter head as a reference.

During pulsed operation, the average power was measured using a Scientech laser calorimeter, model 360001 (serial nº 1437), and a Scientech analog reader 362. The reflection coefficient of the disc calorimeter surface with aperture of 2.54 cm was measured to be 25% at 330.1 GHz and the readings from the analog reader had to be corrected by a factor of 1.2. The microwave output pulse was measured using a Pacific Millimeter Products diode, model HD (serial nº 18). Based on the information available for the average power P_{av}, the pulse duration t_{FWHM} at full width at half maximum (FWHM), and the pulse repetition frequency (PRF), the peak power P_{peak} in pulsed operation could be estimated as:

$$P_{peak} = 1.6 \frac{P_{av}}{t_{FWHM} PRF} \tag{4.1}$$

where the factor 1.6 takes into account reflections from the calorimeter surface and deviation in the calorimeter analog reader. The power measurements were performed after a corrugated waveguide connected to the gyrotron output. The corrugated waveguide utilized in these measurements has an inner diameter of 19 mm and a corrugation depth of $\lambda/4$ at 460 GHz [130].

4.2.2 Frequency

The gyrotron frequency in the submillimeter band was measured using the heterodyne receiver system shown in Fig. 4-3. The incoming gyrotron radiation f_{RF} is picked up by a horn antenna and downconverted to an intermediate frequency f_{IF} by mixing the gyrotron signal with the h^{th} harmonic of the local oscillator (LO) frequency f_{LO}.

The mixer utilized in this setup is a Pacific Millimeter Products WR-3 harmonic mixer, model HM (serial nº 12), which is connected to a Pacific Millimeter Prod-

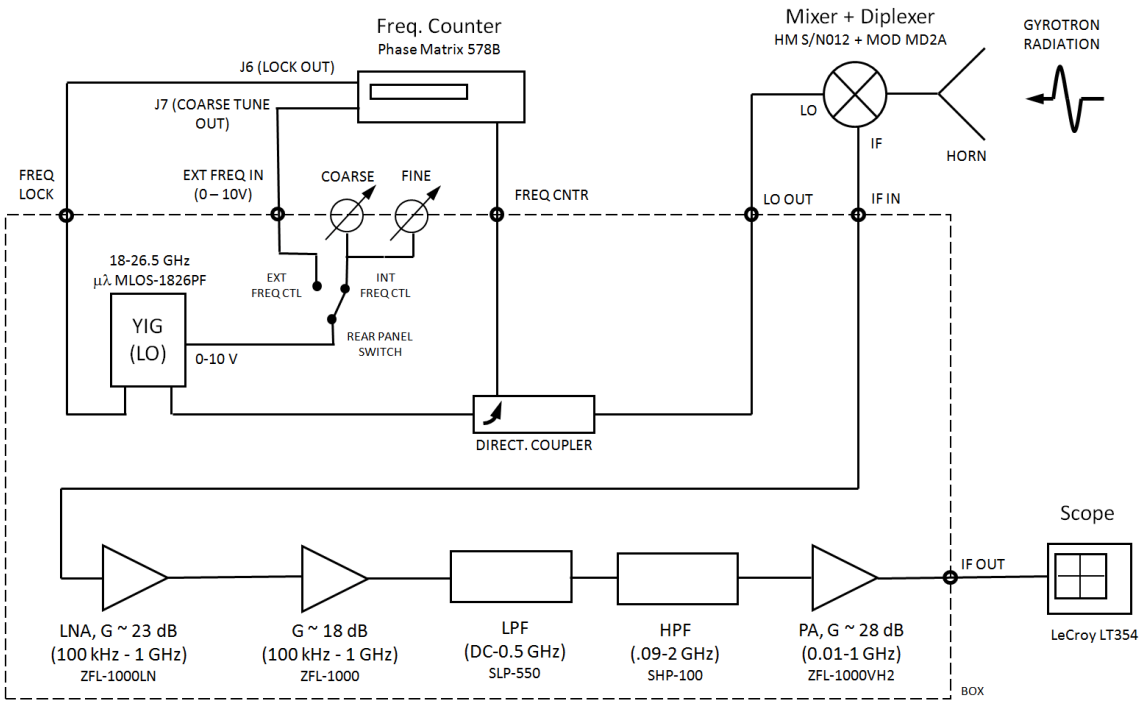

Figure 4-3: Schematic of the heterodyne receiver system for frequency measurement.

ucts diplexer, model MD2A. The LO signal is provided by a Micro Lambda Wireless YIG oscillator, model MLOS-1826PF, voltage tunable over 18-26.5 GHz. The LO frequency is measured by a Phase Matrix frequency counter, model 578B. This counter has an automatic source locking capability able to stabilize the frequency of an electronically tunable source such as the YIG oscillator, which is important for an accurate frequency measurement in long-term gyrotron operation. After the downconversion, the IF signal is amplified and filtered, and the resulting signal in the range of 0.09-500 MHz is Fourier transformed in real time by a fast Fourier transform (FFT) operation performed in a LeCroy 500-MHz oscilloscope, model LT354.

For a given f_{IF}, there are two LO frequencies $f_{LO,upper}$ and $f_{LO,lower}$ that can result in the same f_{IF}:

$$f_{IF} = f_{RF} - hf_{LO,lower} \tag{4.2}$$

$$f_{IF} = hf_{LO,upper} - f_{RF} \tag{4.3}$$

Combining both equations, one can find the operating mixer harmonic h in order

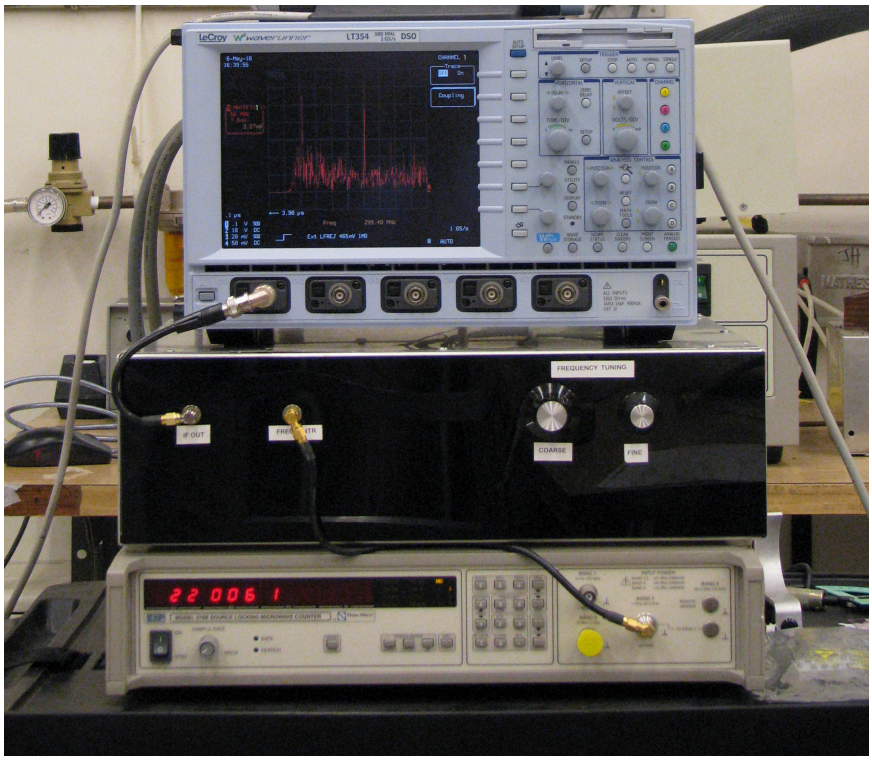

Figure 4-4: Picture of the heterodyne receiver system depicting, from bottom to top, the frequency counter, the heterodyne receiver, and the oscilloscope.

to obtain the unknown f_{RF}:

$$h = \frac{2f_{IF}}{f_{LO,upper} - f_{LO,lower}} \tag{4.4}$$

The 330-GHz signal can be observed for mixer harmonics between 15 and 17. A picture of the heterodyne system is shown in Fig. 4-4, where the oscilloscope displays the gyrotron signal downconverted from $f_{RF} = 329.79$ GHz to a FFT peak at $f_{IF} = 300$ MHz for $f_{LO,upper} = 22.0061$ GHz and $h = 15$.

4.2.3 Ohmic Loss

The portion of the generated microwave power dissipated on the gyrotron cavity walls, which constitutes the ohmic loss P_{load}, can be estimated by measuring the water temperature rise ΔT_{water} and the flow rate $\dot{V}_{water}$ in the cavity cooling channel as follows from Eq. (3.21). While the inlet and outlet water temperatures in the

cavity cooling channel are monitored by negative temperature coefficient thermistors, Omega model 44008, the flow rate is provided by a flowmeter described in Section 4.1.

4.2.4 Microwave Beam Pattern

The output microwave beam pattern can be evaluated using different techniques such as an array of pyroelectric elements, thermal paper, liquid crystal sheet, and thermal-sensitive phosphor.

A Spyricon Pyrocam III pyroelectric camera was utilized to assess the output radiation pattern from the gyrotron at low microwave power. The camera consists of an array of 124-by-124 $LiTaO_3$ pyroelectric sensors with a spacing of 100 μm between each pixel, yielding an active area of 12.4 mm by 12.4 mm. Since the pyroelectric sensors are only sensitive to alternating signals, the incoming CW microwave beam was modulated at a rate of 24 or 48 Hz by a built-in chopper located over the active detection area. During the measurements with the pyroelectric camera, the output power of the gyrotron was kept below the threshold of 2 W for camera sensor damage.

Evaluation of the output radiation pattern at higher microwave power can be carried out by using thermal paper, liquid crystal sheet, or thermal-sensitive phosphor. A typical thermal paper consists of a base paper impregnated with chemicals that darkens when exposed to heat. The thermal paper can form an image of microwave beam when it is placed on a microwave absorber surface. Similarly, an image of the beam can also be observed on a liquid crystal sheet with a color spectrum response as a function of temperature. Another technique utilized in this work relied on striking the output microwave beam on a thermal-sensitive surface covered with phosphors. These phosphors fluoresce when illuminated by a long wavelength ultraviolet light (3600 Å) and the intensity of fluorescence decreases with increasing temperature, enabling an image to be produced in the area heated by the gyrotron microwave beam.

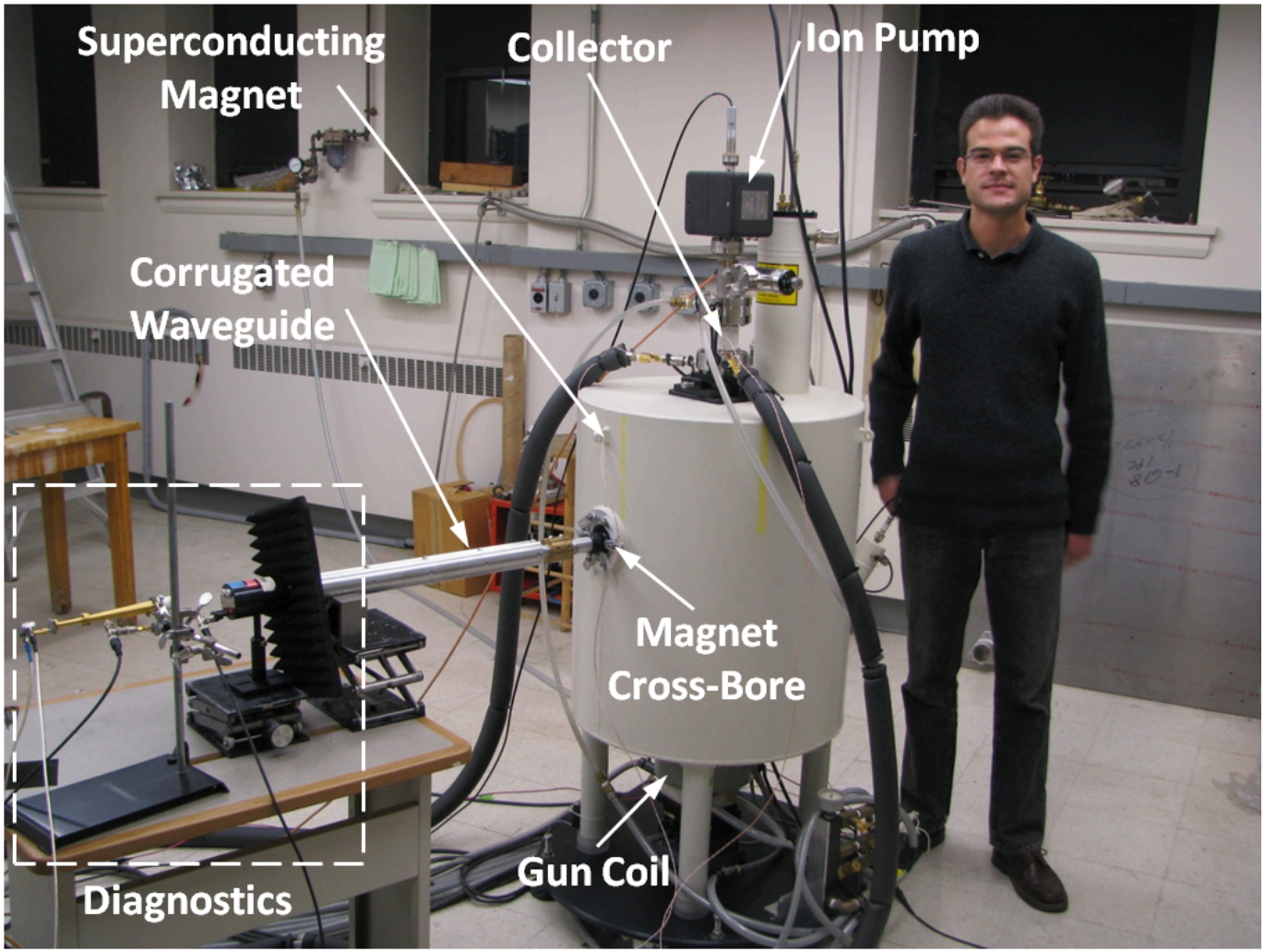

Figure 4-5: Photograph of the author and the 330-GHz gyrotron installed in the Cryomagnetics magnet.

4.3 Experimental Results (Cryomagnetics Magnet)

The performance of the 330-GHz gyrotron was first evaluated using a superconducting magnet manufactured by Cryomagnetics. A picture of the 330-GHz gyrotron installed in this magnet is shown in Fig. 4-5. The microwaves are extracted using a corrugated transmission line installed in the horizontal cross-bore of the superconducting magnet. In this system, the magnetic field at the gun location can be adjusted by using a 103-mT water-cooled copper electromagnet located at the bottom of the magnet. The results and analysis of the measurements carried out in this system are described below.

4.3.1 Start Oscillation Current

The start oscillation current of the operating mode $\mathrm{TE}_{-4,3}$ was measured in CW mode as a function of the magnetic field B_0 for a fixed beam voltage $V_b = 10.1$ kV. The result of this measurement is shown as a solid black line in Fig. 4-6 along with a red diamonds displaying the measured frequency at each start current value. The minimum start current was measured to be 33 mA. Also plotted in this graph are the theoretical start currents for the first six axial modes $\mathrm{TE}_{-4,3,q}$, where $q = 1, 2, 3, 4, 5, 6$. The theoretical start currents were obtained from linear theory (*cf.* Section 2.4) for beam parameters $V_b = 10.1$ kV, $\alpha = 1.8$, and no velocity spread. A cavity radius $r_{cav} = 1.833$ mm was chosen for best fit for the start current calculations, which is within the experimental error of the value (1.834 mm) obtained from the cavity cold test described in Section 3.3.2.

Good agreement is obtained between the measured start current values and the prediction from linear theory, indicating that high-order axial modes are being excited in the experiment. In addition, the measured frequency range for the start current between 329.88 GHz and 331.13 GHz is in reasonable agreement with the range for high-order axial modes as presented in Table 3.2. Frequency detuning may exist at the lower edge of the excitation zone for $B_0 < 6.01$ T since the measured power at these start current values is greater than 1.4 W. The neighboring fundamental mode

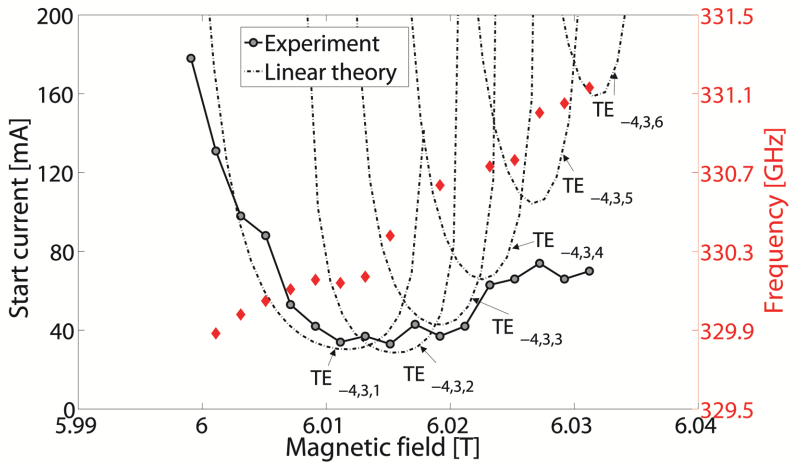

Figure 4-6: Measured start oscillation current (black solid line) and measured frequency (red diamonds) of the operating mode $TE_{-4,3}$ as a function of magnetic field for beam voltage $V_b = 10.1$ kV, $T_{water} = 20$℃. Theoretical start currents (black dash-dotted lines) based on linear theory for the first six axial modes $TE_{-4,3,q}$, where $q = 1, 2, 3, 4, 5, 6$ (simulation parameters: $r_{cav} = 1.833$ mm, cold-cavity axial field profile, $V_b = 10.1$ kV, $\alpha = 1.8$, no beam velocity spread).

$TE_{5,1}$ is excited for magnetic field values $B_0 > 6.035$ T.

4.3.2 Power and Frequency Tuning

The 330-GHz gyrotron has generated 18 W of output power in the second-harmonic mode $TE_{-4,3}$ for a 10.1-kV 190-mA electron beam, corresponding to an efficiency of 0.93%. In addition, a smooth continuous frequency tuning range of 1 GHz has been achieved as a function of magnetic field as shown in Fig. 4-7. This represents a significant improvement in continuous tuning range for a second-harmonic mode in a submillimeter-wave gyrotron compared to the state-of-the-art of 50 MHz at the beginning of this project. Also, the obtained tuning range covers the frequency that yield the maximum DNP/NMR enhancement, which corresponds to 329.4 GHz. In the magnetic tuning measurement, the gyrotron output power was optimized by adjusting the subtracting gun coil field from $B_{gun} = -3$ mT to $B_{gun} = -5$ mT as the main magnetic field was increased, resulting in a minimum output power of 2 W throughout the frequency tuning range.

Comparing the magnetic tuning data with the measured start current, one can

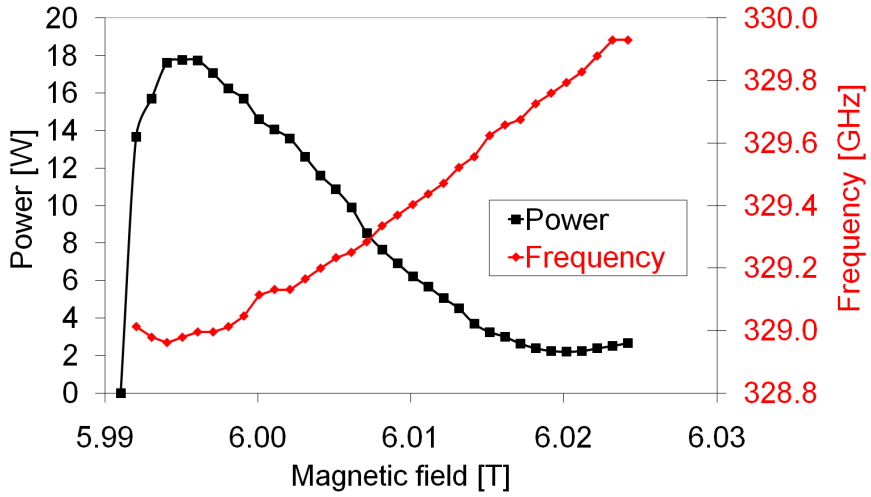

Figure 4-7: Power (black line) and frequency tuning (red line) measurement as a function of magnetic field for beam voltage $V_b = 10.1$ kV, beam current $I_b = 190$ mA, and water temperature in the cavity cooling channel $T_{water} = 9$℃. The gun coil was swept from $B_{gun} = -3$ mT to $B_{gun} = -5$ mT for best output power as the magnetic field was increased.

verify that microwaves are being excited at current values lower than the start current for $B_0 < 6.0$ T. This region corresponds to the hard excitation region and it is accessible by lowering the magnetic field after first exciting microwaves at a higher magnetic field value.

Another difference observed between Fig. 4-6 and Fig. 4-7 is the frequency down-shift in Fig. 4-7. The 330-GHz gyrotron utilizes the same cavity cooling configuration adopted previously in the 460-GHz gyrotron described in Chapter 5. As it is detailed in Section 4.3.3, the cavity cooling circuit only covers a fraction of the cavity area to handle the cavity ohmic loss, yielding a higher thermal resistance, a higher cavity inner wall temperature, and a temperature gradient along the cavity. As a result of this temperature gradient, the cavity straight section undergoes a non-uniform deformation, detuning the microwave frequency in higher power CW operation. Detuning of the microwave frequency is also observed at the edge of the interaction in Fig. 4-7, where the frequency increases as the output power drops from the maximum power point for lower magnetic field values.

Due to the dependence of the electron cyclotron frequency on beam voltage, continuous tuning range of 1 GHz was also achieved as a function of beam voltage for a

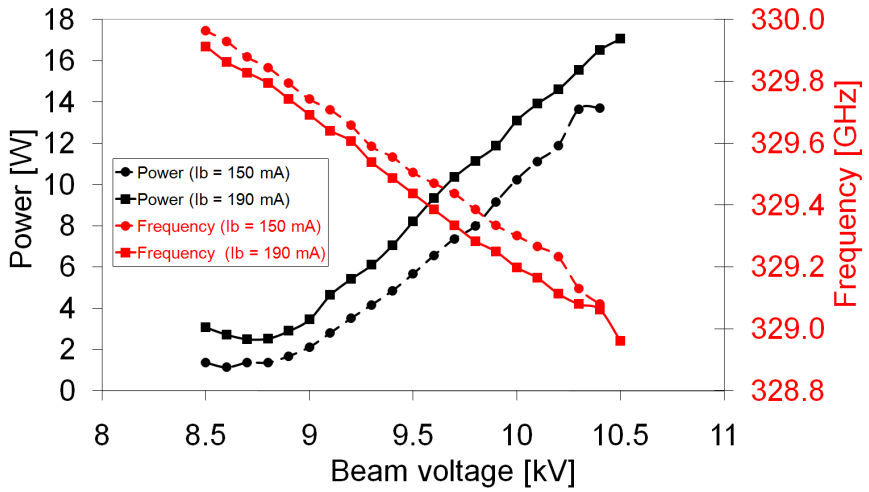

Figure 4-8: Power (black line) and frequency tuning (red line) measurement as a function of beam voltage for magnetic field $B_0 = 6.003$ T, and water temperature in the cavity cooling channel $T_{water} = 9$℃. Circular and square markers represent measurements taken at beam current $I_b = 150$ mA and $I_b = 190$ mA, respectively. For $I_b = 190$ mA, the gun coil was swept from $B_{gun} = 1$ mT to $B_{gun} = -25$ mT for best output power as the beam voltage was decreased.

constant magnetic field as indicated in Fig. 4-8. As the beam voltage was decreased from the maximum power point, the gun coil field had to be swept from $B_{gun} = 1$ mT to $B_{gun} = -25$ mT to optimize the gyrotron power for a beam current $I_b = 190$ mA. The power and tuning response obtained for voltage tuning are similar to the ones measured for magnetic tuning. This can be clearly seen by plotting the voltage and magnetic tuning results as a function of the cyclotron frequency as seen in Fig. 4-9. This shows that magnetic and voltage tuning provide two different knobs for the same basic tuning mechanism based on the dependence of the synchronism condition on the cyclotron frequency. One advantage of voltage tuning over magnetic tuning is the possibility of faster frequency sweep that may be explored in future DNP/NMR experiments [69]. In Fig. 4-8, frequency detuning can also be verified as the beam current and output microwave power are increased.

Another feature utilized to provide additional tunability was thermal tuning. By increasing the water temperature in the cavity cooling channel, the gyrotron cavity will expand and the beam voltage necessary to keep the same synchronism and efficiency condition has to be increased for a fixed magnetic field. This effect is observed

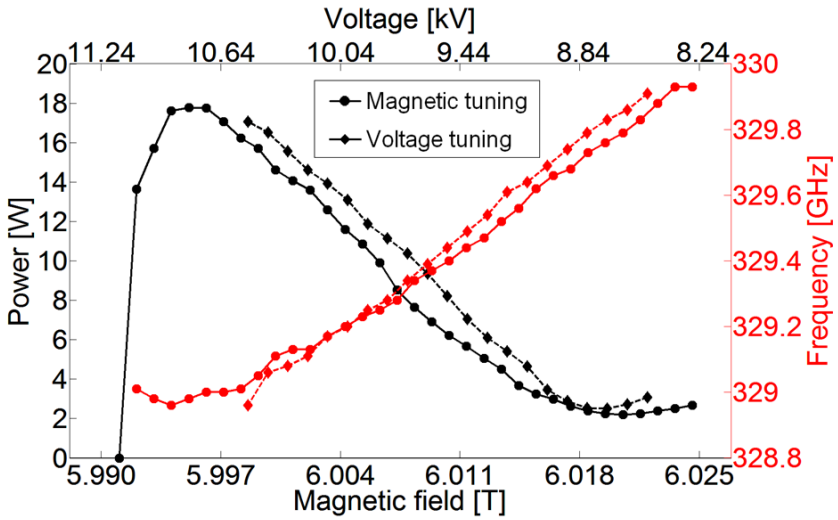

Figure 4-9: Magnetic tuning (circular markers, bottom abscissa) and voltage tuning (diamond markers, top abscissa) measurement for beam current $I_b = 190$ mA and water temperature in the cavity cooling channel $T_{water} = 9$℃. The magnetic and voltage tuning data were taken at $V_b = 10.1$ kV and $B_0 = 6.003$ T, respectively. Each point on the top and bottom abscissa corresponds to the same electron cyclotron frequency value.

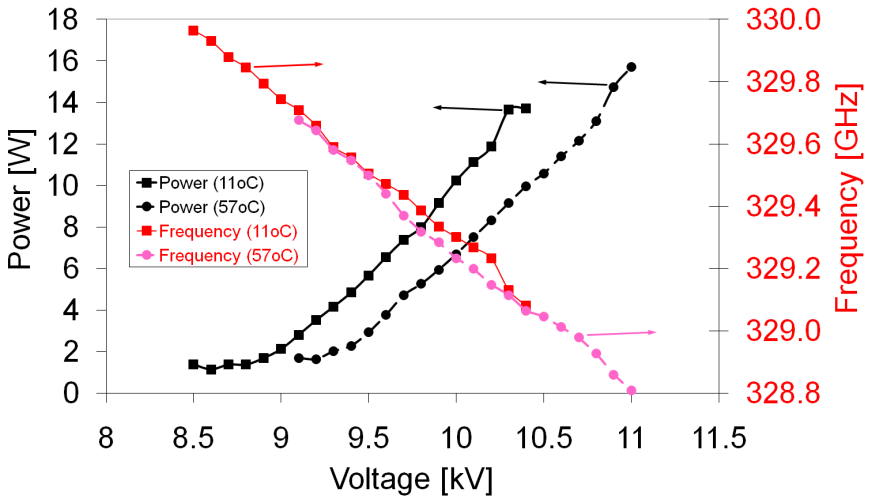

Figure 4-10: Voltage tuning measurement for magnetic field $B_0 = 6.003$ T, beam current $I_b = 150$ mA, along with cavity cooling channel temperature $T_{water} = 11$℃ (square markers), and $T_{water} = 57$℃ (circular markers).

in the measurement shown in Fig. 4-10 as the power curve shifts to higher voltage values as the water temperature T_{water} is increased from 11℃ to 57℃. An additional tuning range of 250 MHz was obtained using thermal tuning.

4.3.3 Ohmic Loss

At a submillimeter wavelength, a considerable part of the power extracted from the electron beam is dissipated in the cavity walls as ohmic loss. Utilizing the wet calorimetric technique outlined in Section 4.2.3, the ohmic loss in the 330-GHz gyrotron was estimated as a function of the beam current for $B_0 = 6.007$ T, $V_b = 10.1$ kV, and flow rate $\dot{V}_{water} = 0.67$ gpm as indicated in Fig. 4-11. The extraction efficiency at $I_b = 175$ mA was computed to be $\eta_{RF} = 7.4\%$. Besides the high ohmic loss at high-frequency operation, another factor that contributes for the observed extraction efficiency is the use of a long resonant structure. Although a long cavity lowers the start oscillation current for the excitation of high-order axial second-harmonic modes, enabling broadband continuous tunability, the diffraction loss is decreased (*cf.* Eq. (2.37)).

Besides ohmic loss, another information needed to estimate the temperature rise in the gyrotron cavity is the convective heat transfer coefficient h_c in the cavity cooling

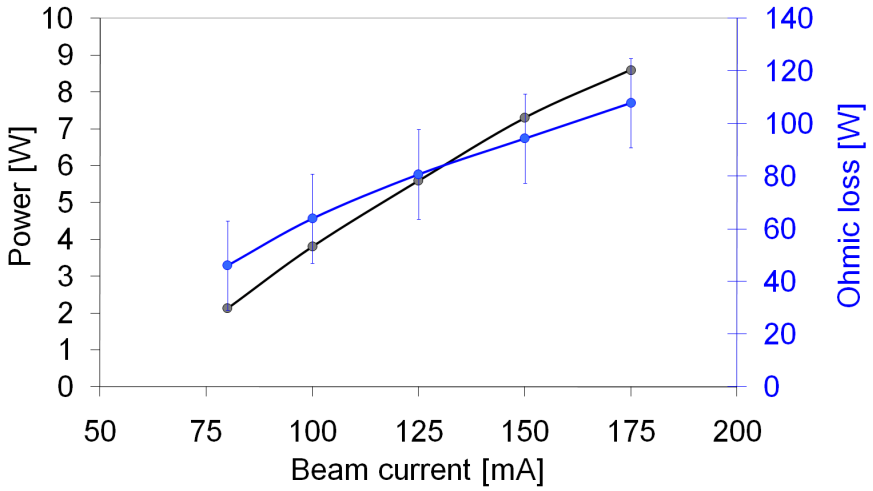

Figure 4-11: Output power and associated ohmic loss as a function of beam current for beam voltage $V_b = 10.1$ kV, magnetic field $B_0 = 6.007$ T, and water flow rate $\dot{V}_{water} = 0.67$ gpm.

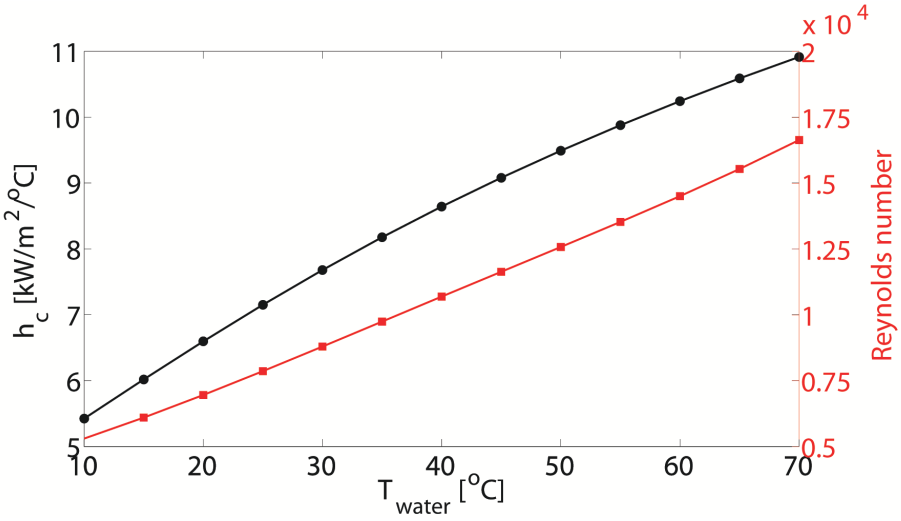

Figure 4-12: Convective heat transfer coefficient h_c and Reynolds number R_e as a function of the water temperature T_{water} for a water flow $\dot{V}_{water} = 0.7$ gpm in a rectangular channel of width $w = 3.6$ mm and height $h = 8.9$ mm.

channel. For a cooling channel with a rectangular cross-sectional area $A = wh$, where w and h are the width and height of the channel, respectively, and a hydraulic diameter $D_h \equiv 4A/(2(w+h))$, the heat transfer coefficient h_c can be estimated by the following expression [131]:

$$h_c = \left(\frac{\kappa}{D_h}\right)\left(\frac{(f/8)(R_e - 1000)Pr}{1 + 12.7\sqrt{f/8}(Pr^{2/3} - 1)}\right) \tag{4.5}$$

where κ is the water thermal conductivity, $Pr = \upsilon c_p/\kappa$ is the water Prandtl number, υ is the water viscosity, c_p is the water specific heat capacity ($c_p = 4.1813$ kJ/kg·K), and $f = (0.79 \ln R_e - 1.64)^{-2}$. Equation (4.5) is valid in the transitional flow condition, which is characterized by a Reynolds number $R_e = \dot{V}_{water} D_h/A\nu$ in the interval $3 \times 10^3 < R_e < 10^6$, where $\nu = \upsilon/\rho$ is the kinematic viscosity and ρ is the water density. For the cavity cooling channel with dimensions $w = 3.6$ mm and $h = 8.9$ mm, the heat transfer coefficient and Reynolds number as a function of the water temperature T_{water} are plotted in Fig. 4-12. The variation of h_c and R_e with T_{water} mainly arises from the temperature dependence of the water viscosity.

With the information of the ohmic loss and h_c, the temperature rise in the gy-

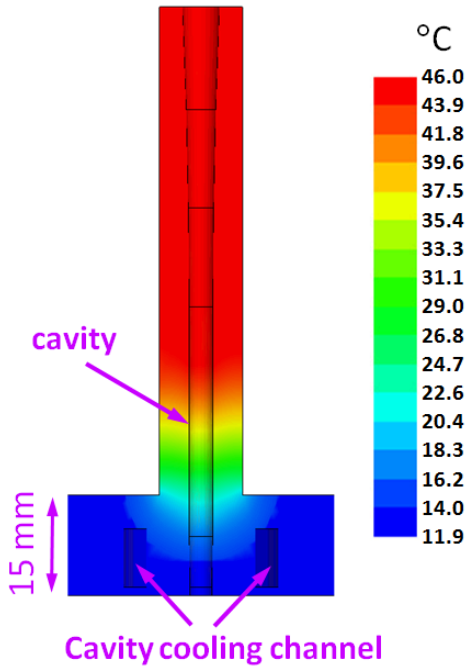

Figure 4-13: Temperature rise in the gyrotron cavity for an uniformly distributed $P_{load} = 100$ W and heat transfer coefficient $h_c = 5$ kW/m^2/℃ in the cavity cooling channel.

rotron cavity could be estimated using the thermal/stress solver ePhysics [132]. The simulation result is shown in Fig. 4-13 considering an ohmic loss $P_{load} = 100$ W uniformly distributed on the cavity straight section and a convective heat transfer coefficient of $h_c = 5$ kW/m^2/℃ for forced water in the cavity cooling channel. The temperature gradient along the gyrotron cavity as a result of the ohmic loss and the cooling circuit configuration may be responsible for the gyrotron frequency detuning as discussed in Section 4.3.2.

4.3.4 CW Long-Run Operation

Stable gyrotron operation over extended periods without interruption is an important requirement to allow long-term signal averaging in DNP/NMR experiments. The stability of the 330-GHz gyrotron was evaluated during a 110-h continuous run test and the result is shown in Fig. 4-14. In this test, the output power was kept stable using a proportional, integral, and derivative (PID) control system implemented in

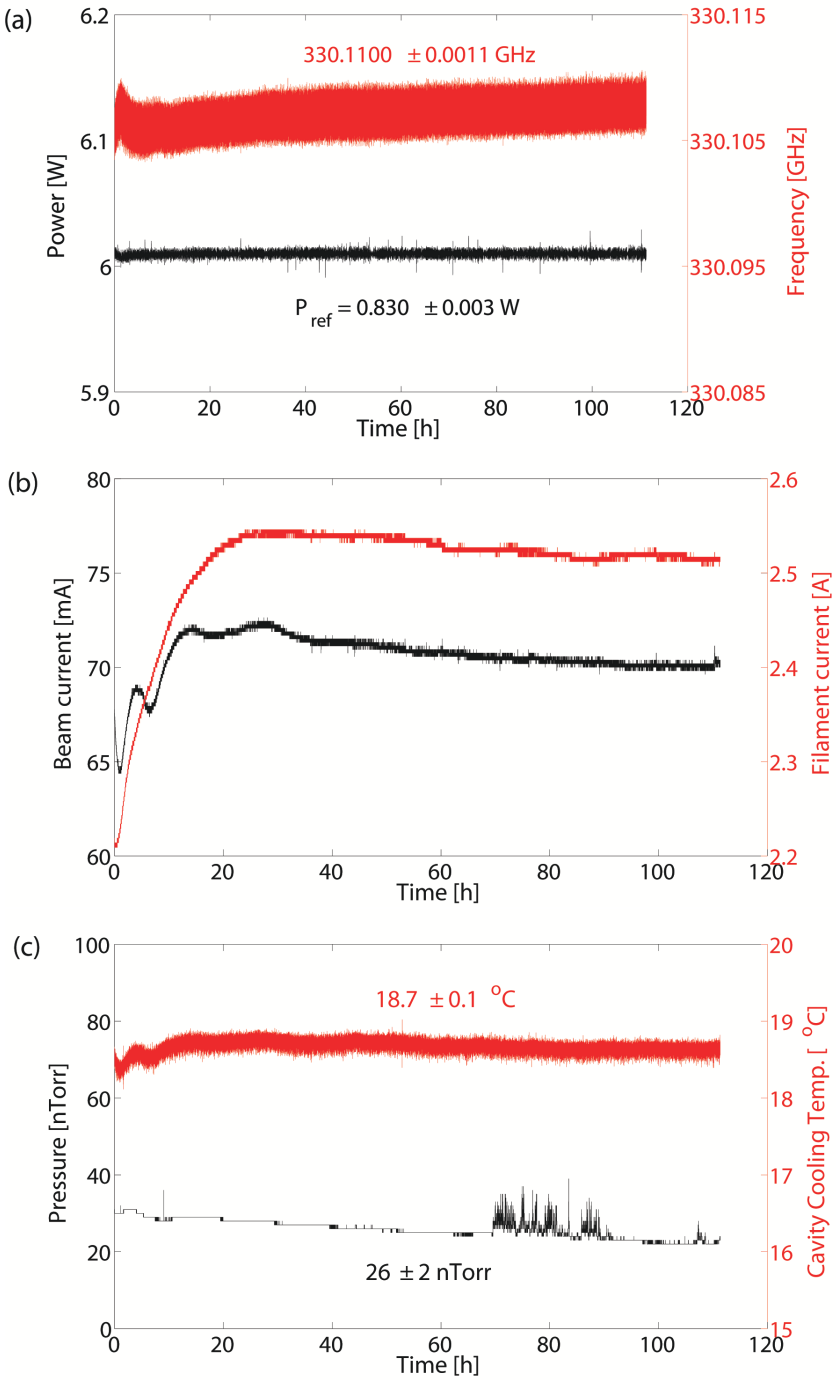

Figure 4-14: Monitored variables during the CW long-run stability test of the 330-GHz second-harmonic gyrotron: (a) output power and frequency, (b) beam and cathode filament currents, and (c) pressure and cavity cooling temperature. During the test, the magnetic field was persistent at $B_0 = 6.006$ T and the beam voltage was kept at $V_b = 10.0$ kV.

LabVIEW by adjusting the cathode filament current based on the difference between a set point value and the output power sampled by a Scientech calorimeter head, model AC2500 (serial nº 4178), connected to a Scientech digital reader, model Vector S310. During the stability test, the output reference power and frequency were kept stable within ±0.4% (±3 mW) and ±3 ppm (±1.1 MHz), meeting the requirement for DNP/NMR, and the superconducting magnet was in persistent mode at $B_0 = 6.006$ T.

4.3.5 Output Beam Pattern

The output microwave beam pattern was evaluated in the 330-GHz gyrotron using the techniques outlined in Section 4.2.4. A picture of the fabricated mode converter is seen in Fig. 4-15. In low power operation ($P_{OUT} = 0.4$ W), the image of the microwave beam in Fig. 4-16 was taken using the pyroelectric camera right after the end of the corrugated waveguide connected to the gyrotron window. Using Eq. (3.19), the Gaussian-like content associated with the measured pattern was calculated to be 92% with beam radii $w_x = 5.1$ mm and $w_y = 4.0$ mm.

In high power operation ($P_{OUT} = 8.1$ W), the output microwave beam pattern shown in Fig. 4-17 could be visualized using a thermal-sensitive phosphor plate illuminated with an ultraviolet light. Due to physical and electromagnetic reasons, the aforementioned methods could not be used to evaluate the microwave beam inside

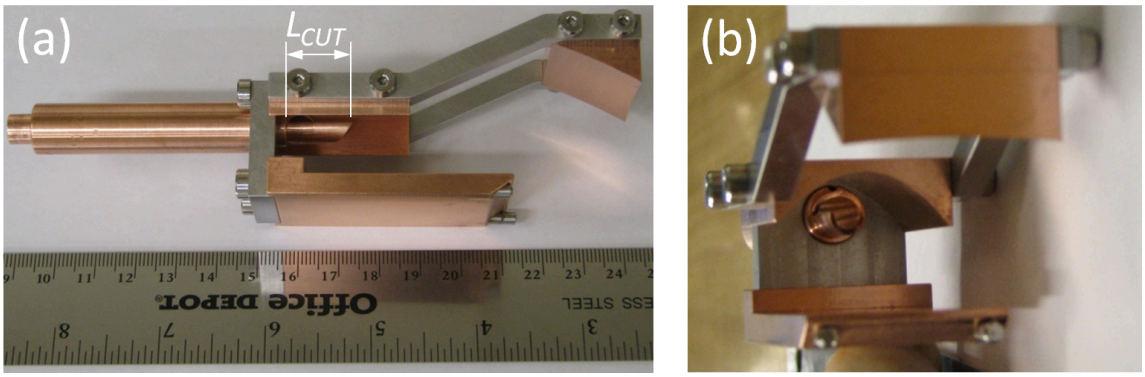

Figure 4-15: (a) Side view and (b) front view of the fabricated quasi-optical mode converter with a helical launcher.

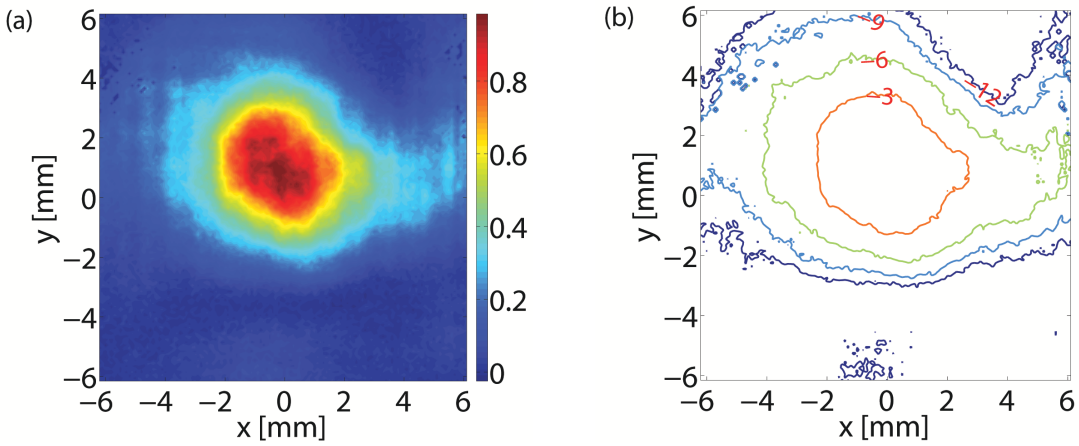

Figure 4-16: Gyrotron output microwave beam displayed in (a) normalized linear power scale and (b) dB contours. The pyroelectric camera image of the output $TE_{-4,3}$ mode at 330.17 GHz was taken right after the end of the corrugated waveguide. Additional gyrotron parameters: beam voltage $V_b = 9.6$ kV, beam current $I_b = 32$ mA, and output power $P_{OUT} = 0.4$ W.

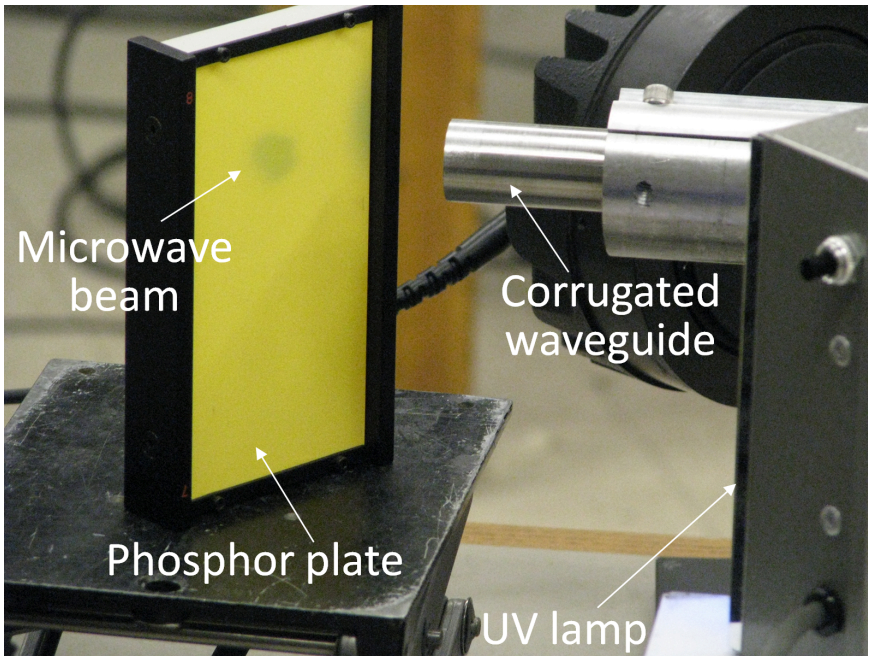

Figure 4-17: Gyrotron output microwave beam displayed on a thermal-sensitive phosphor plate illuminated by an ultraviolet light. Gyrotron parameters: beam voltage $V_b = 10.1$ kV, beam current $I_b = 130$ mA, frequency $f = 329.34$ GHz, and output power $P_{OUT} = 8.1$ W.

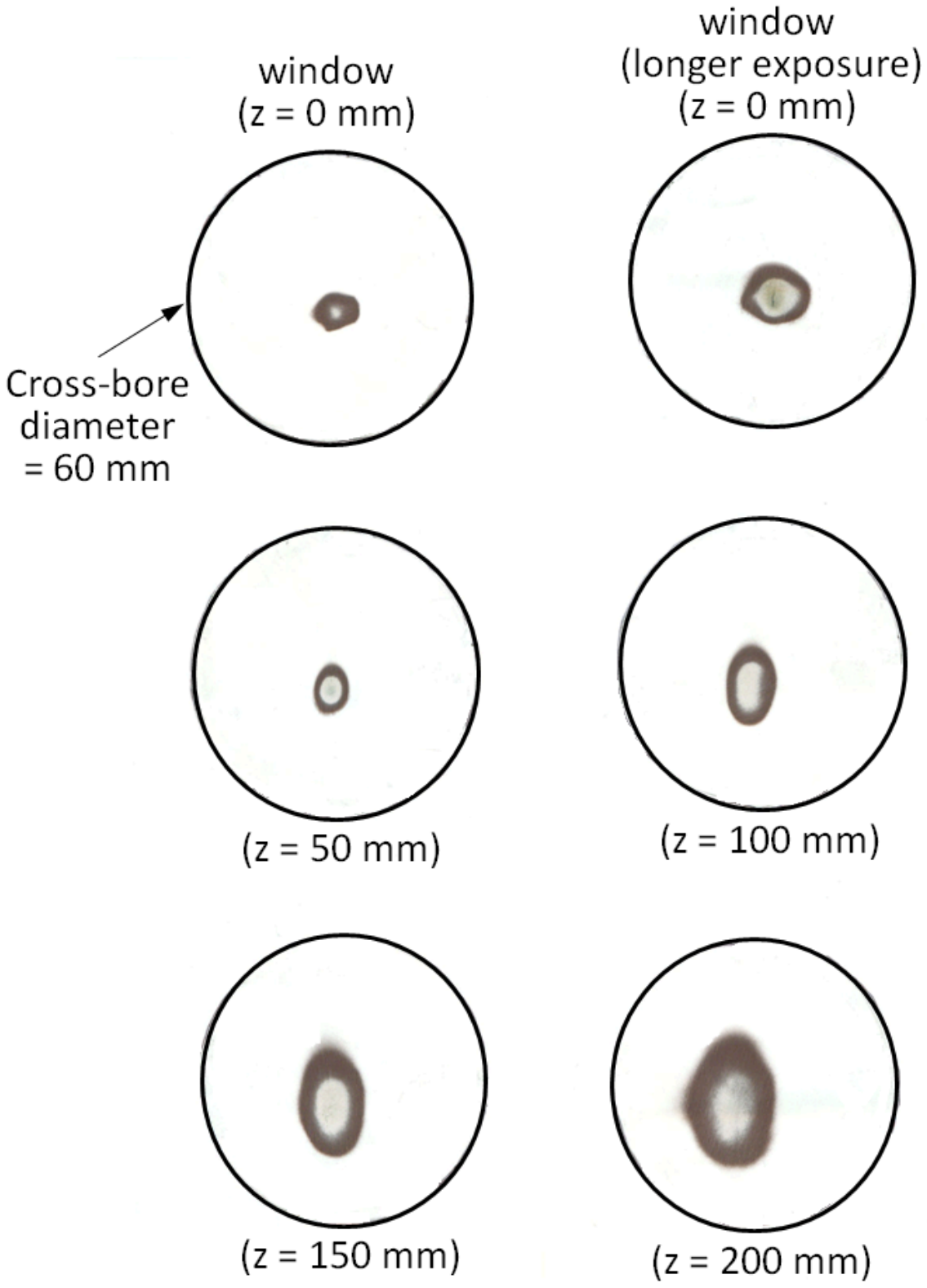

Figure 4-18: Thermal paper images of the gyrotron output microwave beam at different distances z from the window location ($z = 0$ mm). Gyrotron parameters: beam voltage $V_b = 9.7$ kV, beam current $I_b = 75$ mA, frequency $f = 330.12$ GHz, and output power $P_{OUT} = 6.2$ W.

the cross-bore of the superconducting magnetic after the gyrotron window. For this task, thermal paper was utilized to record the microwave beam at different distances z from the window location ($z = 0$ mm). The result of this measurement is shown in Fig. 4-18, depicting the propagation of a Gaussian-like beam along the magnet cross-bore. Based on these experimental results, proper operation of the implemented internal quasi-optical mode converter could be verified.

4.3.6 Short Pulse Measurement

All measurements reported so far were carried out in CW operation. In order to assess the gyrotron performance at a beam current higher than the 200 mA limit imposed by the CW high-voltage power supply, a high voltage modulator described in Section 3.5.3 was utilized. Typical oscilloscope traces for beam voltage V_b, beam current I_b, body current I_{body}, and output power monitored by a diode are shown in Fig. 4-19. Magnetic tuning experimental results are plotted in Fig. 4-20 for peak beam voltage $V_b = 10.9$ kV, beam current $I_b \sim 610$ mA, pulse repetition frequency $PRF = 20$ Hz, and water temperature $T_{water} = 15$℃. The measured frequencies in pulse operation are consistent with the ones obtained in the start current measurement at low equilibrium power points due to the absence of cavity deformation. The average power in pulse regime is on the order of a few milliwatts. One complication during pulse measurements is that a mode can be excited in the rising or falling edge of the voltage pulse at a lower value than the voltage peak. For example, the gyrotron mode at 330 GHz could be excited at each magnetic field value in Fig. 4-20 with a proper gun coil field.

Thermal tuning measurements were also carried out for a fixed electron cyclotron frequency ($V_b = 10.9$ kV peak, $B_0 = 6.007$ T) and beam current $I_b \sim 620$ mA and the result is shown in Fig. 4-21. The thermal tuning rate obtained in the experiment was 4.8 MHz/℃, compatible to the theoretical 5.6 MHz/℃ in an unconstrained gyrotron cavity. The combination of magnetic, voltage, and thermal tuning yielded a total tuning range of 1.2 GHz in pulse operation with minimum peak output power of 20 W.

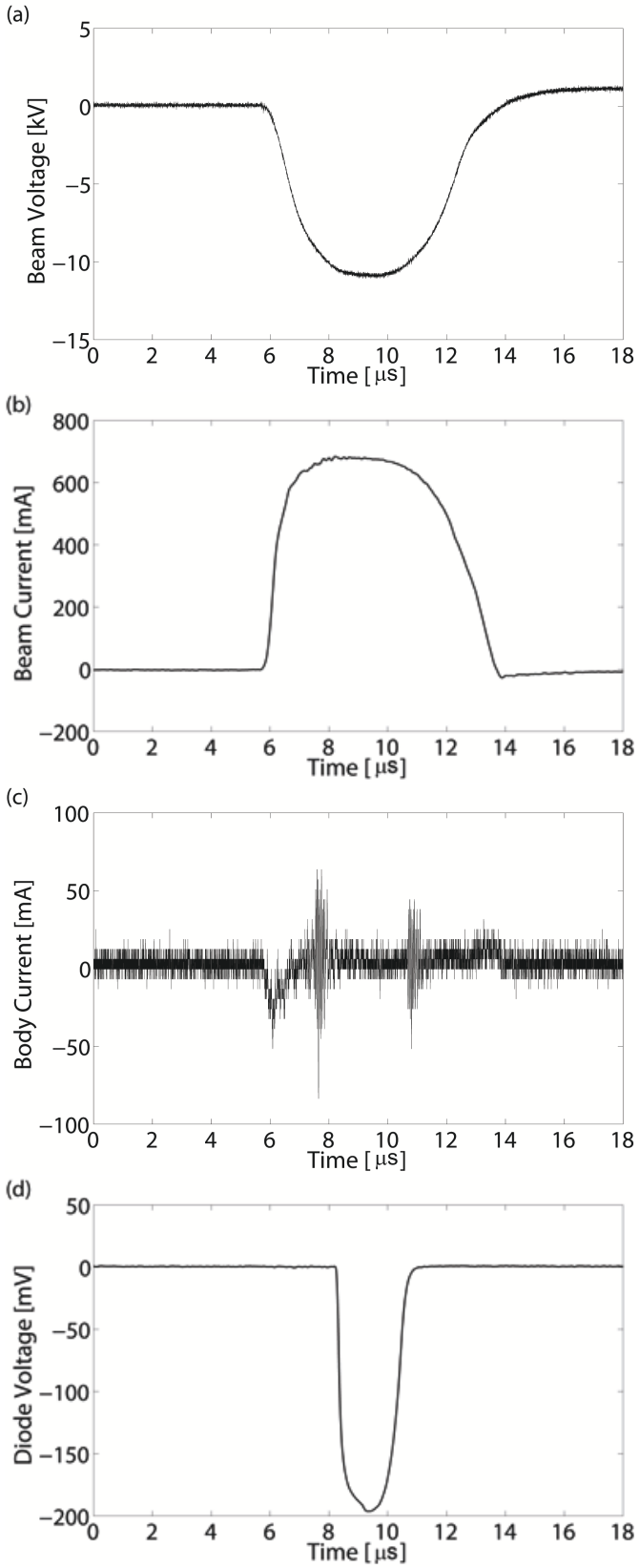

Figure 4-19: Typical traces obtained from high voltage modulator: (a) beam voltage, (b) beam current, (c) body current, and (d) output power detected by a diode.

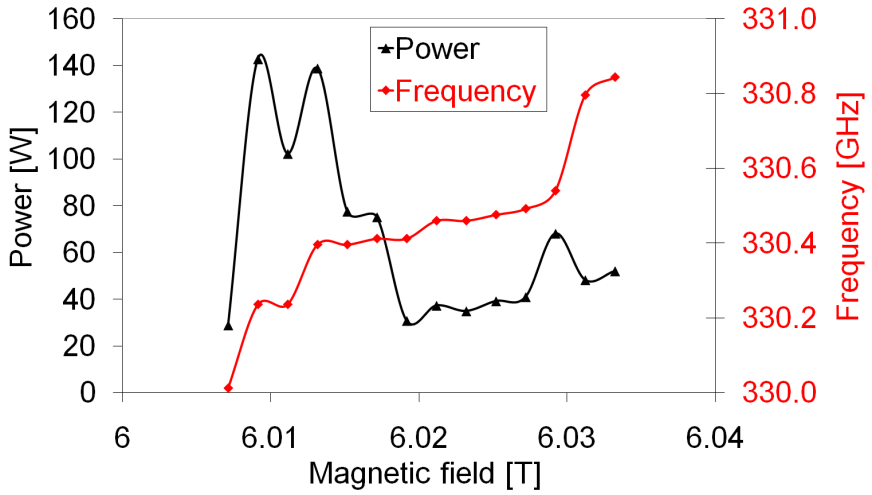

Figure 4-20: Magnetic tuning measurement for peak beam voltage $V_b = 10.9$ kV, beam current $I_b \sim 610$ mA, $PRF = 20$ Hz, and water temperature $T_{water} = 15$℃ in the cavity cooling channel.

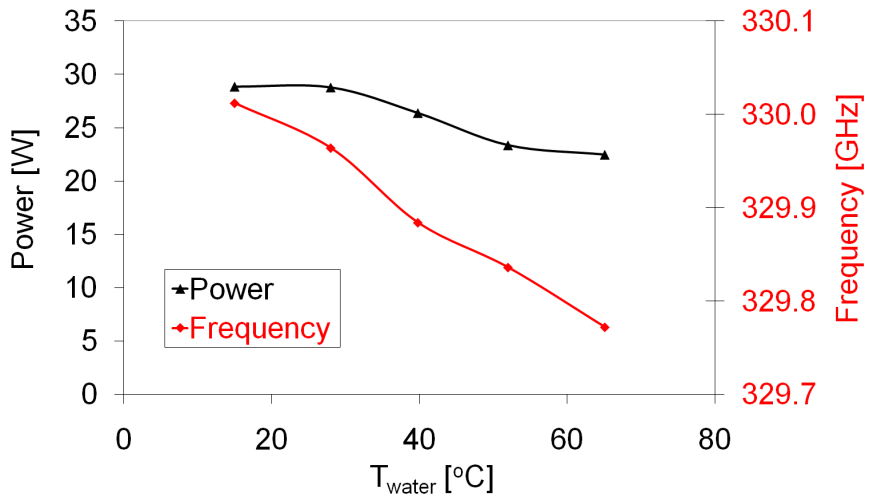

Figure 4-21: Thermal tuning measurement for magnetic field $B_0 = 6.007$ T, peak beam voltage $V_b = 10.9$ kV, and beam current $I_b \sim 620$ mA, $PRF = 20$ Hz.

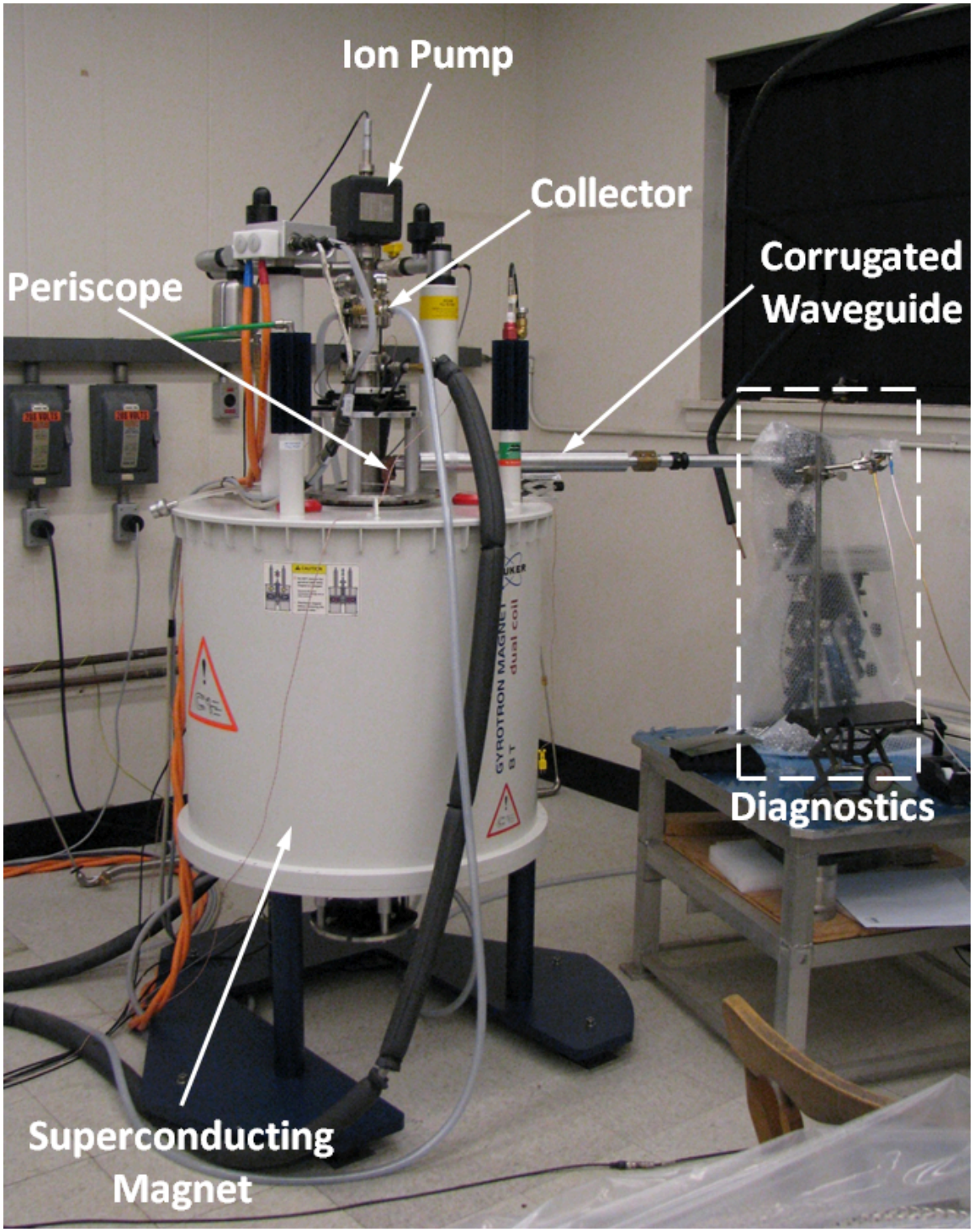

Figure 4-22: Photograph of the 330-GHz gyrotron installed in the Bruker superconducting magnet.

4.4 Experimental Results (Bruker Magnet)

After the evaluation of the 330-GHz gyrotron using the Cryomagnetics magnet, the gyrotron was moved to its final destination, the Bruker superconducting magnet detailed in Section 3.5.1. A schematic of the 330-GHz gyrotron in the Bruker superconducting magnet is shown in Fig. 4-22, where the output power is extracted using a periscope attached to the gyrotron window.

4.4.1 Start Oscillation Current

The start oscillation current of the 330-GHz gyrotron in the new magnet system was measured in CW operation as a function of magnetic field for $B_{gun} = 25$ mT and a beam voltage $V_b = 10.1$ kV, the same voltage utilized in the start current measurement reported in Section 4.3.1. The start current data is shown in Fig. 4-23, where the measured start current values are in good agreement with the calculated start current from linear theory for $TE_{-4,3,q}$ modes, $q = 1$ to $q = 6$. The calculation in Fig. 4-23 was performed using the same beam parameters as utilized in Fig. 4-6. The measured frequency at each start current value is in reasonable agreement with the cold frequencies associated with high-order axial modes, $q = 1$ to $q = 6$, presented in Table 3.2. Frequency detuning is observed for $B_0 < 6.0$ T since the output power at these start current values exceed 1 W. The fundamental mode $TE_{5,1}$ is excited at $B_0 = 6.028$ T with a start current of 80 mA and measured frequency of 166.62 GHz.

The experimental result in the Bruker magnet is similar to the one obtained in the Cryomagnetics magnet, although the operating mode is excited at lower currents in the Bruker magnet with a minimum measured start current of 21 mA. Differences in the magnetic field profile such as a longer flattop region in the Bruker magnet may explain the lower start current. Furthermore, the operating mode is observed at slight lower magnetic fields in the new magnet system. This difference may be caused by the position of the tube with respect to the magnet axis and/or by an inaccuracy in the field-to-current ratio provided by the vendor. According to Bruker, the field-to-current ratio for the cavity coil is 0.06565 T/A and the calibration of the

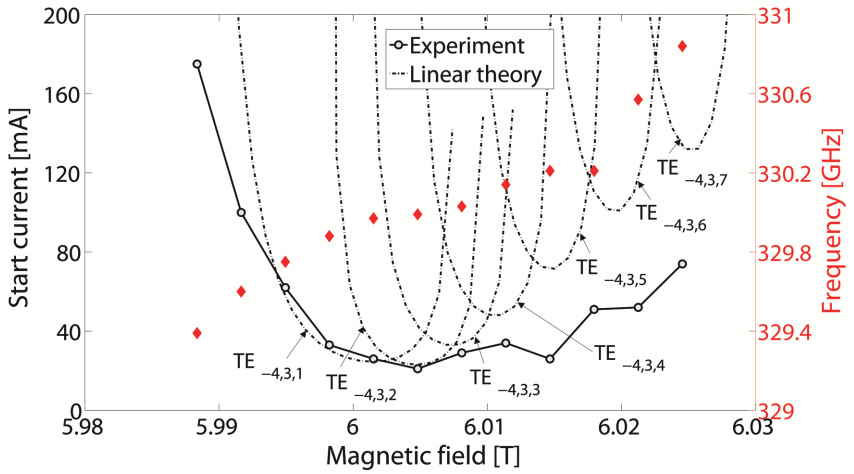

Figure 4-23: Measured start oscillation current (black solid line) and measured frequency (red diamonds) of the operating mode $TE_{-4,3}$ as a function of magnetic field for beam voltage $V_b = 10.1$ kV, $T_{water} = 15$ ℃. Theoretical start currents (black dash-dotted lines) based on linear theory for the first six axial modes $TE_{-4,3,q}$, where $q = 1, 2, 3, 4, 5, 6$ (simulation parameters: cold-cavity axial field profile, $V_b = 10.1$ kV, $\alpha = 1.8$, no beam velocity spread).

magnet power supply has an accuracy of 0.2%.

4.4.2 Power and Frequency Tuning

Power and frequency tuning were evaluated as a function of beam voltage for a constant magnetic field as indicated in Fig. 4-24. Magnetic tuning measurement was also carried out for two different beam voltages, $V_b = 9$ kV and $V_b = 12.9$ kV, as shown in Fig. 4-25 since the fundamental mode $TE_{5,1}$ would be excited for $B_0 > 6.02$ T for $V_b = 12.9$ kV. For a beam current $I_b = 190$ mA, while the power varies from 1 W to 19 W, compared to 2 W to 18 W in the Cryomagnetics case, the frequency continuously varies from 328.82 GHz to 330.05 GHz, compared 328.96 GHz to 329.93 GHz in the Cryomagnetics case. Superposition of the magnetic and voltage tuning data having the normalized electron cyclotron frequency as an abscissa in Fig. 4-26 indicates the common nature of the tuning mechanism based on the cyclotron frequency. Thermal tuning measurements were also performed as displayed in Fig. 4-27, where the expected shift in the power and frequency curves were observed for operation at a higher cavity temperature. In this measurement, high pressure in the tube did not

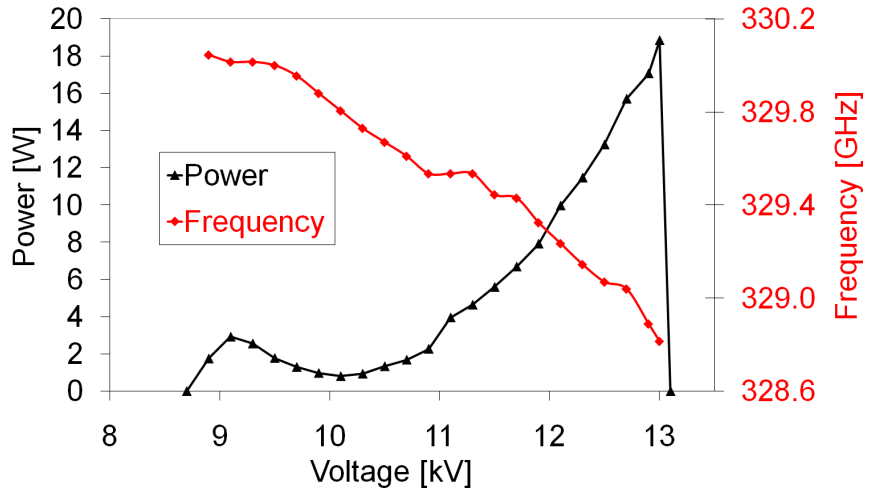

Figure 4-24: Power (black line) and frequency tuning (red line) measurement as a function of beam voltage for magnetic field $B_0 = 5.991$ T, beam current $I_b = 190$ mA, and water temperature in the cavity cooling channel $T_{water} = 15$℃. The gun coil was swept from $B_{gun} = 58$ mT to $B_{gun} = 13$ mT for best output power as the beam voltage was decreased.

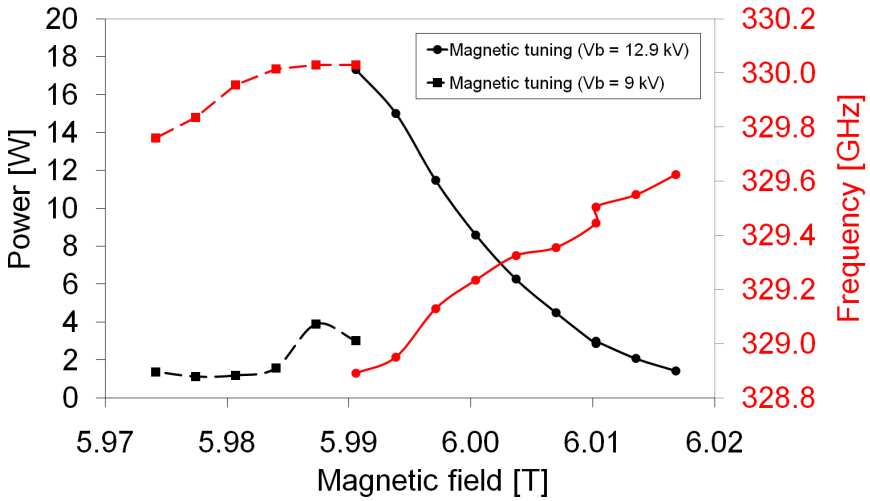

Figure 4-25: Power (black line) and frequency tuning (red line) measurement as a function of magnetic field for beam voltage $V_b = 9$ kV (square markers, dashed line) and $V_b = 12.9$ kV (circular markers, solid line). The water temperature in the cavity cooling channel was $T_{water} = 15$℃. The gun coil field was kept constant at $B_{gun} = 16$ mT and $B_{gun} = 58$ mT during the measurements at $V_b = 9$ kV and $V_b = 12.9$ kV, respectively.

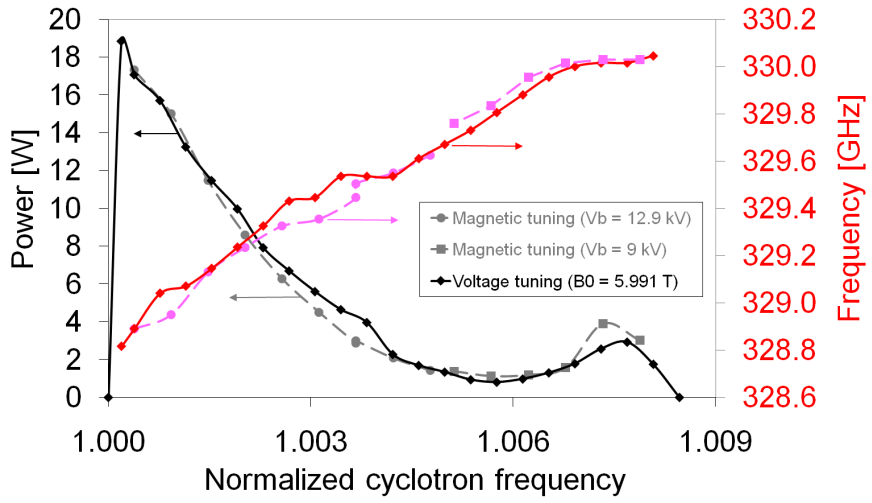

Figure 4-26: Magnetic tuning (dashed line) and voltage tuning (solid line) measurement for beam current $I_b = 190$ mA and water temperature in the cavity cooling channel $T_{water} = 15$℃. The voltage tuning data was taken at $B_0 = 5.991$ T and the magnetic tuning data was taken at $V_b = 9$ kV (square markers, $B_{gun} = 16$ mT) and at $V_b = 12.9$ kV (circular markers, $B_{gun} = 58$ mT).

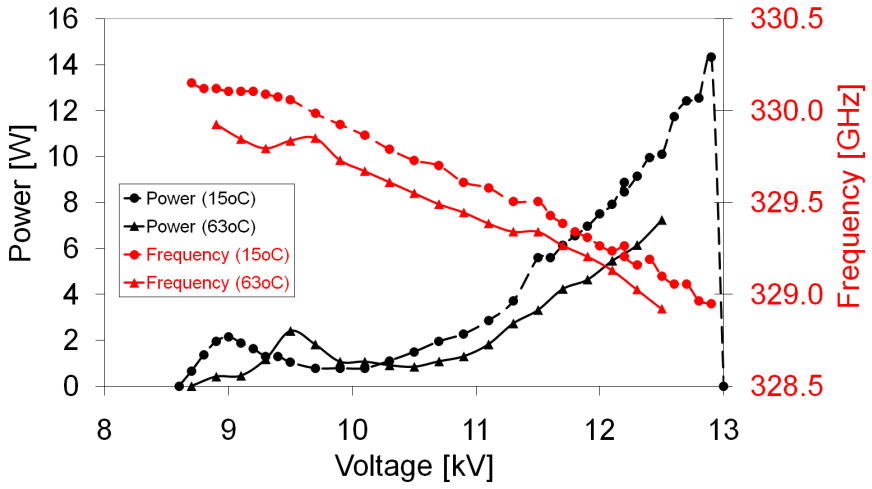

Figure 4-27: Voltage tuning measurement for magnetic field $B_0 = 5.991$ T, beam current $I_b = 150$ mA, along with cavity cooling channel temperature $T_{water} = 15$℃ (circular markers), and $T_{water} = 63$℃ (triangular markers).

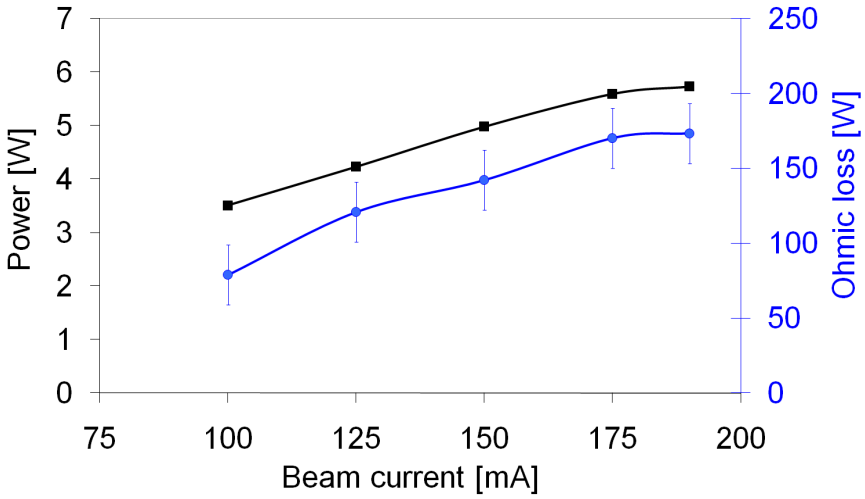

Figure 4-28: Output power and associated ohmic loss as a function of beam current for beam voltage $V_b = 11.7$ kV, magnetic field $B_0 = 5.991$ T, and water flow rate $\dot{V}_{water} = 0.71$ gpm.

allow operation for $V_b > 12.5$ kV.

4.4.3 Additional measurements

In addition to the start oscillation current as well as the power and frequency tuning, the ohmic loss and the output beam pattern have also been evaluated in the current system using the techniques described in Section 4.2. The ohmic loss was estimated as a function of beam current for $V_b = 11.7$ kV, $B_0 = 5.991$ T, and flow rate $\dot{V}_{water} = 0.71$ gpm. The result is shown in Fig. 4-28 with an estimated extraction efficiency η_{RF} of 3.2% for a beam current $I_b = 175$ mA, which is on the order of the extraction efficiency reported in Section 4.3.3.

A picture of the output microwave beam was taken 80 mm after the end of a corrugated waveguide connected to the output periscope using a Spiricon Pyrocam III pyroelectric camera. The Gaussian-like content associated with the measured pattern in Fig. 4-29 was computed to be 91% with beam radii $w_x = 4.6$ mm and $w_y = 5.4$ mm.

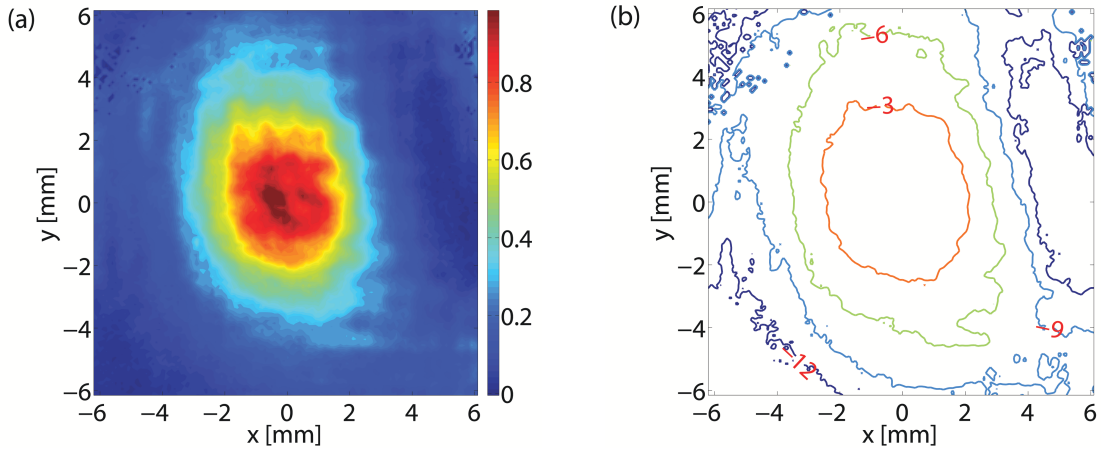

Figure 4-29: Gyrotron output microwave beam displayed in (a) normalized linear power scale and (b) dB contours. The pyroelectric camera image of the output $TE_{-4,3}$ mode at 329.82 GHz was taken 80 mm after the end of the corrugated waveguide. Additional gyrotron parameters: beam voltage $V_b = 10.74$ kV, beam current $I_b = 75$ mA, $B_{gun} = 36$ mT, and output power $P_{OUT} = 1$ W.

4.5 Discussion

The operation of a continuously tunable 330-GHz second-harmonic gyrotron has been successfully demonstrated as reported in this chapter. In the first configuration of the gyrotron utilizing a superconducting magnet manufactured by Cryomagnetics, the gyrotron has generated 18 W of output power for a 10.1-kV 190-mA electron beam, yielding an efficiency of 0.93%. The minimum starting current of the operating mode $TE_{-4,3}$ was measured to be 33 mA for a beam voltage $V_b = 10.1$ kV. Good agreement was observed between the measured start current values and the prediction from linear theory for the first six axial modes ($q = 1$ to $q = 6$). Also the measured frequency at each start current value with a low equilibrium power value reasonably agrees with the cold-cavity frequency of each axial mode.

Continuous frequency tunability of 1.2 GHz with a minimum output power of 2 W was achieved via cyclotron frequency tuning and cavity thermal tuning. This tuning range is 24 times broader than the state-of-the-art for second-harmonic modes in submillimeter-wave gyrotrons at the beginning of this project. Moreover, the measured frequency tuning range covers the optimum frequency (329.4 GHz) that

yields the maximum DNP/NMR signal enhancement. A frequency-tunable gyrotron is highly desirable since it simplifies the implementation of DNP in NMR spectrometers, particularly the ones without magnetic tuning capability.

The long-term stability of the 330-GHz gyrotron output was evaluated over an uninterrupted period of 110 h where the output power of the gyrotron was monitored by a computerized PID control. During this test, the power and frequency were stable within $\pm 0.4\%$ and ± 1.1 MHz, respectively, meeting the specifications for long-term signal averaging in DNP/NMR experiments. In addition, proper operation of the implemented quasi-optical mode converter has been verified as a Gaussian-like output microwave beam has been recorded by various methods. The Gaussian-like content associated with the image taken by a pyroelectric camera right after the end of the output corrugated waveguide was computed to be 92%. One challenge for submillimeter-wave operation in the current gyrotron circuit is the predominance of ohmic loss over diffractive loss. As a consequence, the majority of the power transferred from the electron beam is dissipated on the cavity walls, leading to low extraction efficiency and frequency detuning in CW operation as observed.

Besides these results in CW operation, measurements were also performed in short pulse operation at a higher beam current ($I_b \sim 610$ mA), where tunability of 1.2 GHz with a minimum output power of 20 W has been achieved by means of cyclotron frequency tuning and thermal tuning. The measured frequencies in pulse operation are consistent with the ones obtained in the start current measurement at low equilibrium power points due to the absence of cavity deformation.

After the evaluation of the gyrotron in the Cryomagnetics magnet, the performance of the oscillator was assessed in the Bruker superconducting magnet ordered for the 330-GHz gyrotron. The experimental results in the new magnet system are consistent with the ones obtained in the Cryomagnetics magnet for power and frequency tuning, start oscillation current, and ohmic loss. Magnetic and voltage tuning measurements for beam current $I_b = 190$ mA demonstrated an output power of 1-19 W (CW) in the frequency range of 328.82 GHz to 330.05 GHz. The desired power level of 5 W for DNP/NMR experiments is achieved for the frequency band 328.82-329.54

Table 4.1: Comparison between specifications and experimental results obtained in the 330-GHz gyrotron.

	Specification	Measured
Optimum DNP frequency	329.4 GHz	Covered (7 W of power)
Tuning range	1.5 GHz	1.2 GHz
Output power	> 5 W	> 1 W (> 5 W over 700 MHz)
Power stability	$\approx 1\%$	0.4%
Frequency stability	≈ 1 MHz	1.1 MHz
Output beam pattern	Gaussian-like	Gaussian-like

GHz, corresponding to a tuning range of 720 MHz. The minimum start current was measured to be 21 mA for the operating mode $TE_{-4,3}$, where good agreement was verified between the measured start current values and the calculation from linear theory for the first six axial modes ($q = 1$ to $q = 6$). Furthermore, the measured frequency at each start current value with a low equilibrium power value reasonably agrees with the cold-cavity frequency of each axial mode. Evaluation of the image of the output microwave beam taken with a pyroelectric camera after the corrugated waveguide revealed a Gaussian-like content of 91%. A comparison between the requirements and the experimental results obtained in the 330-GHz gyrotron is given in Table 4.1.

Chapter 5

Design and Operation of a Tunable 460-GHz Second-Harmonic Gyrotron

In this chapter, the design and operational characteristics of a second-harmonic 460-GHz CW gyrotron are presented. The gyrotron is intended to be used as a submillimeter-wave source for 700-MHz DNP/NMR experiments. The tube was redesigned and rebuilt from a previous version [91] for higher output power, lower start current, and improved stability/reliability. Broadband smooth frequency tunability was also obtained for the operating second-harmonic mode by changing the electron cyclotron frequency. This chapter is organized as follows: Section 5.1 describes the design and features of the different parts of the tube, including electron gun, cavity interaction region, and internal converter from a cylindrical waveguide mode to a linearly polarized free space Gaussian-like beam. Evaluation of output power and frequency tunability as a function of magnetic field and beam voltage, start oscillation current of the operating mode, ohmic loss, frequency and power stability in long-run continuous operation, and output microwave beam profile are detailed in Section 5.2. In addition to the experimental results reported in the previous section at 460 GHz, power and broadband frequency tunability was also achieved at 332 GHz as described in Section 5.3, providing valuable information for the design of the subsequent 330-

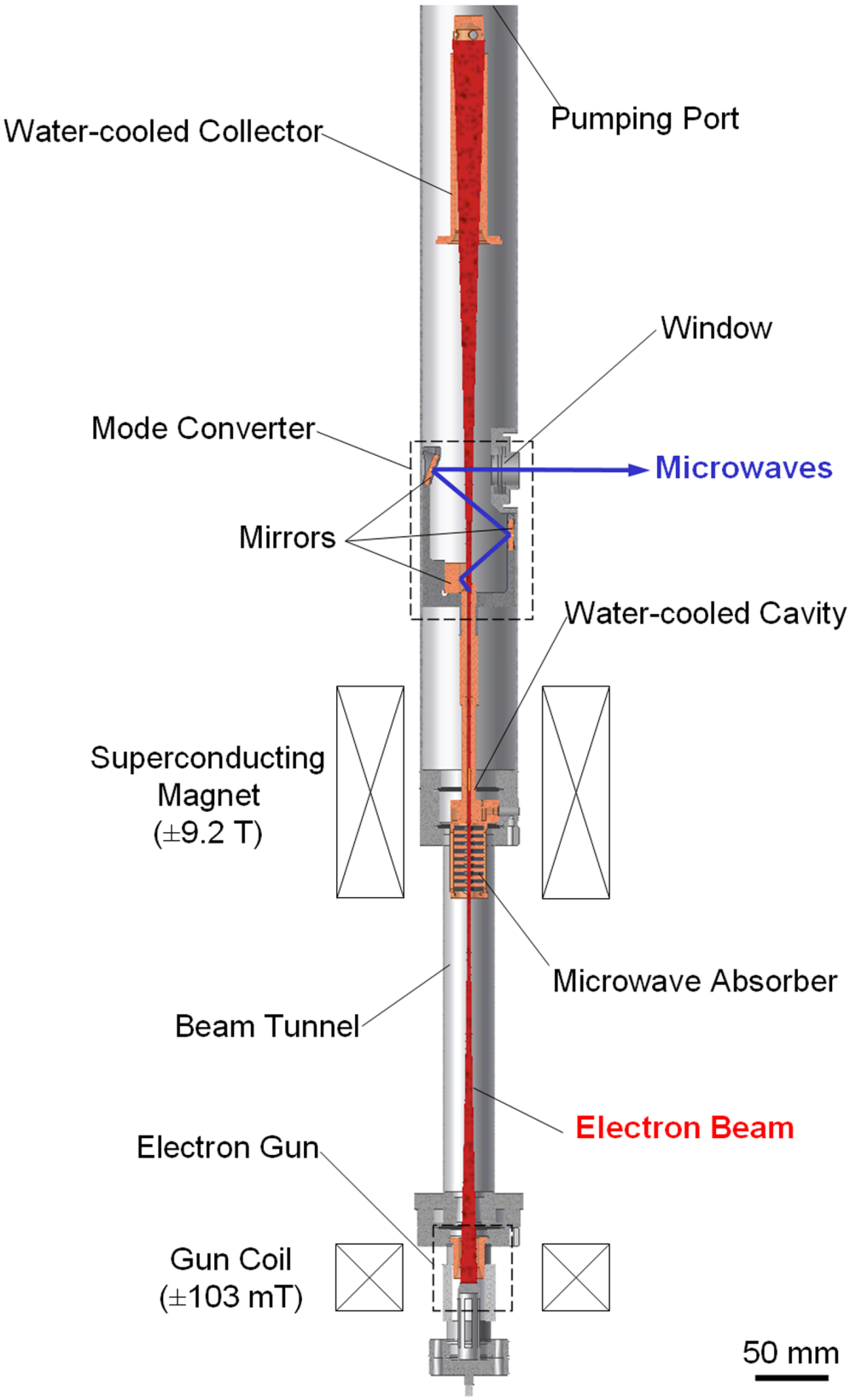

Figure 5-1: Schematic of the 460-GHz gyrotron.

GHz tunable gyrotron described in the previous chapters. The current chapter is finalized with conclusions in Section 5.4. The results reported in this chapter at 460 GHz are available in the literature [101].

5.1 Design

A schematic of the upgraded 460-GHz second-harmonic gyrotron is shown in Fig. 5-1, which depicts the different parts of the tube: electron gun, cavity interaction region, internal mode converter, and collector. This gyrotron utilizes a superconducting magnet fabricated by Cryomagnetics, Inc., which is described in Section 3.5.1 and Ref. [125].

5.1.1 Diode Electron Gun

The magnetron injection gun utilized in the 460-GHz gyrotron is identical to the one described in Section 3.5.2. After being thermionically emitted from an indirectly heated ring cathode of radius 5.38 mm and slant length 1.09 mm, electrons are accelerated due to a potential difference between a grounded anode and a cathode at a beam voltage $-V_b$. As the electrons advance through the beam tunnel in cyclotron motion around the magnetic field lines created by the main superconducting magnet, the hollow annular electron beam is compressed, reaching a final beam radius of $r_e = 1.1$ mm in the cavity interaction region. The electron gun geometry is depicted in Fig. 5-2(a) along with equipotential lines, and electron trajectories obtained from the code EGUN [127] for the gyrotron operating parameters $V_b = 13$ kV and beam current $I_b = 100$ mA. Other important beam parameters such as the pitch factor α and the beam perpendicular velocity spread $\Delta v_\perp / v_\perp$ were also evaluated at the cavity region using EGUN. The results from these simulations are shown in Fig. 5-2(b) and a set of values favorable for beam-wave interaction, i.e. a high pitch factor ($\alpha \cong 2.0$) and a low perpendicular velocity spread ($\Delta v_\perp / v_\perp < 4\%$), was obtained at the operating voltage $V_b = 13$ kV by proper adjustment of a water-cooled copper gun coil with a magnetic field range of ± 103 mT.

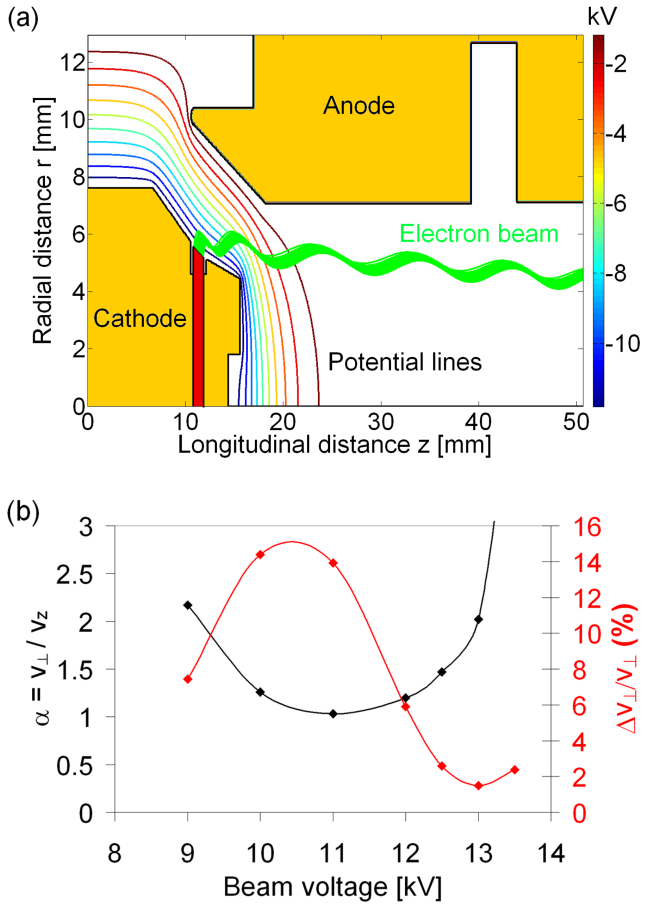

Figure 5-2: (a) Magnetron injection gun geometry along with simulated electron trajectories and equipotential lines for an applied voltage $V_b = 13$ kV and beam current $I_b = 100$ mA. (b) Computed pitch factor α and beam perpendicular velocity spread $\Delta v_\perp / v_\perp$ at the cavity entrance according to the code EGUN. The gun coil field was adjusted to a subtracting field of -61 mT for high α and low velocity spread at the operating voltage of 13 kV.

5.1.2 Interaction Circuit

As outlined in Section 3.2, although operation at the second harmonic of the cyclotron frequency has the advantage of requiring only half of the magnetic field necessary for a fundamental-harmonic mode, second-harmonic modes suffer from lower beam-wave interaction efficiency and from additional competition with neighboring fundamental modes. In order to overcome these difficulties, the mode $TE_{11,2}$ was chosen as the operating mode due to its isolation from surrounding modes and its high coupling to an electron beam of radius $r_e = 1.1$ mm. This whispering-gallery mode is supported by a

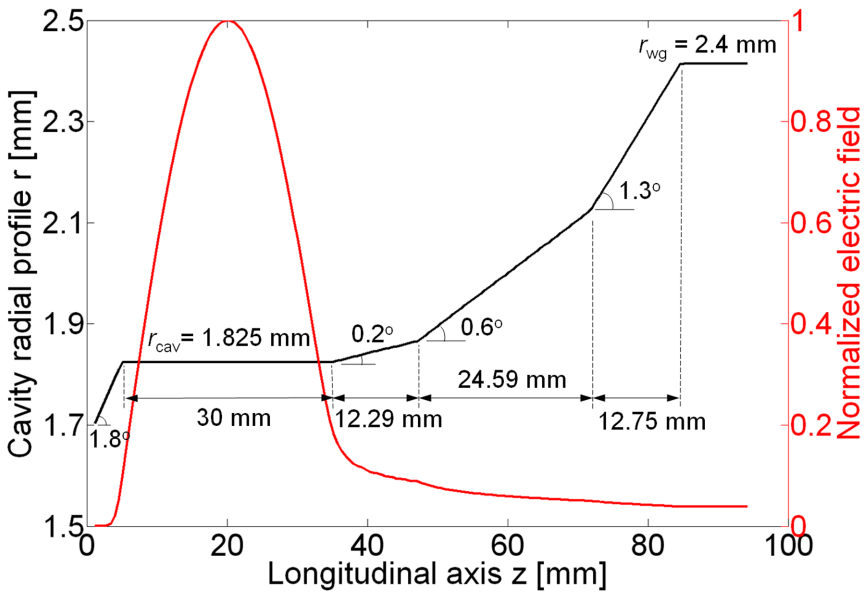

Figure 5-3: Schematic of the 460-GHz gyrotron circuit featuring a downtaper section, a cavity (straight section), and an uptapered section. The red line represents the normalized axial electric field profile of the operating mode $TE_{11,2,1}$.

30-mm long cavity with radius $r_{cav} = 1.825$ mm, where a long cavity ($L \sim 46\lambda$ at 460 GHz) was preferred in order to reduce the start oscillation current. The interaction circuit geometry comprising a cavity straight section and tapered sections is shown in Fig. 5-3. The uptapered section was designed for reduced mode conversion and for reduced wave reflection at the cavity uptapered end to improve power extraction at the high operating frequency of the tube. The mode conversion in the uptapered part was found to be less than 0.2% according to calculations using the scattering matrix code Cascade [116]. Also shown in Fig. 5-3 is the normalized axial electric field profile of the first axial mode $TE_{11,2,1}$ obtained from the cold-cavity code [111].

For the different axial modes $TE_{11,2,q}$, the ohmic quality factor was computed to be $Q_O = 8100$ for an electrical conductivity half that of ideal copper (5.8×10^7 S/m), and the diffractive quality factor was estimated as $Q_{D,q} = 90500/q^2$ according to results from the cold-cavity code. Based on linear theory [114] and the cold cavity axial electric field profile, the start current of the $TE_{11,2,1}$ mode was computed to be 27 mA for beam parameters $V_b = 12.8$ kV, $\alpha = 1.85$, $r_e = 1.1$ mm, and no velocity spread. Following similar procedure, the start current of the neighboring modes was

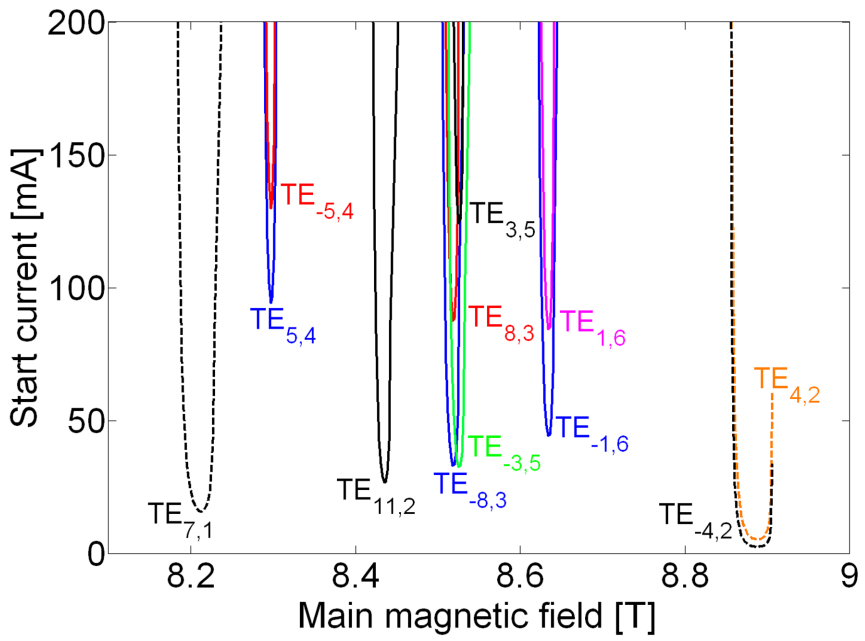

Figure 5-4: Start oscillation current of cavity $TE_{m,n,1}$ modes in the vicinity of the operating mode $TE_{11,2,1}$. The dashed lines represent fundamental-harmonic modes, while the solid ones refer to second-harmonic modes. For each $TE_{m,p,q}$ mode, only the lowest axial mode ($q = 1$) is shown (beam parameters: $V_b = 12.8$ kV, $r_e = 1.1$ mm, $\alpha = 1.85$, and no velocity spread).

also evaluated and the result is shown in Fig. 5-4, which demonstrates the isolation of the operating second-harmonic mode from adjacent modes, especially fundamental modes.

The performance of the interaction circuit was evaluated using the self-consistent code MAGY [115] and the simulation results are shown in Fig. 5-5 for beam parameters $V_b = 13$ kV, $I_b = 100$ mA, $\alpha = 1.9$, $r_e = 1.1$ mm, and perpendicular velocity spread of 5%. A magnetic tuning range of 540 MHz was obtained supported by the excitation of successive axial modes $TE_{11,2,q}$, $q = 1, 2, 3, 4$. The transition from the mode $TE_{11,2,1}$ to $TE_{11,2,2}$ was observed at a magnetic field value $B_0 = 8.445$ T. Smoother transition in power between successive axial modes was verified in simulation by shifting the magnetic field profile 3.5 mm toward the cavity downtaper with respect to the cavity axial center.

The gyrotron cavity was manufactured by electroforming, where oxygen-free copper was deposited on an aluminum mandrel precisely machined to a tolerance of 2.5

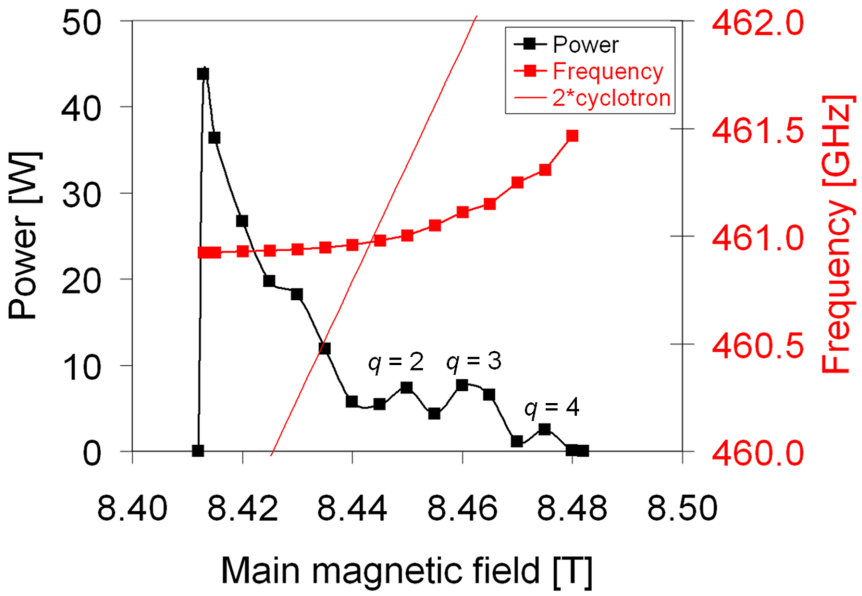

Figure 5-5: Simulated power and frequency tuning as a function of magnetic field for the $TE_{11,2}$ mode. Simulation parameters: $V_b = 13$ kV, $I_b = 100$ mA, $\alpha = 1.9$, $r_e = 1.1$ mm, $\Delta v_\perp / v_\perp = 5\%$, and $r_{cav} = 1.822$ mm. In this simulation, the magnetic field profile was shifted 3.5 mm toward the cavity downtaper with respect to the cavity axial center.

μm in cavity diameter. After fabrication, the gyrotron cavity was cold tested, and the cavity radius was estimated to be 1.823 mm, corresponding to a cutoff frequency of 460.65 GHz for the $TE_{11,2,1}$ mode. The cold test consisted of exciting lower order cavity modes such as $TE_{0,1}$ and $TE_{1,2}$ by means of a step-cut Vlasov converter and measuring the respective resonant frequencies using a vector network analyzer Agilent E8363B with a 90-140-GHz frequency extension as detailed in Section 3.3.2. Once the measured frequencies were corrected for a vacuum environment [118], the cold-cavity code was utilized to determine the cavity radius that would match the corrected frequency.

5.1.3 Internal Mode Converter and Collector

After transferring part of its perpendicular energy to the generated wave, the spent beam is separated from the electromagnetic wave by an internal mode converter, and it is allowed to expand in the decaying field of the superconducting magnet until

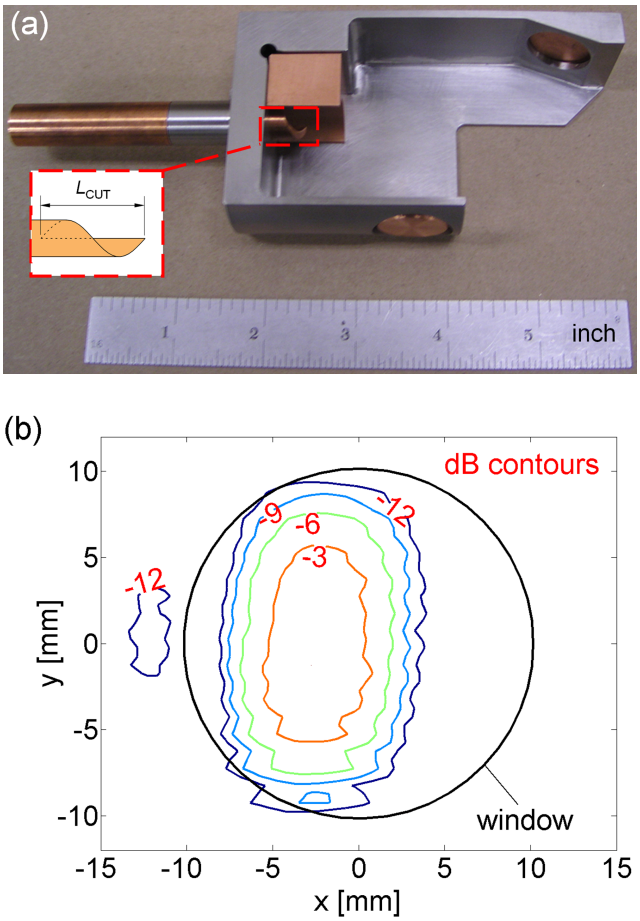

Figure 5-6: (a) Quasi-optical mode converter picture with the inset showing the helical launcher orientation. (b) Simulated electric field profile of the mode-converted $TE_{11,2}$ output beam at the window plane at 460 GHz.

it is collected on a water-cooled copper collector at ground potential. This internal mode converter configuration not only allows a reduction of the thermal load on the collector but also permits a better vacuum conductance throughout the tube, which contributes to the CW operation of the device. Meanwhile, a portion of the generated wave diffracts out of the resonator and propagates through the uptapered section followed by an output cylindrical waveguide of radius $r_{wg} = 2.4$ mm. In the sequence, the cylindrical mode is internally converted into a linearly polarized free-space Gaussian-like beam, which is suitable for low-loss transmission to the NMR probe using a corrugated waveguide.

The internal mode converter is shown in Fig. 5-6(a) and consists of a helical

launcher, a quasi-parabolic mirror, and two flat mirrors to deflect the microwave beam out of the tube through a transparent fused silica window of diameter 20.3 mm and thickness 2.00 mm, and a horizontal cross bore in the superconducting magnet. The converter design is based on a geometrical optics approach [43, 121] using the formalism described in Section 3.4. For the $TE_{11,2}$ mode and output waveguide $r_{wg} = 2.4$ mm, the helical cut length L_{CUT} was determined by Eq. (3.16), yielding $L_{CUT} = 11.2$ mm. The other parameters of the helical launcher are: Brillouin angle $\theta_B = 49.5°$, normalized caustic radius $r_{caustic}/r_{wg} = 0.625$, and azimuthal bounce angle $\psi = 51.3°$.

The design was evaluated using an electric field integral equation code Surf3d [122, 123], and the computed electric field profile of the mode-converted $TE_{11,2}$ output beam at 460 GHz is shown in Fig. 5-6(b). The simulated field profile has a Gaussian-like content of 92% according to Eq. (3.19), with beam radii $w_x = 5.6$ mm and $w_y = 8.7$ mm at the window plane.

5.2 Experimental Results at 460 GHz

The new version of the 460-GHz second-harmonic gyrotron was entirely processed and characterized in CW mode. The temperature of sensitive parts of the tube, such as the anode, cavity, collector, and gun coil, was kept stable by a 2.4-kW recirculating Neslab chiller, model Merlin M-75, with the water temperature and flow at each cooling channel being monitored by flowmeters. Relays existent in these flowmeters and in the ion pump controller formed a hardware safety interlock network ready to shut off the beam voltage if necessary. Software interlocks were also implemented in the computer control routine.

The output power was monitored at the end of a corrugated waveguide connected to the gyrotron window using, unless otherwise specified, a Scientech laser calorimeter model AC2500 (serial nº 4177) calibrated for the submillimeter wavelength range. The corrugated waveguide employed in these measurements has an inner diameter of 19 mm and a corrugation depth of $\lambda/4$ [130]. The other diagnostics utilized in the evaluation of the 460-GHz gyrotron are described in Section 4.2. The main gyrotron

Table 5.1: Operating parameters of 460-GHz gyrotron

Operating mode $TE_{m,p,q}$	$TE_{11,2,q}$
Frequency	460.2 GHz
Magnetic/voltage tuning range	1 GHz
Cavity magnetic field B_0	8.42 T
Cyclotron harmonic	Second
Beam voltage V_b	13 kV
Beam current I_b	100 mA
Output power	16 W (CW)

operating parameters are summarized in Table 5.1.

5.2.1 Start Oscillation Current

The start oscillation current of the operating mode $TE_{11,2}$ was measured as a function of magnetic field for a fixed beam voltage $V_b = 12.8$ kV and a gun coil field $B_{gun} = -75$ mT. The result from this measurement is shown as a solid line in Fig. 5-7, and it is compared to theoretical start currents obtained from linear theory for the first four axial modes $TE_{11,2,q}$, where $q = 1, 2, 3, 4$. In these calculations, the axial electric field profile obtained from a cold-cavity code was employed, and the following beam parameters were assumed: $V_b = 12.8$ kV, $\alpha = 1.85$, and no velocity spread. The cavity radius was chosen to be $r_{cav} = 1.822$ mm for best fit, which is within experimental error of the value (1.823 mm) obtained from the cavity cold test.

Good agreement between the measured and theoretical start currents for the first axial mode $TE_{11,2,1}$ is obtained at lower magnetic field values ($B_0 < 8.44$ T), where the minimum start current was measured to be 27 mA. This represents a start current much lower than 67 mA measured for the operating mode $TE_{0,6}$ in the previous version of the 460-GHz gyrotron [90]. The wider range of excitation of the measured start current compared to the magnetic field range of the theoretical start current for the $TE_{11,2,1}$ mode suggests that high-order axial modes ($q \geqslant 2$) are being observed in the experiment, which is in reasonable agreement with the calculated start currents for high-order axial modes $TE_{11,2,q}$, $q = 2, 3, 4$.

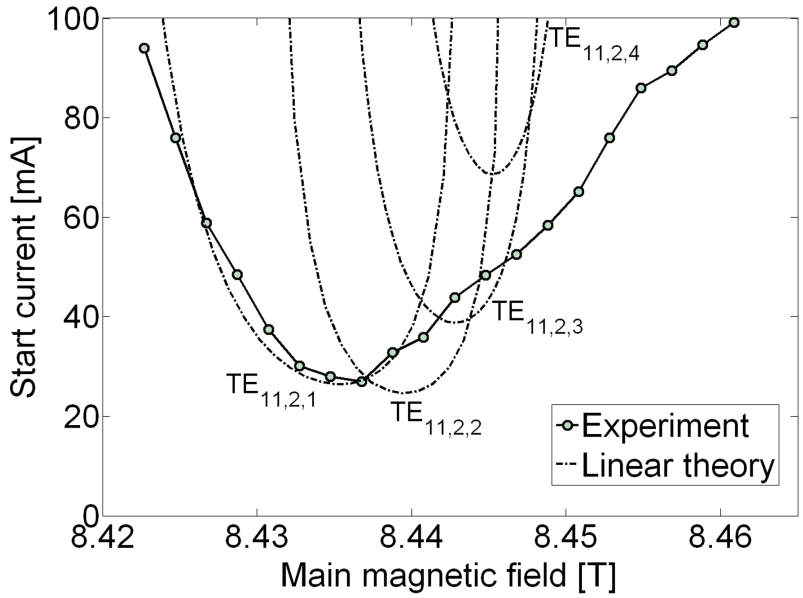

Figure 5-7: Measured start oscillation current (solid line) of the operating mode $TE_{11,2}$ as a function of magnetic field for beam voltage $V_b = 12.8$ kV and a gun coil field $B_{gun} = -75$ mT. Theoretical start currents based on linear theory for the first four axial modes $TE_{11,2,q}$, where $q = 1, 2, 3, 4$, are represented by dashed-dotted lines (simulation parameters: $r_{cav} = 1.822$ mm, cold-cavity axial electric field profile, and beam parameters $V_b = 12.8$ kV and $\alpha = 1.85$, with no velocity spread).

5.2.2 Power and Frequency Tuning

The 460-GHz gyrotron has generated 16 W of output power in the $TE_{11,2,1}$ second-harmonic mode for a 13-kV 100-mA electron beam, yielding an efficiency of 1.2%, a significant improvement compared to the 0.5% efficiency obtained in the previous configuration of this tube [91]. In addition, a smooth frequency tuning range of 1 GHz has been measured as a function of magnetic field for a constant 13-kV 100-mA electron beam, as shown in Fig. 5-8. This represents a tuning range 20 times broader than previously reported for a second-harmonic mode in a submillimeter-wave gyrotron. In the magnetic tuning measurement, the gyrotron output power was optimized by adjusting the subtracting gun coil field from -75 to -78 mT as the main magnetic field was increased, resulting in a minimum output power of 2 W throughout the tuning band.

The measured output power in Fig. 5-8 is in reasonable agreement with the self-consistent simulation result shown in Fig. 5-5, although more power was predicted in

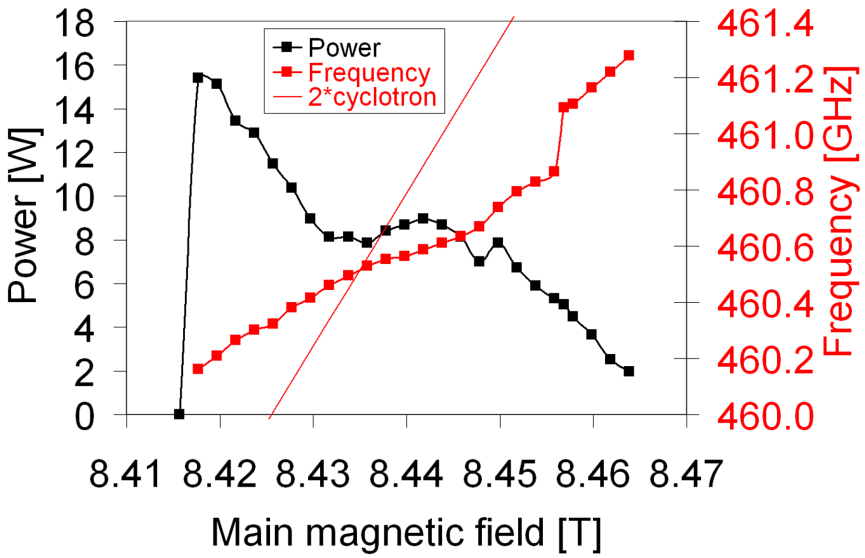

Figure 5-8: Power and frequency tuning measurement as a function of magnetic field for the $TE_{11,2}$ mode, beam current $I_b = 100$ mA, and beam voltage $V_b = 13$ kV. The gun coil was swept from $B_{gun} = -75$ mT to $B_{gun} = -78$ mT for the best output power as the magnetic field was increased.

the simulation at the lower edge of magnetic field values.

As indicated by the start current measurement and the self-consistent simulations, the excitation of successive high-order axial modes $TE_{11,2,q}$ plays a role in providing the extended tuning as one increases the magnetic field for a fixed beam voltage. Electron beam interaction with backward-wave components of high-order axial modes is observed experimentally, and it occurs in a region where the gyrotron radiation frequency is less than the second harmonic of the electron cyclotron frequency. For the magnetic tuning measurement, the backward interaction region corresponds to magnetic field values greater than $B_0 \cong 8.44$ T, a transition region from mode $TE_{11,2,1}$ to $TE_{11,2,2}$ as suggested by the start current measurement in Fig. 5-7 and the self-consistent simulations in Fig. 5-5. Unlike in the simulation where the frequency tunability associated with the high-Q mode $TE_{11,2,1}$ was restricted to a few tens of megahertz, the measured tuning for the same mode reached a few hundreds of megahertz. One factor that may contribute to the broader tuning observed in the experiment is cavity thermal expansion due to the implemented cooling circuit covering a fraction of the cavity surface area similar to the case shown in Fig. 4-13.

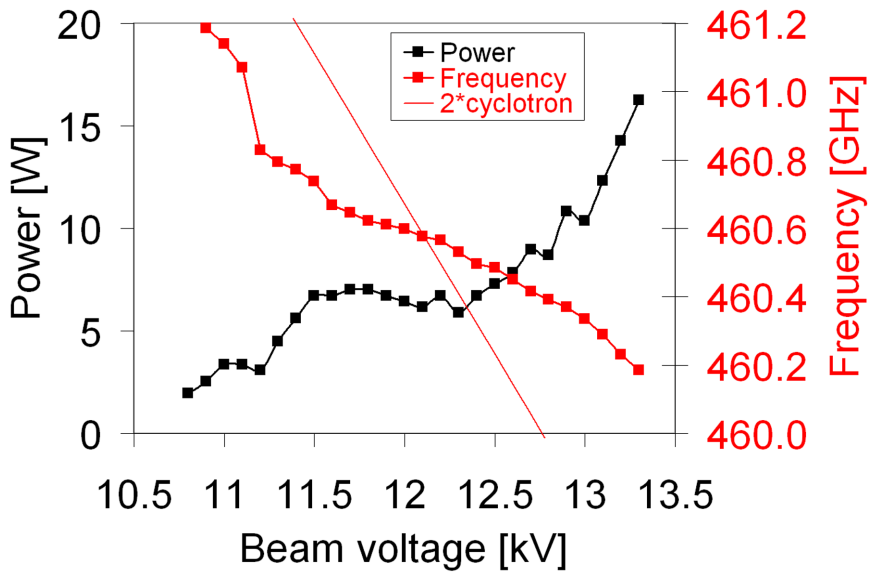

Figure 5-9: Power and frequency tuning measurement as a function of beam voltage for the $TE_{11,2}$ mode, beam current $I_b = 100$ mA, and main magnetic field in persistent mode at $B_0 = 8.422$ T. The gun coil was swept from $B_{gun} = -71$ mT to $B_{gun} = -103$ mT for the best output power as the beam voltage was decreased from the maximum power point.

Tuning measurements were also performed by changing the beam voltage while keeping the main magnetic field at $B_0 = 8.422$ T and the beam current at $I_b = 100$ mA. The voltage tuning results are shown in Fig. 5-9, with similar output power and frequency tuning range compared to the magnetic tuning case. As the beam voltage was decreased from the maximum output power value, the gun coil had to be swept from -71 to -103 mT in order to keep a high α in the diode gun configuration for the best output power.

The tuning performance of the tube while keeping the output power constant at 4 W by varying the beam current was also evaluated. The results are displayed in Fig. 5-10 and Fig. 5-11 with a measured tuning range of 830 MHz for magnetic tuning and 900 MHz for voltage tuning.

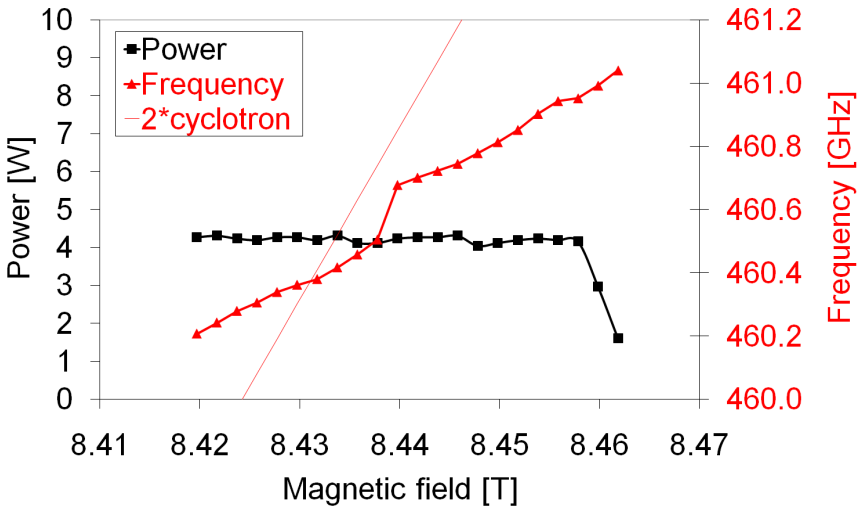

Figure 5-10: Frequency tuning measurement for a constant output power (~ 4 W) as a function of magnetic field for the $TE_{11,2}$ mode, beam voltage $V_b = 12.9$ kV, and gun coil $B_{gun} = -75$ mT. The beam current was changed from $I_b = 60$ mA to $I_b = 104$ mA during the measurement.

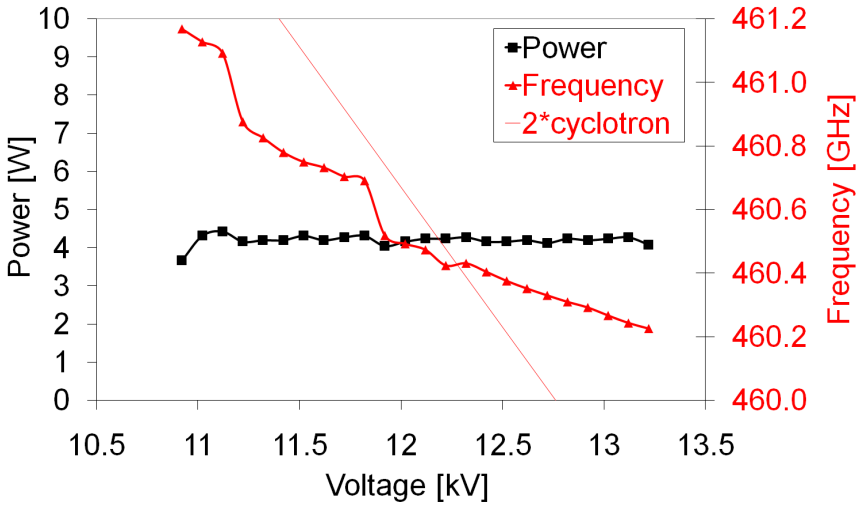

Figure 5-11: Frequency tuning measurement for a constant output power (~ 4 W) as a function of beam voltage for the $TE_{11,2}$ mode, and main magnetic field in persistent mode at $B_0 = 8.422$ T. The beam current and gun coil were changed from $I_b = 58$ mA, $B_{gun} = -75$ mT to $I_b = 106$ mA, $B_{gun} = -99$ mT as the beam voltage was decreased from its maximum value.

5.2.3 Ohmic Loss

At high-frequency operation, a significant part of the power transferred from the electron beam is not extracted from the gyrotron cavity, but instead, it is deposited in the cavity walls as ohmic loss. By measuring the water flow rate in the cavity cooling channel and the difference between its inlet and outlet temperature using thermistors, Omega model 44007, the amount of power transferred from the gyrotron cavity to the water cooling circuit could be calculated. For a gyrotron output power of 5.2 W at 460.28 GHz and a flow rate of 0.7 gpm, the ohmic loss was estimated to be 53 W. Thus, only 9% of the power generated in the first axial mode $TE_{11,2,1}$ in the cavity is extracted as useful output power. This experimental extraction efficiency value η_{RF} is in good agreement with the theoretical one for the $TE_{11,2,1}$ mode, $\eta_{RF\_theory} = (1 + Q_{D,1}/Q_O)^{-1} = 8\%$. The beam parameters during this measurement were $V_b = 12.9$ kV and $I_b = 79$ mA with the main magnetic field at $B_0 = 8.423$ T.

5.2.4 CW Long-Term Stable Operation

Continuous gyrotron operation for extended periods with stable power and frequency characteristics is an important requirement to allow long-term signal averaging in DNP/NMR experiments. The long-term stability of the 460-GHz gyrotron operating in the $TE_{11,2}$ mode was evaluated for a period of two days, and the monitored variables are shown in Fig. 5-12. A quasi-optical directional coupler [133] was utilized at the end of the output corrugated waveguide to divert part of the output power to the frequency measurement system. The gyrotron output power was kept stable within $\pm 0.7\%$ by a computerized proportional, integral, and derivative (PID) control system implemented in LabVIEW that adjusted the cathode filament current based on the difference between a set point value and the output power monitored by a calibrated diode. This level of power fluctuation and the observed frequency stability of ± 2.9 MHz (± 6 ppm) are suitable for DNP/NMR. During the stability test, the main superconducting magnet was in persistent mode at $B_0 = 8.422$ T, which has a magnetic field drift rate of less than 0.02 ppm/h according to a NMR probe measurement.

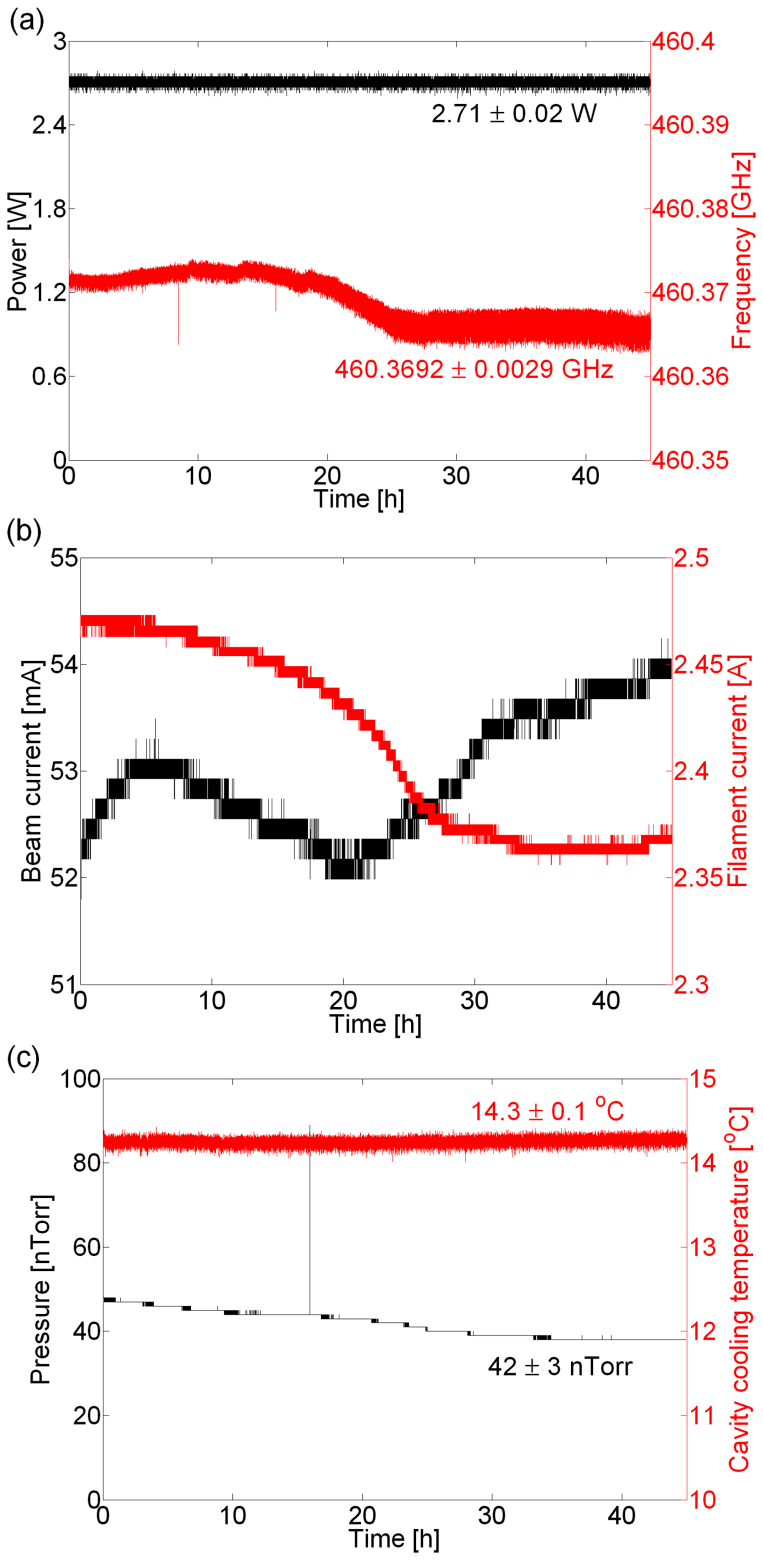

Figure 5-12: Monitored variables during the long-term stability test of the 460-GHz gyrotron operating in the second-harmonic $TE_{11,2}$ mode: (a) output power and frequency, (b) beam and filament currents, (c) pressure and cavity cooling temperature, and (d) beam voltage. During the test, the magnetic field was persistent at $B_0 = 8.422$ T and the beam voltage was kept at $V_b = 12.75$ kV.

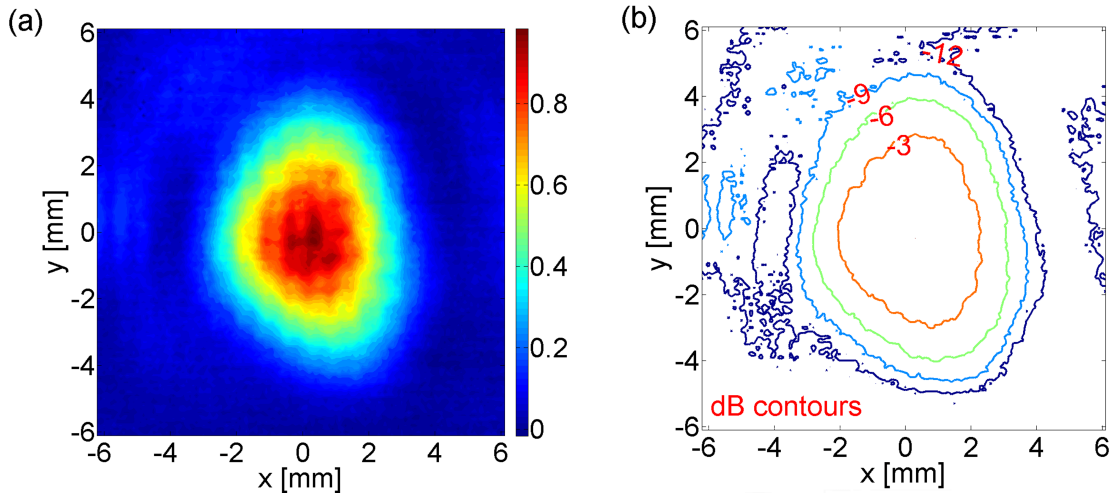

Figure 5-13: Gyrotron output microwave beam displayed in (a) a normalized linear power scale and (b) dB contours. The pyroelectric camera image of the mode-converted $TE_{11,2}$ mode at 460.3 GHz was taken 40 mm after the end of the corrugated waveguide.

5.2.5 Output Beam Pattern

The gyrotron output beam pattern was measured by the Spiricon Pyrocam III pyroelectric camera positioned after the corrugated waveguide connected to the gyrotron window. During the camera measurements, the gyrotron output power was limited to 0.4 W, below the camera sensor damage threshold of 2 W.

An image of the mode-converted $TE_{11,2}$ beam at 460.3 GHz captured 40 mm after the end of the corrugated waveguide is shown in Fig. 5-13. Based on the measured pattern, the Gaussian-like content associated with the measured microwave beam was computed to be 92% with beam radii $w_x = 4.1$ mm and $w_y = 4.6$ mm, corresponding to an ellipticity of 12%. Due to the limited access provided by the horizontal cross bore of the superconducting magnet, a direct beam measurement after the gyrotron window was not possible using the pyroelectric camera. However, measurements performed with thermal paper inside the cross bore corroborated the camera results and confirmed the alignment of the output beam trajectory with respect to the cross-bore centerline. These results indicate a good performance of the implemented internal quasi-optical converter from a whispering-gallery mode $TE_{11,2}$ to a Gaussian-like mi-

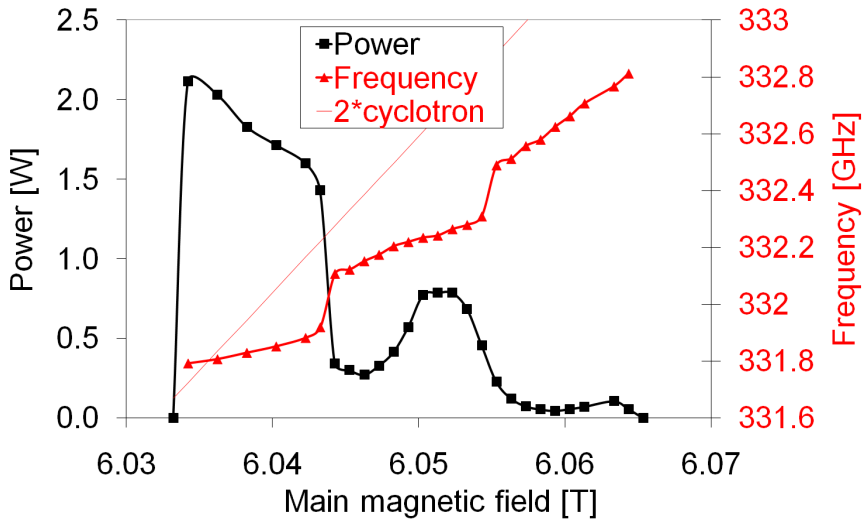

Figure 5-14: Power and frequency tuning measurement as a function of magnetic field for the $TE_{-4,3}$ mode, beam current $I_b = 50$ mA, and beam voltage $V_b = 9.4$ kV. The gun coil was swept from $B_{gun} = -20$ mT to $B_{gun} = -26$ mT for the best output power as the magnetic field was increased.

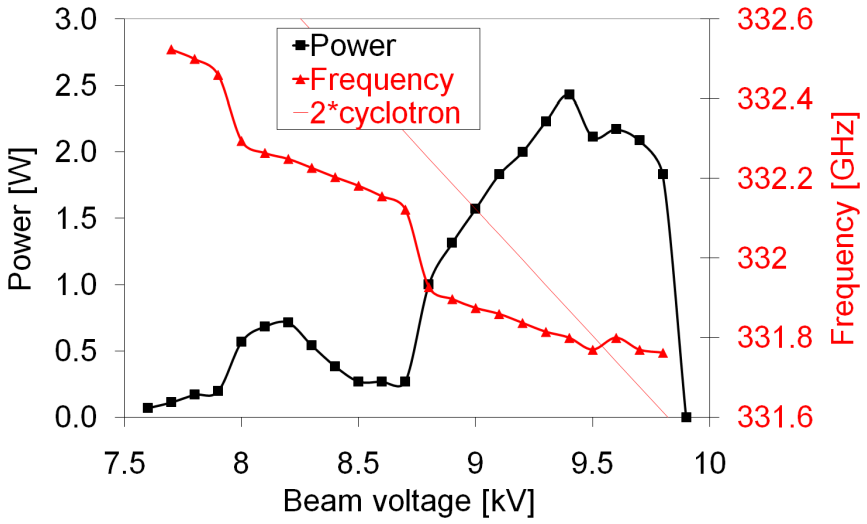

Figure 5-15: Power and frequency tuning measurement as a function of beam voltage for the $TE_{11,2}$ mode, beam current $I_b = 50$ mA, and main magnetic field in persistent mode at $B_0 = 6.037$ T. The gun coil was swept from $B_{gun} = -16$ mT to $B_{gun} = -48$ mT for the best output power as the beam voltage was decreased from the maximum power point.

crowave beam at a submillimeter wavelength.

5.3 Experimental Results at 332 GHz

Besides the results obtained with the operating mode $TE_{11,2}$ at 460 GHz, excitation of a counter-rotating mode $TE_{-4,3}$ with radiation frequency near 332 GHz has also been observed. As the implemented mode converter in the 460-GHz tube was not optimized for the mode $TE_{-4,3}$ and the installed gyrotron window has a power transmission coefficient of 0.71 at 332 GHz, magnetic and voltage tuning measurements were carried out at a low beam current $I_b = 50$ mA. The magnetic and voltage tuning data obtained are shown in Fig. 5-14 and Fig. 5-15, respectively, where a frequency tuning range as broad as 1 GHz was achieved, supported mostly by backward-wave interaction.

5.4 Discussion

The improved version of the 460-GHz second-harmonic gyrotron has generated 16 W of output power for a 13-kV 100-mA electron beam, yielding an efficiency of 1.2%. The minimum start current of the operating mode $TE_{11,2,1}$ was measured to be 27 mA, agreeing with the linear theory prediction. Smooth frequency tunability of 1 GHz has been demonstrated for the operating second-harmonic mode as a function of the cyclotron frequency either by magnetic field tuning or beam voltage tuning. This frequency tuning range is 20 times broader than previously observed for a second-harmonic mode in a submillimeter-wave gyrotron. A frequency-tunable microwave source is highly desirable since it simplifies the implementation of DNP in NMR spectrometers, particularly the ones without sweep coils. The stability characteristics of the gyrotron have been evaluated during a period of two days in which the gyrotron operated continuously under computerized PID control monitoring the CW output power. A power stability of $\pm 0.7\%$ and a frequency stability of ± 2.9 MHz (± 6 ppm) have been obtained, which are suitable for the 700-MHz DNP/NMR application for which the gyrotron was designed. The Gaussian-like content of the measured mode-

converted $TE_{11,2}$ output beam was calculated to be 92% with an ellipticity of 12%, indicating proper operation of the implemented internal quasi-optical mode converter. In addition to the results at 460 GHz, frequency tunability as broad as 1 GHz has been achieved near 332 GHz with the counter-rotating mode $TE_{-4,3}$.

Chapter 6

Conclusion

6.1 Relevance and Summary of Results

This thesis successfully demonstrated for the first time that a continuous frequency tuning range greater than 1 GHz can be experimentally achieved for a second-harmonic mode in a submillimeter-wave gyrotron as a function of the cyclotron frequency via magnetic tuning or beam voltage tuning. Even though simulation results indicated that a tuning range on the order of 1 GHz could be achieved for realistic electron beam parameters using magnetic tuning, skepticism was in place due to the narrow tuning range of 50 MHz measured in the past for second-harmonic gyrotrons in the submillimeter band (*cf* Table 1.1).

Although second-harmonic modes have the advantage of doubling the gyrotron frequency for a given magnet system or requiring a superconducting magnet with half of the field of that for a fundamental-harmonic mode, operation in a second-harmonic mode is challenging due to lower interaction efficiency and higher start current that arises from the lower gain as detailed in Chapter 3. In order to overcome these issues, a second-harmonic mode with a high beam-wave coupling and sufficiently isolated from adjacent modes was chosen as the operating mode in the 330-GHz and 460-GHz gyrotrons. Furthermore, a long interaction structure was preferred in order to lower the start oscillation current and enable the access to high-order axial modes for continuous frequency tunability in a system with continuous-wave (CW) beam current

limited to 200 mA. Another challenge associated with high-frequency operation is the predominance of ohmic loss over diffractive loss. As a consequence, the majority of the power transferred from the electron beam is dissipated in the cavity walls, leading to extraction efficiency of about 8% or less from the gyrotron cavity as reported in Chapters 4 and 5.

The 330-GHz second-harmonic gyrotron was designed to operate in the second-harmonic mode $TE_{-4,3,q}$. In the first configuration of the gyrotron utilizing a superconducting magnet manufactured by Cryomagnetics, the oscillator has generated 18 W of output power for a 10.1-kV 190-mA electron beam, yielding an efficiency of 0.93%. The minimum starting current of the operating second-harmonic mode was measured to be 33 mA for a beam voltage of 10.1 kV. Good agreement was observed between the measured start current values and the prediction from linear theory for the first six axial modes ($q = 1$ to $q = 6$). Also the measured frequency at each start current value with a low equilibrium power value reasonably agrees with the cold-cavity frequency of each axial mode.

Continuous frequency tunability of 1.2 GHz with a minimum output power of 2 W was achieved via cyclotron frequency tuning and cavity thermal tuning. Considering the 500-MHz dynamic nuclear polarization/nuclear magnetic resonance (DNP/NMR) application for which this gyrotron was designed, the measured frequency tuning range of 328.96 GHz to 329.93 GHz covers the frequency of 329.4 GHz that yields the maximum DNP/NMR enhancement.

The long-term stability of the 330-GHz gyrotron output was evaluated during an uninterrupted period of 110 h in which the gyrotron operated continuously under computerized proportional, integral, and derivative (PID) control monitoring the CW output power. During this test, the power and frequency were stable within $\pm 0.4\%$ and ± 1.1 MHz (± 3 ppm), respectively, meeting the specifications for long-term signal averaging in DNP/NMR experiments. Proper operation of the implemented quasi-optical mode converter has been verified as an output microwave beam with a Gaussian-like mode content of 92% has been recorded using a pyroelectric camera.

Besides these results in CW regime, measurements were also performed in mi-

crosecond pulse operation at a higher beam current of 610 mA, where tunability of 1.2 GHz with a minimum output power of 20 W has been achieved by means of cyclotron frequency tuning and thermal tuning. The measured frequencies in pulse operation are consistent with the ones obtained in the start current measurement at low equilibrium power points due to the absence of cavity deformation.

The performance of the oscillator was also assessed in the superconducting magnet ordered for the 330-GHz gyrotron and manufactured by Bruker. The experimental results in the new magnet system are consistent with the ones obtained in the Cryomagnetics magnet for power and frequency tuning, start oscillation current, and ohmic loss. Magnetic and voltage tuning measurements for a beam current of 190 mA demonstrated an output power of 1-19 W (CW) in the frequency range of 328.82 GHz to 330.05 GHz. The minimum start current was measured to be 21 mA for the operating mode $TE_{-4,3}$, where good agreement was verified between the measured start current values and the calculation from linear theory for the first six axial modes ($q = 1$ to $q = 6$). Furthermore, the measured frequency at each start current value with a low equilibrium power value reasonably agrees with the cold-cavity frequency of each axial mode. Evaluation of the image of the output microwave beam taken with a pyroelectric camera after the corrugated waveguide revealed a Gaussian-like content of 91%.

In addition to the 330-GHz gyrotron, this thesis also reported the design and operation of a tunable second-harmonic 460-GHz CW gyrotron to be used as a submillimeter-wave source in 700-MHz DNP/NMR experiments. The 460-GHz gyrotron has generated 16 W of output power for a 13-kV 100-mA electron beam, yielding an efficiency of 1.2%. The minimum start current of the operating mode $TE_{11,2,1}$ was measured to be 27 mA, agreeing with the linear theory prediction. Smooth frequency tunability of 1 GHz has been also achieved for the operating second-harmonic mode as a function of the cyclotron frequency either by magnetic field tuning or beam voltage tuning. The stability characteristics of the gyrotron have been evaluated during a period of two days in which the gyrotron operated continuously under computerized PID control monitoring the CW output power. A power stability of

±0.7% and a frequency stability of ±2.9 MHz (±6 ppm) have been obtained, which are suitable for the DNP/NMR application. The Gaussian-like content of the measured mode-converted $TE_{11,2}$ output beam was calculated to be 92% with an ellipticity of 12%, indicating proper operation of the implemented internal quasi-optical mode converter.

6.2 Future Work and Directions

A continuously frequency tunable gyrotron is highly desirable for DNP/NMR experiments since it simplifies the implementation of DNP in NMR spectrometers, particularly the ones without magnetic tuning capability. Also, the voltage tuning capability studied in this work may be explored in future DNP/NMR experiments since it enables fast frequency sweep.

The final version of the 330-GHz gyrotron delivered a minimum CW power level of 1 W over a continuous tuning range of 1.2 GHz, and 5 W of a continuous tuning range of 700 MHz as summarized in Table 4.1. A transmission line and a DNP probe are being fabricated to complete the 500-MHz DNP/NMR setup. The 460-GHz gyrotron produced a minimum power level of 2 W over 1 GHz, and of 4 W over 900 MHz. In order to bring the performance of the gyrotron closer to the desired one for DNP/NMR, a minimum power level of 5 W over a 1.5 GHz tuning range, some options can be considered.

Operation at a higher beam power at second harmonic will increase the output power of the device without necessarily broadening the associated cyclotron tuning range as shown by the pulse measurements at 330 GHz. Appropriate analysis of the thermal load in the gyrotron cavity and collector should follow before any increase in beam power. An improved configuration for the cavity cooling circuit is advised in order to reduce the cavity temperature rise and the frequency detuning observed in CW regime in the current 330-GHz and 460-GHz gyrotrons. Today, cyclotron frequency tuning of a fundamental-harmonic mode would be a proven choice to achieve the ideal DNP/NMR power and frequency tuning goals but that would require an

expensive new superconducting magnet.

Another possibility would be to use an alternative interaction structure such as a mechanically tunable split cavity. Issues to be addressed for this structure include the precise alignment required between the two cavity halves, integration of the cavity cooling circuit, and the need of additional vacuum feedthroughs depending on the implementation to move the parts precisely and to hold them stably.

References

[1] G. Caryotakis, "Klystrons," in *Modern Microwave and Millimeter-Wave Power Electronics*, R. J. Barker, J. H. Booske, N. C. Luhmann, Jr., and G. S. Nusinovich, Eds. Wiley-Interscience, 2005, pp. 107–170.

[2] S. H. Gold and G. S. Nusinovich, "Review of high-power microwave source research," *Rev. Sci. Instrum.*, vol. 68, no. 11, pp. 3945–3974, Nov. 1997.

[3] J. R. Sirigiri, K. E. Kreischer, J. Machuzak, I. Mastovsky, M. A. Shapiro, and R. J. Temkin, "Photonic-band-gap resonator gyrotron," *Phys. Rev. Lett.*, vol. 86, no. 24, pp. 5628–5631, Jun. 2001.

[4] W. Hu, M. A. Shapiro, K. E. Kreischer, and R. J. Temkin, "140-GHz gyrotron experiments based on a confocal cavity," *IEEE Trans. Plasma Sci.*, vol. 26, no. 3, pp. 366–374, Jun. 1998.

[5] K. R. Chu and J. L. Hirshfield, "Comparative study of the axial and azimuthal bunching mechanisms in electromagnetic cyclotron instabilities," *Phys. Fluids*, vol. 21, no. 3, pp. 461–466, Mar. 1978.

[6] J. E. Brittain, "Eletrical engineering hall of fame: Ernest F. W. Alexanderson," *Proc. IEEE*, vol. 92, no. 7, pp. 1216–1219, Jul. 2004.

[7] ——, "Eletrical engineering hall of fame: Peder O. Pedersen," *Proc. IEEE*, vol. 94, no. 7, pp. 1464–1466, Jul. 2006.

[8] E. W. Herold, "The impact of receiving tubes on broadcast and TV receivers," *Proc. IRE*, vol. 50, no. 5, pp. 805–810, May 1962.

[9] A. V. Gaponov-Grekhov and V. L. Granatstein, *Applications of High-Power Microwaves*. Norwood, MA: Artech House, 1994.

[10] V. L. Granatstein, R. K. Parker, and C. M. Armstrong, "Vacuum electronics at the dawn of the twenty-first century," *Proc. IEEE*, vol. 87, no. 5, pp. 702–716, May 1999.

[11] R. H. Varian and S. F. Varian, "A high frequency oscillator and amplifier," *J. Appl. Phys.*, vol. 10, pp. 321–327, May 1939.

[12] R. H. Abrams, B. Levush, A. A. Mondelli, and R. K. Parker, "Vacuum eletronics for the 21st century," *IEEE Microw. Mag.*, vol. 9, pp. 61–72, Sep. 2001.

[13] T. Habermann, A. Balkcum, R. Begum, H. Bohlen, M. Cattelino, E. Eisen, D. Gajaria, A. Staprans, B. Stockwell, and L. Zitelli, "High-power high-efficiency L-band multiple-beam klystron development at CPI," *IEEE Trans. Plasma Sci.*, vol. 38, no. 6, pp. 1264–1269, Jun. 2010.

[14] M. Cusick, J. Atkinson, A. Balkcum, G. Caryotakis, D. Gajaria, T. Grant, C. Meyer, K. Lind, M. Perrin, G. Scheitrum, and A. Jensen, "X-band sheet beam klystron (XSBK)," in *Proc. of IEEE Int. Vacuum Electronics Conference*, Rome, Italy, Apr. 2009, pp. 296–297.

[15] D. Sprehn, G. Caryotakis, A. Haase, E. Jongewaard, and C. Pearson, "Current status of the Next Linear Collider X-band klystron development program," in *Proc. of EPAC 2004*, Lucerne, Switzerland, Jul. 2004, pp. 1090–1092.

[16] L. Laurent and E. Jongewaard, "Autopsy report on three SLAC X-band klystron output circuits," in *Proc. of IEEE Int. Vacuum Electronics Conference*, Rome, Italy, Apr. 2009, pp. 542–543.

[17] B. Steer, A. Roitman, P. Horoyski, M. Hyttinen, R. Dobbs, and D. Berry, "Extended interaction klystron technology at millimeter and sub-millimeter wavelengths," Commun. Power Ind. Canada Inc., Georgetown, Canada, Apr. 2010. [Online]. Available: http://www.cpii.com/docs/related/40/EIK%20Technology%20at%20MMW%20&%20SubMMW%20Wavelengths.pdf

[18] H. A. H. Boot and J. T. Randall, "Historical notes on the cavity magnetron," *IEEE Trans. Electron Devices*, vol. ED-23, no. 7, pp. 724–729, Jul. 1976.

[19] *Magnetrons*, L3 Commun. Electron Devices, Williamsport, PA, May 2010. [Online]. Available: http://www.l-3com.com/edd/magnetrons.htm

[20] *Magnetrons*, Commun. Power Ind. Inc., Beverly, MA, May 2010. [Online]. Available: http://www.cpii.com/product.cfm/8/2/16

[21] J. Benford, J. A. Swegle, and E. Schamiloglu, *High Power Microwaves*. Boca Raton, FL: Taylor & Francis, 2007.

[22] *Crossed-Field Amplifiers*, Commun. Power Ind. Inc., Beverly, MA, May 2010. [Online]. Available: http://www.cpii.com/product.cfm/8/3/3

[23] *Crossed-Field Amplifiers*, L3 Commun. Electron Devices, Williamsport, PA, May 2010. [Online]. Available: http://www.l-3com.com/edd/products_cfas.htm

[24] R. Kompfner, "The invention of traveling wave tubes," *IEEE Trans. Electron Devices*, vol. ED-23, no. 7, pp. 730–738, Jul. 1976.

[25] V. L. Bratman, B. S. Dumesh, A. E. Fedotov, P. B. Makhalov, B. Z. Movshevich, and F. S. Rusin, "Terahertz orotrons and oromultipliers," *IEEE Trans. Plasma Sci.*, vol. 38, no. 6, pp. 1466–1471, Jun. 2010.

[26] C. L. Kory, M. E. Read, R. L. Ives, J. H. Booske, and P. Borchard, "Design of overmoded interaction circuit for 1-kW 95-GHz TWT," *IEEE Trans. Electron Devices*, vol. 56, no. 5, pp. 713–720, May 2009.

[27] E. N. Comfoltey, M. A. Shapiro, J. R. Sirigiri, and R. J. Temkin, "Design of an overmoded W-band TWT," in *Proc. of IEEE Int. Vacuum Electronics Conference*, Rome, Italy, Apr. 2009, pp. 127–128.

[28] W. L. Menninger, T. K. Phelps, and J. Lingenfelter, "Performance and reliability of recent production space linearized traveling-wave tube amplifiers," in *Proc. of IEEE Int. Vacuum Electronics Conference*, Monterey, CA, May 2010, pp. 49–50.

[29] J. Tucek, M. Basten, D. Gallagher, and K. Kreischer, "Sub-millimeter and THz power amplifier development at Northrop Grumman," in *Proc. of IEEE Int. Vacuum Electronics Conference*, Monterey, CA, May 2010, pp. 19–20.

[30] M. Field, R. Borwick, V. Mehrotra, B. Brar, J. Zhao, Y.-M. Shin, D. Gamzina, A. Spear, A. Baig, L. Barnett, N. Luhmann, T. Kimura, J. Atkinson, T. Grant, Y. Goren, and D. E. Pershing, "220 GHz 50 W sheet beam travelling wave tube amplifier," in *Proc. of IEEE Int. Vacuum Electronics Conference*, Monterey, CA, May 2010, pp. 21–22.

[31] *Backward-Wave Oscillators*, Microtech Instruments, Inc., Eugene, OR, May 2010. [Online]. Available: http://www.mtinstruments.com/downloads/THz%20Generators%20Datasheet.pdf

[32] G. Kantorowicz and P. Palluel, "Backward wave oscillators," in *Infrared and Millimeter Waves*, K. J. Button, Ed. New York, NY: Academic, 1970, pp. 185–212.

[33] K. Kreischer, J. Tucek, D. Gallagher, and R. E. Mihailovich, "Operation of a compact, 0.65 THz source," in *Proc. of 33rd Int. Conf. on Infrared, Millimeter, and THz Waves*, Pasadena, CA, Sep. 2008, pp. 1–2.

[34] R. Q. Twiss, "Radiation transfer and the possibility of negative absorption in radio astronomy," *Australian J. Phys.*, vol. 11, pp. 564–579, Dec. 1958.

[35] J. Schneider, "Stimulated emission of radiation by relativistic electrons in a magnetic field," *Phys. Rev. Let.*, vol. 2, no. 12, pp. 504–505, Jun. 1959.

[36] A. V. Gaponov, "Interaction between electron fluxes and electromagnetic waves in waveguides," *Izv. VUZov Radiofizika*, vol. 2, pp. 450–462, 1959, (in Russian).

[37] J. L. Hirshfield and J. M. Wachtel, "Electron cyclotron maser," *Phys. Rev. Lett.*, vol. 12, no. 19, pp. 533–536, May 1964.

[38] G. S. Nusinovich, *Introduction to the Physics of Gyrotrons.* Baltimore, MD: Johns Hopkins, 2004.

[39] K. R. Chu, "The electron cyclotron maser," *Rev. Mod. Phys.*, vol. 76, pp. 489–540, Apr. 2004.

[40] V. A. Flyagin and G. S. Nusinovich, "Gyrotron oscillators," *Proc. IEEE*, vol. 76, no. 6, pp. 644–656, Jun. 1988.

[41] V. L. Bratman, N. S. Ginzburg, G. S. Nusinovich, M. I. Petelin, and P. S. Strelkov, "Relativistic gyrotrons and cyclotron autoresonance masers," *Int. J. Electron.*, vol. 51, no. 4, pp. 541–567, 1981.

[42] M. Thumm, "State-of-the-art of high power gyro-devices and free electron masers, Update 2009," Karlsruhe Institute of Technology, Karlsruhe, Germany, Tech. Rep. KIT-SR 7540, 2010.

[43] S. N. Vlasov, L. I. Zagryadskaya, and M. I. Petelin, "Transformation of a whispering gallery mode, propagating in a circular waveguide, into a beam of waves," *Radio Eng. Electron. Phys.*, vol. 12, no. 10, pp. 14–17, 1975.

[44] G. G. Denisov, A. N. Kuftin, V. I. Malygin, N. P. Venediktov, D. V. Vinogradov, and V. E. Zapevalov, "110 GHz gyrotron with built-in high-efficiency converter," *Int. J. Electron.*, vol. 72, no. 5 and 6, pp. 1079–1091, 1992.

[45] M. Thumm, "Development of ouput windows for high-power long-pulse gyrotrons and EC wave applications," *Int. J. Infrared and Millim. Waves*, vol. 19, no. 1, pp. 3–14, Jan. 1998.

[46] A. Kasugai, K. Sakamoto, K. Takahashi, K. Kajiwara, and N. Kobayashi, "Steady-state operation of 170 GHz-1 MW gyrotron for ITER," *Nucl. Fusion*, vol. 48, no. 5, p. 054009, May 2008.

[47] T. Rzesnicki, B. Piosczyk, S. Kern, S. Illy, J. Jin, A. Samartsev, A. Schlaich, and M. Thumm, "2.2-MW record power of the 170-GHz European preprototype coaxial-gyrotron for ITER," *IEEE Trans. Plasma Sci.*, vol. 38, no. 6, pp. 1141–1149, Jun. 2010.

[48] N. I. Zaytsev, T. B. Pankratova, M. I. Petelin, and V. A. Flyagin, "Millimeter- and submillimeter-wave gyrotrons," *Radio Eng. Electron. Phys.*, vol. 19, no. 5, pp. 103–107, May 1974.

[49] S. Spira-Hakkarainen, K. E. Kreischer, and R. J. Temkin, "Submillimeter-wave harmonic gyrotron experiment," *IEEE Trans. Plasma Sci.*, vol. 18, no. 3, pp. 334–342, Jun. 1990.

[50] T. Notake, T. Saito, Y. Tatematsu, A. Fujii, S. Ogasawara, L. Agusu, I. Ogawa, T. Idehara, and V. N. Manuilov, "Development of a novel high power sub-THz second harmonic gyrotron," *Phys. Rev. Lett.*, vol. 103, p. 225002, 2009.

[51] M. Yu. Glyavin, A. G. Luchinin, and G. Yu. Golubiatnikov, "Generation of 1.5-kW, 1-THz coherent radiation from a gyrotron with a pulsed magnetic field," *Phys. Rev. Lett.*, vol. 100, p. 015101, 2008.

[52] T. Idehara, I. Ogawa, H. Mori, S. Kobayashi, S. Mitsudo, and T. Saito, "A Thz gyrotron FU CW II with a 20T superconducting magnet," *J. Plasma Fusion Res. SERIES*, vol. 8, pp. 1508–1511, 2009.

[53] V. L. Bratman, Yu. K. Kalynov, and V. N. Manuilov, "Large-orbit gyrotron operation in the terahertz frequency range," *Phys. Rev. Lett.*, vol. 102, p. 245101, 2009.

[54] M. A. Basten, W. C. Guss, K. E. Kreischer, R. J. Temkin, and M. Caplan, "Experimental investigation of a 140 GHz gyrotron-backward wave oscillator," *Int. J. Infrared and Millim. Waves*, vol. 16, no. 5, pp. 889–905, May 1995.

[55] S. V. Samsonov, G. G. Denisov, V. L. Bratman, A. A. Bogdashov, M. Yu. Glyavin, A. G. Luchinin, V. K. Lygin, and M. K. Thumm, "Frequency-tunable CW gyro-BWO with a helically rippled operating waveguide," *IEEE Trans. Plasma Sci.*, vol. 32, no. 3, pp. 884–889, Jun. 2004.

[56] C. R. Donaldson, W. He, A. W. Cross, F. Li, A. D. R. Phelps, L. Zhang, K. Ronald, C. W. Robertson, C. G. Whyte, and P. McElhinney, "Experimental demonstration of a W-band gyro-BWO using a helically corrugated waveguide," in *Proc. of IEEE Int. Vacuum Electronics Conference*, Monterey, CA, May 2010, pp. 195–196.

[57] M. Blank, P. Borchard, S. Cauffman, and K. Felch, "Design and demonstration of W-band gyrotron amplifiers for radar applications," in *Proc. of 32nd Int. Conf. on Infrared and Millimeter and 15th Int. Conf. on Terahertz Electronics*, Cardiff, UK, Sep. 2007, pp. 364–366.

[58] H. Jory, M. Blank, S. Cauffman, and K. Felch, "Gyrotron introduction for Ecris 2008," in *Proc. of 18th Int. Workshop on ECR Ion Sources*, Chicago, IL, Sep. 2008, pp. 174–177.

[59] M. Blank, P. Borchard, S. Cauffman, and K. Felch, "Demonstration of a broadband W-band gyro-TWT amplifier," in *Proc. of IEEE Int. Vacuum Electronics Conference*, Monterey, CA, Apr. 2006, pp. 459–460.

[60] J. R. Sirigiri, M. A. Shapiro, and R. J. Temkin, "High-power 140-GHz quasioptical gyrotron traveling-wave amplifier," *Phys. Rev. Lett.*, vol. 90, no. 25, p. 258302, Jun. 2003.

[61] C. D. Joye, M. A. Shapiro, J. R. Sirigiri, and R. J. Temkin, "Demonstration of a 140-GHz 1-kW confocal gyro-traveling-wave amplifier," *IEEE Trans. Electron Devices*, vol. 56, no. 5, pp. 818–827, May 2009.

[62] E. A. Nanni, M. A. Shapiro, J. R. Sirigiri, and R. J. Temkin, "Design of a 250 GHz photonic band gap gyrotron amplifier," in *Proc. of IEEE Int. Vacuum Electronics Conference*, Monterey, CA, May 2010, pp. 317–318.

[63] L. R. Becerra, G. J. Gerfen, R. J. Temkin, D. J. Singel, and R. G. Griffin, "Dynamic nuclear polarization with a cyclotron resonance maser at 5 T," *Phys. Rev. Lett.*, vol. 71, no. 21, pp. 3561–3564, Nov. 1993.

[64] L. R. Becerra, G. J. Gerfen, B. F. Bellew, J. A. Bryant, D. A. Hall, S. J. Inati, R. T. Weber, S. Un, T. F. Prisner, A. E. McDermott, K. W. Fishbein, K. E. Kreischer, R. J. Temkin, D. J. Singel, and R. G. Griffin, "A spectrometer for dynamic nuclear polarization and electron paramagnetic resonance at high frequencies," *J. Magn. Reson.*, vol. 117, pp. 28–40, 1995.

[65] T. Maly, G. T. Debelouchina, V. S. Bajaj, K.-N. Hu, C.-G. Joo, M. L. Mak-Jurkauskas, J. R. Sirigiri, P. C. A. van der Wel, J. Herzfeld, R. J. Temkin, and R. G. Griffin, "Dynamic nuclear polarization at high magnetic fields," *J. Chem. Phys.*, vol. 128, no. 5, p. 052211, Feb. 2008.

[66] G. J. Gerfen, L. R. Becerra, D. A. Hall, R. G. Griffin, R. J. Temkin, and D. J. Singel, "High frequency (140 GHz) dynamic nuclear polarization: Polarization transfer to a solute in frozen aqueous solution," *J. Chem. Phys.*, vol. 102, no. 24, pp. 9494–9497, Jun. 1995.

[67] C.-G. Joo, K.-N. Hu, J. A. Bryant, and R. G. Griffin, "In situ temperature jump high-frequency dynamic nuclear polarization experiments: Enhanced sensitivity in liquid-state NMR spectroscopy," *J. Amer. Chem. Soc.*, vol. 128, no. 29, pp. 9428–9432, Jul. 2006.

[68] V. S. Bajaj, M. K. Hornstein, K. E. Kreische, J. R. Sirigiri, P. P. Woskov, M. L. Mak-Jurkauskas, J. Herzfeld, R. J. Temkin, and R. G. Griffin, "250 GHz CW gyrotron oscillator for dynamic nuclear polarization in biological solid state NMR," *J. Magn. Reson.*, vol. 189, no. 2, pp. 251–279, Dec. 2007.

[69] A. B. Barnes, Private communication, Mar. 2010.

[70] R. J. Trew, "High-frequency solid-state electronic devices," *IEEE Trans. Electron Devices*, vol. 52, no. 5, pp. 638–649, May 2005.

[71] J. L. Hesler, D. S. Kurtz, Y. Duan, and T. W. Crowe, "Solid-state sources, receivers and systems for plasma diagnostics and THz frequency extenders for VNAs," in *Proc. IEEE 36th Int. Conf. Plasma Sci.*, San Diego, CA, Jun. 2009, p. 1.

[72] A. K. Hassan, L. A. Pardi, J. Krzystek, A. Sienkiewicz, P. Goy, M. Rohrer, and L.-C. Brunel, "Ultrawide band multifrequency high-field EMR technique: A methodology for increasing spectroscopic information," *J. Magn. Reson.*, vol. 142, no. 2, pp. 300–312, Feb. 2000.

[73] G. Dodel, "On the history of far-infrared (FIR) gas lasers: Thirty-five years of research and application," *Infrared Phys. Technol.*, vol. 40, no. 3, pp. 127–139, Jun. 1999.

[74] *FIR THz Laser System*, Coherent, Inc., Santa Clara, CA, May 2010. [Online]. Available: http://www.coherent.com/downloads/SIFIR50_DSrevB.pdf

[75] B. S. Williams, "Terahertz quantum-cascade lasers," *Nature Photon.*, vol. 1, pp. 517–525, Sep. 2007.

[76] A. Wade, G. Fedorov, D. Smirnov, S. Kumar, B. S. Williams, Q. Hu, and J. L. Reno, "Magnetic-field-assisted terahertz quantum cascade laser operating up to 225 K," *Nature Photon.*, vol. 3, pp. 41–45, Jan. 2009.

[77] S. Takahashi, G. Ramian, M. S. Sherwin, L.-C. Brunel, and J. van Tol, "Sub-megahertz linewidth at 240 GHz from an injection-locked free-electron laser," *App. Phys. Lett.*, vol. 91, no. 17, p. 174102, Jun. 2007.

[78] K. Kreischer, C. Farrar, R. Griffin, R. Temkin, and J. Vieregg, "250 GHz gyrotron for NMR spectroscopy," in *Proc. IEEE 27th Int. Conf. Plasma Sci.*, New Orleans, LA, Jun. 2000, p. 198.

[79] C. D. Joye, R. G. Griffin, M. K. Hornstein, K.-N. Hu, K. E. Kreischer, M. Rosay, M. A. Shapiro, J. R. Sirigiri, R. J. Temkin, and P. P. Woskov, "Operational characteristics of a 14-W 140-GHz gyrotron for dynamic nuclear polarization," *IEEE Trans. Plasma Sci.*, vol. 34, no. 3, pp. 518–523, Jun. 2006.

[80] S.-T. Han, R. G. Griffin, K.-N. Hu, C.-G. Joo, C. D. Joye, J. R. Sirigiri, R. J. Temkin, A. C. Torrezan, and P. P. Woskov, "Spectral characteristics of a 140-GHz long-pulsed gyrotron," *IEEE Trans. Plasma Sci.*, vol. 35, no. 3, pp. 559–564, Jun. 2007.

[81] T. Idehara, I. Ogawa, L. Agusu, T. Kanemaki, S. Mitsudo, T. Saito, T. Fujiwara, and H. Takahashi, "Development of 394.6 GHz CW gyrotron (Gyrotron FU CW II) for DNP/proton-NMR at 600 MHz," *Int. J. Infrared and Millim. Waves*, vol. 28, no. 6, pp. 433–442, Jun. 2007.

[82] T. H. Chang, T. Idehara, I. Ogawa, L. Agusu, and S. Kobayashi, "Frequency tunable gyrotron using backward-wave components," *J. Appl. Phys.*, vol. 105, p. 063304, Mar. 2009.

[83] Y. Matsuki, H. Takahashi, K. Ueda, T. Idehara, I. Ogawa, M. Toda, H. Akutsua, and T. Fujiwara, "Dynamic nuclear polarization experiments at 14.1 T for solid-state NMR," *Phys. Chem. Chem. Phys.*, vol. 12, pp. 5799–5803, 2010.

[84] T. Idehara, K. Kosuga, L. Agusu, R. Ikeda, I. Ogawa, T. Saito, Y. Matsuki, K. Ueda, and T. Fujiwara, "Continuously frequency tunable high power sub-THz radiation source - Gyrotron FU CW VI for 600 MHz DNP-NMR spectroscopy," *J. Infrared Milli. Terahz Waves*, 2010, DOI: 10.1007/s10762-010-9643-y.

[85] T. Idehara, K. Kosuga, L. Agusu, I. Ogawa, H. Takahashi, M. E. Smith, and R. Dupree, "Gyrotron FU CW VII for 300 MHz and 600 MHz DNP-NMR spectroscopy," *J. Infrared Milli. Terahz Waves*, 2010, DOI: 10.1007/s10762-010-9637-9.

[86] S. Alberti, J.-P. Ansermet, K. Avramides, D. Fasel, J.-P. Hogge, S. Kern, C. Lievin, Y. Liu, A. Macor, I. Pagonakis, M. Silva, M. Tran, T. Tran, and D. Wagner, "Design of a frequency-tunable gyrotron for DNP-enhanced NMR spectroscopy," in *Proc. of 34th Int. Conf. on Infrared, Millimeter, and THz Waves*, Busan, Korea, Sep. 2009, pp. 1–2.

[87] M. Rosay, L. Tometich, S. Pawsey, R. Bader, R. Schauwecker, M. Blank, P. M. Borchard, S. R. Cauffman, K. L. Felch, R. T. Weber, R. J. Temkin, R. G. Griffin, and W. E. Maas, "Solid-state dynamic nuclear polarization at 263 GHz: Spectrometer design and experimental results," *Phys. Chem. Chem. Phys.*, vol. 12, pp. 5850–5860, 2010.

[88] V. E. Zapevalov, V. V. Dubrov, A. S. Fix, E. A. Kopelovich, A. N. Kuftin, O. V. Malygin, V. N. Manuilov, M. A. Moiseev, A. S. Sedov, N. P. Venediktov, and N. A. Zavolsky, "Development of 260 GHz second harmonic CW gyrotron with high stability of output parameters for DNP spectroscopy," in *Proc. of 34th Int. Conf. on Infrared, Millimeter, and THz Waves*, Busan, Korea, Sep. 2009, pp. 1–2.

[89] V. Denysenkov, M. J. Prandolini, M. Gafurov, D. Sezer, B. Endeward, and T. F. Prisner, "Liquid state DNP using a 260 GHz high power gyrotron," *Phys. Chem. Chem. Phys.*, vol. 12, pp. 5786–5790, 2010.

[90] M. K. Hornstein, V. S. Bajaj, R. G. Griffin, K. E. Kreischer, I. Mastovsky, M. A. Shapiro, J. R. Sirigiri, and R. J. Temkin, "Second harmonic operation at 460 GHz and broadband continuous frequency tuning of a gyrotron oscillator," *IEEE Trans. Electron Devices*, vol. 52, no. 5, pp. 798–807, May 2005.

[91] M. K. Hornstein, V. S. Bajaj, R. G. Griffin, and R. J. Temkin, "Continuous-wave operation of a 460-GHz second harmonic gyrotron oscillator," *IEEE Trans. Plasma Sci.*, vol. 34, no. 3, pp. 524–533, Jun. 2006.

[92] S. Alberti, M. Q. Tran, J. P. Hogge, T. M. Tran, A. Bondeson, P. Muggli, A. Perrenoud, B. Jödicke, and H. G. Mathews, "Experimental measurements on a 100 GHz frequency tunable quasioptical gyrotron," *Phys. Fluids B*, vol. 2, no. 7, pp. 1654–1661, Jul. 1990.

[93] I. I. Antakov, S. N. Vlasov, V. A. Ginzburg, L. I. Zagryadskaya, and L. V. Nikolaev, "MCR-generators with mechanical rearrangement of frequency," *Elektronnaia Tekhnika*, no. 8, pp. 20–25, 1975, (in Russian).

[94] G. F. Brand, Z. Chen, N. G. Douglas, M. Gross, J. Y. L. Ma, and L. C. Robinson, "A tunable millimetre-submillimetre gyrotron," *Int. J. Electron.*, vol. 57, no. 6, pp. 863–870, 1984.

[95] G. F. Brand and M. Gross, "Continuously tunable, split-cavity gyrotrons," *Int. J. Infrared and Millim. Waves*, vol. 6, no. 12, pp. 1237–1254, 1985.

[96] S. Alberti, M. Pedrozzi, M. Q. Tran, J. P. Hogge, T. M. Tran, P. Muggli, B. Jödicke, and H. G. Mathews, "Experimental measurements of competition between fundamental and second harmonic emission in a quasi-optical gyrotron," *Phys. Fluids B*, vol. 2, no. 11, pp. 2544–2546, Nov. 1990.

[97] Y. V. Zasypkin, "Electronic frequency tuning in gyrotrons," *Sov. J. Commun. Technol. Electron.*, vol. 33, no. 5, pp. 7–13, May 1988.

[98] A. C. Torrezan, S.-T. Han, M. A. Shapiro, J. R. Sirigiri, and R. J. Temkin, "CW operation of a tunable 330/460 GHz gyrotron for enhanced nuclear magnetic resonance," in *Proc. of 33rd Int. Conf. on Infrared, Millimeter, and THz Waves*, Pasadena, CA, Sep. 2008, pp. 1–2.

[99] A. C. Torrezan, M. A. Shapiro, J. R. Sirigiri, and R. J. Temkin, "A tunable continuous-wave 330 GHz gyrotron for enhanced nuclear magnetic resonance," in *Proc. IEEE 36th Int. Conf. Plasma Sci.*, San Diego, CA, Jun. 2009, p. 1.

[100] ——, "Operation of a tunable second-harmonic 330 GHz CW gyrotron," in *Proc. of IEEE Int. Vacuum Electronics Conference*, Monterey, CA, May 2010, pp. 199–200.

[101] A. C. Torrezan, S.-T. Han, I. Mastovsky, M. A. Shapiro, J. R. Sirigiri, R. J. Temkin, A. B. Barnes, and R. G. Griffin, "Continuous-wave operation of a frequency-tunable 460-GHz second-harmonic gyrotron for enhanced nuclear magnetic resonance," *IEEE Trans. Plasma Sci.*, vol. 38, no. 6, pp. 1150–1159, Jun. 2010.

[102] M. K. Hornstein, V. S. Bajaj, R. G. Griffin, and R. J. Temkin, "Efficient low-voltage operation of a CW gyrotron oscillator at 233 GHz," *IEEE Trans. Plasma Sci.*, vol. 35, no. 1, pp. 27–30, Feb. 2007.

[103] B. Piosczyk, "Electron guns for gyrotron applications," in *Gyrotron oscillators: their principles and practice*, C. J. Edgecombe, Ed. London, England: Taylor & Francis, 1993, pp. 123–146.

[104] G. S. Nusinovich, "Non-linear theory of a large-orbit gyrotron," *Int. J. Electron.*, vol. 72, no. 5 and 6, pp. 959–967, 1992.

[105] J. M. Baird, "Gyrotron theory," in *High-Power Microwave Sources*, V. L. Granatstein and I. Alexeff, Eds. Boston, MA: Artech House, 1987, pp. 103–184.

[106] B. G. Danly and R. J. Temkin, "Generalized nonlinear harmonic gyrotron theory," *Phys. Fluids*, vol. 29, no. 2, pp. 561–567, Feb. 1986.

[107] R. J. Temkin, "Analytic theory of a tapered gyrotron resonator," *Int. J. Infrared and Millim. Waves*, vol. 2, no. 4, pp. 629–650, 1981.

[108] M. A. Shapiro, Private communication, Jan. 2010.

[109] K. E. Kreischer, B. G. Danly, J. B. Schutkeker, and R. J. Temkin, "The design of megawatt gyrotrons," *IEEE Trans. Plasma Sci.*, vol. PS-13, no. 6, pp. 364–373, Dec. 1985.

[110] E. M. Choi, C. D. Marchewka, I. Mastovsky, J. R. Sirigiri, M. A. Shapiro, and R. J. Temkin, "Experimental results for a 1.5 MW, 110 GHz gyrotron oscillator with reduced mode competition," *Phys. Plasmas*, vol. 13, p. 023103, 2006.

[111] A. W. Fliflet and M. E. Read, "Use of weakly irregular waveguide theory to calculate eigenfrequencies, Q values, and RF field functions for gyrotron oscillators," *Int. J. Electron.*, vol. 51, no. 4, pp. 475–484, 1981.

[112] T. H. Chang, K. F. Pao, S. H. Chen, and K. R. Chu, "Self-consisten effects on the starting current of gyrotron oscillators," *Int. J. Infrared and Millim. Waves*, vol. 24, no. 9, pp. 1415–1420, Sep. 2003.

[113] G. N. Watson, *A treatise on the theory of Bessel functions*. Cambridge, United Kingdom: Cambridge University Press, 1966, ch. XI, pp. 359–361.

[114] M. Yedulla, G. S. Nusinovich, and T. M. Antonsen, Jr., "Start currents in an overmoded gyrotron," *Phys. Plasmas*, vol. 10, no. 11, pp. 4513–4520, 2003.

[115] M. Botton, T. M. Antonsen, Jr., B. Levush, K. T. Nguyen, and A. N. Vlasov, "MAGY: a time-dependent code for simulation of slow and fast microwave sources," *IEEE Trans. Plasma Sci.*, vol. 26, no. 3, pp. 882–892, Jun. 1998.

[116] *Cascade Engine v1.60*, Calabazas Creek Res., Inc., Saratoga, CA, 2001.

[117] O. Dumbrajs and A. Möbius, "Competition between co- and counter-rotating modes in gyrotrons," *Int. J. Electron.*, vol. 72, no. 5 and 6, pp. 683–686, 1992.

[118] M. Blank, B. G. Danly, B. Levush, P. E. Latham, and D. E. Pershing, "Experimental demonstration of a W-band gyroklystron amplifier," *Phys. Rev. Lett.*, vol. 79, no. 22, pp. 4485–4488, Dec. 1997.

[119] M. Blank, "High efficiency quasi-optical mode converters for overmoded gyrotrons," Ph.D. dissertation, Massachusetts Institute of Technology, Cambridge, MA, Sep. 1994.

[120] J. A. Kong, *Electromagnetic Wave Theory*. Cambridge, MA: EMW Publishing, 2000.

[121] E. M. Choi, M. A. Shapiro, J. R. Sirigiri, and R. J. Temkin, "Calculation of radiation from a helically cut waveguide for a gyrotron mode converter in the quasi-optical approximation," *J. Infrared Milli. Terahz Waves*, vol. 30, no. 1, pp. 8–25, Jan. 2009.

[122] J. M. Neilson and R. Bunger, "Surface integral equation analysis of quasi-optical launcher," *IEEE Trans. Plasma Sci.*, vol. 30, no. 3, pp. 794–799, Jun. 2002.

[123] *Surf3d v1.1*, Calabazas Creek Res., Inc., Saratoga, CA, 2004.

[124] M. A. Shapiro, Private communication, Apr. 2009.

[125] M. K. Hornstein, "A continuous-wave second harmonic gyrotron oscillator at 460 GHz," Ph.D. dissertation, Massachusetts Institute of Technology, Cambridge, MA, Jun. 2005.

[126] A. S. Gilmour, Jr., *Microwave Tubes*. Norwood, MA: Artech House, 1986.

[127] W. B. Hermannsfeldt, "EGUN - An electron optics and gun design program," SLAC, Stanford, CA, Tech. Rep. SLAC-331 UC-28, Oct. 1988.

[128] J. M. Baird and W. Lawson, "Magnetron injection gun (MIG) design for gyrotron applications," *Int. J. Electron.*, vol. 61, no. 6, pp. 953–967, 1986.

[129] *X-Ray Power Supply*, Spellman High Voltage Electronics Corp., Hauppauge, NY, Jul. 2010. [Online]. Available: http://www.spellmanhv.com/∼/media/Files/Products/DF_FF.ashx

[130] P. P. Woskov, M. K. Hornstein, R. J. Temkin, V. S. Bajaj, and R. G. Griffin, "Transmission lines for 250 and 460 GHz CW gyrotron DNP experiments," in *Proc. Joint 30th Int. Conf. Infrared Millim. Waves*, Williamsburg, VA, Sep. 2005, pp. 563–564.

[131] A. F. Mills, *Heat Transfer*. Upper Saddle River, NJ: Prentice Hall, 1999.

[132] *ePhysics, version 2.0*, Ansoft Corporation, Pittsburg, PA, 2006.

[133] P. P. Woskov, V. S. Bajaj, M. K. Hornstein, R. J. Temkin, and R. G. Griffin, "Corrugated waveguide and directional coupler for CW 250-GHz gyrotron DNP experiments," *IEEE Trans. Microw. Theory Tech.*, vol. 53, no. 6, pp. 1863–1869, Jun. 2005.